EUROPEAN ORGANIZATION FOR NUCLEAR RESEARCH

CERN/SPSLC 95–1
SPSLC/P 284
December 15, 1994

PROPOSAL TO THE SPSLC

LIFETIME MEASUREMENT OF $\pi^+\pi^-$ ATOMS TO TEST LOW ENERGY QCD PREDICTIONS

LAPP Annecy[1], Bern University[2], IAP Bucharest[3], CERN[4], JINR Dubna[5],
LNF-INFN Frascati[6], KEK Tsukuba-shi[7], Kyoto-Sangyo University[8],
Industrille-Kyushu University[9], NPI Moscow[10], Osaka City University[11], CdF Paris[12],
INP Orsay[13], LNS Saclay[14], University de Santiago de Campostela[15]

B.Adeva[15], L.Afanasyev[5], M.Angeles Lopez[15], M.Benayoun[12], A.Chvyrov[5], C.Ciortea[3], D.Dumitriu[3], P.Gianotti[6], F.Gomes[15], O.Gorchakov[5], L.Groza[3], C.Guaraldo[6], N.Kalinina[10], V.Karpukhin[5], M.Kobayashi[7], V.Komarov[5], V.Kruglov[5], L.Kruglova[5], A.Kulikov[5], A.Kuptsov[5], K.Kuroda[1], A.Lanaro[6], Y.Le Bornec[13], Ph.Leruste[12], V.Lucherini[6], T.Maki[9], L.Micu[3], L.Montanet[4], R.Mozzetti[6], J.Narjoux[12], L.Nemenov[5], F.Nichitiu[6*], M.Nikitin[5], M.Nupieri[6], K.Okada[8], T.Okusawa[11], V.Olshevsky[5], A.Pazos[15], M.Pentia[3], M.Petrascu[3], C.Petrascu[6*], I.Piticu[3], M.Plo[15], T.Ponta[3], Zh.Pustylnik[5], D.Rjabkov[5], A.Rosca[6*], J.Schacher[2], Yu.Scheglov[5], A.Selikov[10], Z.Szilagyi[3], F.Takeutchi[8], A.Tarasov[5], B.Tatischeff[13], S.Trusov[10], N.Willis[13], V.Yazkov[10], J.Yonnet[14], T.Yoshida[11], A.Zghiche[14†], V.Zoran[3] P.Zrelov[5]

GENEVA
1994

*on leave from IAP Bucharest
†CRN Strasbourg

Abstract

The proposed experiment aims to measure the lifetime of $\pi^+\pi^-$ atoms in the ground state with 10% precision, using the 24 GeV/c proton beam of the CERN Proton Synchrotron. As the value of the above lifetime of order 10^{-15}s is dictated by a strong interaction at low energy, the precise measurement of this quantity enables to determine a combination of S-wave pion scattering lengths to 5%. Pion scattering lengths have been calculated in the framework of chiral perturbation theory and values predicted at the same level of accuracy have, up to now, never been confronted with accurate experimental data. Such a measurement would submit the understanding of chiral symmetry breaking of QCD to a crucial test.

Contents

Chapter 1

Introduction

Pion-pion scattering at low energies is analysed in terms of scattering lengths. At present pion-pion scattering is still an unresolved problem in the framework of QCD. However the approach based on an effective lagrangian and Chiral Perturbation Theory (CHPT) allows to predict S-wave $\pi\pi$ scattering lengths within 5%. These predictions have not yet been tested at such a level of accuracy (the best precision is 20%).

To obtain the pion scattering lengths in a model-independent way, a measurement of the lifetime of exotic atoms formed by π^+ and π^- mesons ($A_{2\pi}$ or dimesoatom) in their ground state is suggested. There exists a precise relationship between this lifetime τ and the difference of the isoscalar a_0 and isotensor a_2 S-wave scattering lengths: $1/\tau = C|a_0 - a_2|^2$. To determine $|a_0 - a_2|$ down to 5%, corresponding to the theoretical uncertainty, the lifetime has to be measured with 10% accuracy. This is the goal of the proposed experiment. The value of τ predicted by CHPT is $3.7 \cdot 10^{-15}$ s.

This measurement will submit the modern concept of chiral symmetry breaking to a crucial test. Any significant discrepancy between the theory and the experiment would demonstrate a basic problem in our understanding of the QCD vacuum structure.

Atoms $A_{2\pi}$ will be produced in proton-nucleus (e.g. Ti) interactions at 24 GeV/c (CERN Proton Synchrotron). After production in the target, these relativistic atoms ($\gamma \simeq 10$) may either decay into $\pi^0\pi^0$ or get excited or break up (be ionized) in the target material. In the case of breakup, characteristic charged pion pairs, called "atomic pairs", will emerge. These pairs have a low relative momentum q in their centre of mass system ($q < 3$ MeV/c) and so a small opening angle ($\theta_{+-} < 3$ mrad) and nearly identical energies ($E_+ \simeq E_-$ at the 0.3% level) in the lab system. The proposed experimental setup consists of a magnetic double arm spectrometer with a resolution on relative pair momenta of $\sigma_q \simeq 1$ MeV/c. By these means, it is possible to determine the number of "atomic pairs" above the background of pion pairs produced in a free state. The total number of produced $A_{2\pi}$ is related by an exact expression to the number of "free" pion pairs with a low relative momentum. For a given target material and thickness, the ratio of the number of observed "atomic pairs" to the total number of produced $A_{2\pi}$ depends on the lifetime τ in a unique way. For the optimum target the observation of $\sim 2 \cdot 10^4$ "atomic pairs" allows to measure τ with the desired accuracy of 10%. Considering the experiment at CERN PS, the necessary amount of data should be collected in a running time of about 7 weeks, including a reasonable safety factor.

The experimental setup consists of a scintillating fibre detector and a scintillation hodoscope near the target, a spectrometer magnet (bending power of 2 Tm) and two tele-

scope arms, each equipped with drift chambers, scintillation hodoscopes, gas Cherenkov counters and muon identifiers. The relative momentum resolution required for identification of "atomic pairs" is provided by the high coordinate resolution of the fibre detector and of the drift chambers. In addition, thin targets and thin windows in the vacuum system must keep the effect of multiple scattering small. With a primary intensity of 10^{11} protons per spill, a first level trigger rate of $3 \cdot 10^4$ events per spill, due to free and accidental pairs, is expected. This high LHC-like trigger rate will be reduced by a factor $\sim$30 with the trigger system. Special purpose processors will reject events with an opening angle of more than 3 mrad as well as events with a relative momentum larger than 30 MeV/c.

Among other physics subjects accessible to the proposed setup, only three topics are mentioned here:

1. The observation of long-lived $A_{2\pi}$ states helps to study the feasibility of a Lamb shift measurement in $A_{2\pi}$. This energy shift is related to the pion scattering length combination $(2a_0 + a_2)$ and hence its measurement, coupled with the lifetime measurement, would provide a determination of a_0 and a_2, separately.

2. The observation of π^+K^- atoms and measurement of their lifetime would allow to extract model-independent values for πK scattering lengths. A comparison of these lengths with CHPT predictions would give the possibility to test the chiral symmetry breaking in processes with strange quarks.

3. The analysis of pion pairs enables to investigate strong and Coulomb $\pi\pi$ correlations in the range of very small relative momenta with high momentum resolution using high statistics $\sim 10^7$.

Chapter 2

Theoretical motivation

The standard model (SM) of elementary particles comprises our understanding of the strong and electroweak interactions. Symmetries play the central role in determining the dynamical structure of the model. Although many input parameters are needed, the SM is a mathematical construction of considerable predictive power.

The strong part of the SM, quantum chromodynamics (QCD), is a gauge theory of coloured quarks and gluons. QCD as a nonabelian gauge theory exhibits two distinct features, asymptotic freedom and colour confinement. At large momentum transfer, QCD predictions have successfully been tested in many reactions, but clearly these results cover only one aspect of the theory, namely asymptotic freedom. It is of great importance to also study the nonperturbative region of QCD in order to fully understand the dynamics of strongly interacting hadrons. Up to now, mainly two accepted methods to handle nonperturbative QCD have been developed: lattice calculations [LATT93] and chiral perturbation theory [LEUT93]. In the following we concentrate on the latter.

2.1 Chiral symmetry and chiral perturbation theory

Consider QCD with two flavours u and d. In the case of massless quarks, $\mathcal{L}_{\rm QCD}$ is invariant under chiral $\mathrm{SU}(2)_L \times \mathrm{SU}(2)_R$ transformations. On the other hand, the observed hadron spectrum suggests that the ground state of the theory is asymmetric under the action of this group (spontaneous breakdown of chiral symmetry). As a consequence, there exist three massless pseudoscalar particles in the spectrum (Goldstone bosons). The three lightest hadrons $\pi^{\pm}$, π^0 indeed are pseudoscalars, but these particles are not exactly massless as it would be appropriate for Goldstone bosons. This is attributed to the fact that the full lagrangian of QCD is not chiral invariant—the masses m_u, m_d break the symmetry $\mathrm{SU}(2)_L \times \mathrm{SU}(2)_R$ and provide the pions with a mass, $m_\pi \simeq 135$ MeV.

The Goldstone nature of the pseudoscalar mesons implies strong constraints on their mutual interactions. These are studied most efficiently in the framework of an effective theory, which is formulated in terms of the physical pion fields [WEIN68] instead of quark and gluon degrees of freedom. This framework, called chiral perturbation theory is mathematically equivalent to QCD [WEIN79, LEUT93] and provides a systematic way to evaluate S-matrix elements at low energies [WEIN79, GASS83, LEUT93, LEUT93A, CHPT]. It consists in an expansion of the Green functions in powers of the external momenta and of the quark masses. Lorentz invariance, P, C and chiral symmetry determine the

structure of the effective lagrangian which allows one to work out that expansion,

$$\mathcal{L}_{\rm eff} = \mathcal{L}^{(2)} + \mathcal{L}^{(4)} + \cdots \,, \tag{2.1}$$

where the indices denote the number of derivatives and quark mass insertions. At low energies, the term with the smallest number of derivatives will dominate, because the higher order contributions are small in this energy range. The leading order lagrangian is

$$\mathcal{L}^{(2)} = \frac{F_\pi^2}{4} {\rm tr}\langle \partial_\mu U \partial^\mu U^\dagger + m_\pi^2 (U + U^\dagger) \rangle \,, \tag{2.2}$$

where the unitary matrix

$$U = \exp \frac{i\pi}{F_\pi} \,; \qquad \pi = \begin{pmatrix} \pi^0 & \sqrt{2}\pi^+ \\ \sqrt{2}\pi^- & -\pi^0 \end{pmatrix} \tag{2.3}$$

collects the pion fields. According to the rules of CHPT, the leading order term in the low-energy expansion is obtained by evaluating tree diagrams with $\mathcal{L}^{(2)}$. These contributions thus contain just two parameters—the pion decay constant F_π and the pion mass m_π. These are not determined by chiral symmetry alone and are taken instead from experiments. The next-to-leading order terms are obtained by evaluating one-loop diagrams with $\mathcal{L}^{(2)}$ and adding tree diagrams from $\mathcal{L}^{(4)}$. The latter lagrangian contains seven further low-energy constants $l_1, \ldots, l_7$ which absorb the infinities generated by the loop contributions. Their renormalized values $\bar{l}_i$ have been extracted from low-energy data some time ago [GASS84]. Continuing in this way, a systematic expansion is obtained, and a large body of processes has been calculated with controlled precision [WEIN79, GASS84, GASS85, LEUT93A, CHPT].

CHPT exploits only one part of the information contained in the lagrangian of QCD, its symmetry properties. Lattice calculations are of a wider scope: they allow one to calculate the full set of Green functions at any value of the momenta in terms of the scale of the theory and of the quark masses. In particular, it is in principle possible to evaluate in this manner the unknown low-energy constants which occur in the effective lagrangian. Once this can be achieved, it is, of course, not necessary anymore to make use of CHPT, because the relevant information may then be obtained directly from a lattice calculation. Unfortunately, one has presumably still to wait a long time before this program reaches the accuracy aimed in CHPT. The reason for this is the smallness of the pion mass: to make sure that the lattice calculation reproduces correctly the infrared singularities encountered in the low-energy expansion, the lattice must extend to distances large in comparison to m_π^{-1}. Note that one cannot see all of these singularities in the quenched approximation—the calculation has to include the fermion determinant to correctly reproduce the chiral logarithms. It seems fair to say that a lattice calculation that accurately accounts for these long range effects is not in sight.

Pion-pion scattering was also studied in quark models [VOLK87, EFIM86].

2.2 $\pi\pi$ scattering: theory

Pion scattering is one of the rare examples in strong interaction where the theoretical predictions are more accurate than the available experimental results. In the following we consider in particular the difference

$$\Delta = a_0 - a_2 \tag{2.4}$$

of S-wave scattering lengths $a_{0,2}$ with isospin $I = 0,\ 2$. (Here we neglect isospin breaking effects which are considered shortly below.) In the framework of QCD, the scattering lengths are functions of the renormalization group invariant quark mass and of the scale of QCD. They are represented in CHPT by an expansion in powers (and logarithms) of the pion mass,

$$\Delta = \Delta_0 \left\{ 1 + \Delta_2 m_\pi^2 + \Delta_4 m_\pi^4 + \ldots \right\} . \tag{2.5}$$

The scale in this expansion is $4\pi F_\pi \simeq 1.2$ GeV. The leading term Δ_0 may be obtained by evaluating the contribution from the tree graph in Figure 2.1a. This diagram corresponds to the first term, $O(p^2)$, of the momentum expansion for the pion scattering amplitude and generates the current-algebra expression for the $\pi\pi$ scattering lengths, derived by Weinberg a long time ago [WEIN66]. The result for the leading term Δ_0 becomes

$$\Delta_0 = \frac{9 m_\pi^2}{32\pi F_\pi^2} = 0.20 . \tag{2.6}$$

Here and further on the units $\hbar = c = m_\pi = 1$ are used.

The next-to-leading order contribution Δ_2 is due to one-loop diagrams generated by $\mathcal{L}^{(2)}$ and to tree graphs from $\mathcal{L}^{(4)}$—we display in figure (2.1b-2.1e) some of the relevant diagrams of $O(p^4)$.

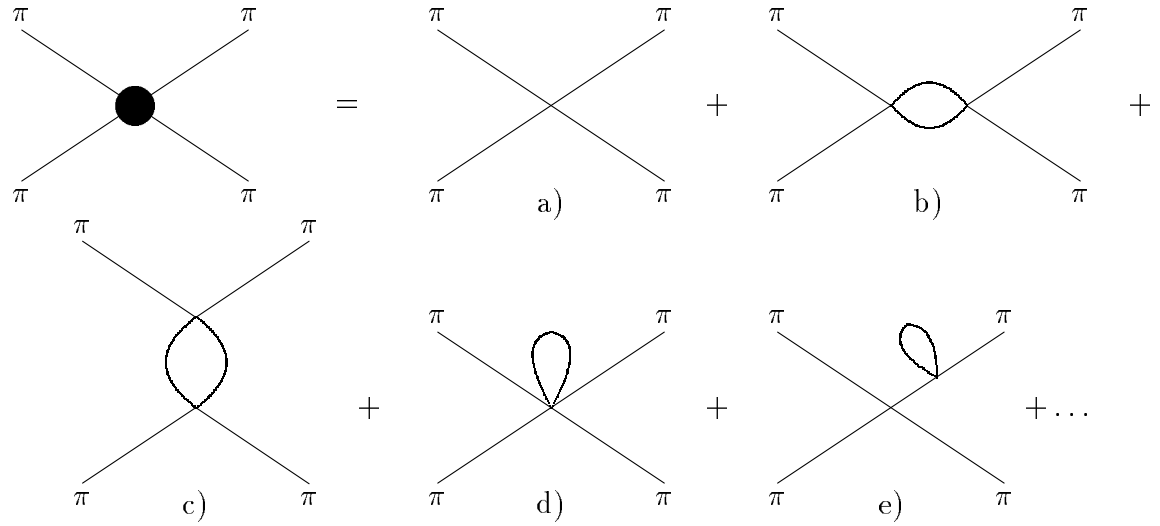

Figure 2.1: The $\pi\pi$ scattering amplitude in the loop expansion. The diagram a) displays the tree graph which generates the leading order term (2.6). The graphs b)–e) stand for one-loop corrections which contribute to Δ_2, see equation (2.7).

The quantity Δ_2 contains four of the seven low-energy constants mentioned above and depends logarithmically on the pion mass [GASS84]. To calculate numerically this correction, one may replace two of the four low-energy constants by the D-wave scattering lengths a_0^2, a_2^2 (notation a_I^l) and a third one by $\langle r^2 \rangle_S^\pi$, the scalar charge radius of the pion [GASS84]

$$\Delta_2 = \frac{1}{3} \left\{ \langle r^2 \rangle_S^\pi + 40\pi F_\pi^2 (a_0^2 + 2a_2^2) + \frac{1}{480\pi^2 F_\pi^2} (517 - 15\bar{l}_3) \right\} . \tag{2.7}$$

Inserting the numerical values[1] gives

$$\Delta = 0.25 \pm 0.01\,. \tag{2.8}$$

The values of the usually used scattering lengths are [GASS84]

$$a_0 = (0.20 \pm 0.01) \qquad \text{and} \qquad \mathrm{a}_2 = (-0.042 \pm 0.002)\,. \tag{2.9}$$

The error in (2.8) includes an estimate of higher order corrections in the quark mass expansion.

It should be noted:

1. The contribution from the scalar radius $\langle r^2\rangle_S^\pi$ amounts to a 10% correction. The numerical value quoted is the result of a dispersive calculation [DONO90]. CHPT yields an independent determination [GASS84], based on the ratio F_K/F_π, which is in good agreement with the dispersive result. Since the uncertainty in the value of $\langle r^2\rangle_S^\pi$ is of order 10%, it affects the error bar of the prediction at the 1% level.

2. According to the $\pi\pi$ phase shift analysis of Froggatt and Petersen [FROG77], the contribution of the D-waves amounts to $\Delta_{\mathrm{D-waves}} = \frac{15}{4} m_\pi^4 (a_0^2 + 2a_2^2) = 0.0074$, so that this term represents a correction of about 4%. A recent calculation [BIJN94A] of K_{e4} decay matrix element in the framework of $\mathrm{SU}(3)_L \times \mathrm{SU}(3)_R$ allows an independent determination of the D-wave scattering lengths, based on the threshold value [ROSS77] of two K_{e4} form factors. The value obtained, $\Delta_{\mathrm{D-waves}} = 0.0083$, neatly confirms the above result.

3. The constant $\bar{l}_3$ determines the magnitude of the corrections, which occur, when m_π^2 is expanded in powers of the quark masses. The leading term of this expansion is proportional to $m_u + m_d$,

$$m_\pi^2 = m^2 \left\{ 1 - \frac{m^2}{32\pi^2 F_\pi^2}\, \bar{l}_3 + O(m^4) \right\}, \quad m^2 \equiv B(m_u + m_d)\,.$$

   According to Gell-Mann, Oakes and Renner, the constant B is related to the value of the quark condensate in the chiral limit. In the standard CHPT framework, $\bar{l}_3$ is a quantity of order one and therefore generates a very small contribution, such that the expansion is dominated by the leading term. In the case of Δ, the correction from $\bar{l}_3$ amounts to less than 1%.

4. The further contributions, arising from higher order effects, are expected to be small. The full two-loop calculation, which will allow one to estimate these corrections more reliably, is in progress [COLA94, BIJN94B].

5. The origin of isospin breaking effects is due to the quark mass difference $m_u - m_d \neq 0$ and to electromagnetic interactions. The quark mass difference generates a tiny shift of 0.2 MeV to $m_{\pi^+} - m_{\pi^0}$ [GASS84], whereas the $\pi\pi$ scattering amplitude remains isospin symmetric up to and including the first non-leading order in the low-energy

[1] $\langle r^2\rangle_S^\pi = 0.60 \pm 0.05\mathrm{fm}^2$ [DONO90]; $\bar{l}_3 = 2.9 \pm 2.4$ [GASS84]; $a_0^2 = (17 \pm 3) \cdot 10^{-4} m_\pi^{-4}$ and $a_2^2 = (1.3 \pm 3) \cdot 10^{-4} m_\pi^{-4}$ [NAGE79]; $F_\pi = 92.4$ MeV [REVI94].

expansion [GASS84]. Therefore we do not consider these effects any longer here. The effects generated by the electromagnetic interactions are also very small. They modify the $\pi^+\pi^- \to \pi^0\pi^0$ scattering amplitude at threshold, $(p_{\pi^+} + p_{\pi^-})^2 = 4m_{\pi^+}{}^2$, by a contribution proportional to the fine structure constant, $\Delta \to \Delta + \alpha C$. Using the lowest order effective lagrangian for electromagnetic interactions gives $C \simeq 0.6$ [GASS94], which amounts to a correction in the theoretical prediction for Δ of less than 2%. In [MOOR94], the quantity C has been estimated using a potential model. For reasonable values of the range of the potential used, the effect is of similar size as the one obtained with the effective lagrangian approach. Work to refine these estimates is in progress [GASS94, RASC94].

Although standard CHPT is widely used, it may be questioned. The standard theory assumes that the light quark masses are small enough for the expansion of the meson masses in powers of the quark masses to be dominated by the leading term, given by the Gell-Mann-Oakes-Renner relation. A direct experimental proof of this assumption is not available. Stern and collaborators [STER93] have investigated the possibility that, for one reason or another, the quark condensate happens to be small, such that the leading term fails to dominate the expansion. They have shown that many of the predictions of standard CHPT do not hold then. A particular example is the Gell-Mann-Okubo formula for the masses of the pseudoscalars, the success of which would then have to be taken as accidental. The prediction for the quantity Δ is also lost, because the framework of Ref. [STER93] leaves the constant $\bar{l}_3$ unspecified. A value like $\bar{l}_3 = -100$, e.g., increases the result for Δ by about 25% and brings it into agreement with the central value of the currently available data (see below). If confirmed, the corresponding term in the expansion of m_π^2, which in the standard theory represents a correction of order 2%, would instead be of the same order of magnitude as the leading term.

The implications for the current understanding of QCD would be drastic. In particular, the values of the quark mass ratios $m_u : m_d : m_s$, which follow from Weinberg's formulae [WEIN77], would then be ruled out. The fact that the ratios obtained with QCD sum rules and lattice methods are in good agreement with the predictions of standard CHPT, would then be accidental — worse, each of these methods would be incorrect.

One of the objectives of the proposed experiment is to decide the issue, be it by confirming the standard theory, or by invalidating it.

2.3 $\pi\pi$ scattering: experiment

The measurements of $\pi\pi$ scattering can be divided into two groups. The first one includes experiments that can be interpreted in a model-independent way and so the precision of the obtained results is determined by experimental errors only. The second group of experiments is analyzed in the framework of models and the results contain, in addition to experimental errors, model uncertainties whose size can only be estimated.

Most precisely the S-wave scattering length a_0 was determined in a model-independent way from K_{e4} decay [ROSS77]. The difference of the $\pi\pi$ scattering phases was obtained for effective $\pi\pi$ masses in the range 280 MeV $\leq M_{\pi\pi} \leq$ 380 MeV. Then using Roy-equation fits, a_0 was found [FROG77]:

$$a_0 = 0.26 \pm 0.05\,. \tag{2.10}$$

As can be seen from (2.10) the experimental a_0 value is still five times more uncertain than the theoretical value (2.9).

An estimation of Δ can be obtained using the universal curve [MORG68, NAGE79] that allows to express a_2 through a_0:

$$\Delta = 0.29 \pm 0.04\,. \tag{2.11}$$

Additional data on $\pi\pi$ scattering lengths were obtained considering different models. In the interval 500 MeV $\leq M_{\pi\pi} \leq$ 1000 MeV values for the $\pi\pi$ scattering phase were extracted from an analysis of the reaction $\pi\, N \to \pi\, \pi\, N$ in the initial pion momentum range 4.5 GeV/c $\leq p_\pi \leq$ 17 GeV/c. Information on $\pi\pi$ scattering phases was obtained after extracting the contribution of the one pion exchange to the differential cross section for the reaction. Note that estimation of the role of the one pion exchange term and the analysis of the one pion diagram involve model uncertainties. The extrapolation of $\pi\pi$ scattering phase to $M_{\pi\pi} = 2m_\pi$ leads to [OCHS91]:

$$a_0 = 0.23 \pm 0.08\,. \tag{2.12}$$

For interpretation of experiments on the reaction $\pi\, N \to \pi\, \pi\, N$ near threshold it is possible to use a semi-phenomenological theory [ANIS65] based on relative momentum expansion of the amplitude for the process. As effects caused by $\pi\pi$ interaction in the final state are proportional to relative momentum, this contribution will be small just in the region where the model describes experimental data well. The values of Δ in this approach are

$$\Delta = \begin{array}{ll} 0.25 \pm 0.05 & \text{[BATU65]} \\ 0.42 \pm 0.10 & \text{[BLAI70]} \end{array}\,. \tag{2.13}$$

A value of the $\pi\pi$ scattering length a_2 may be found [OLLS67] in a model-dependent way from an analysis of the process $\pi^+ p \to \pi^+ \pi^+ n$ near threshold. A measurement of the cross section of this reaction at pion kinetic energies 180 MeV $\leq E_\pi \leq$ 200 MeV gives for a_2 the value [SEVI90]:

$$a_2 = -0.040 \pm 0.003\,. \tag{2.14}$$

Here the error is purely experimental and does not include model-uncertainties. The model used in the analysis of the experimental data took into account only two main graphs, but not rescattering effects in the final state, loops and lagrangian $\mathcal{L}^{(4)}$. Besides, many other graphs contribute to this reaction and to evaluate their role at the percentage level is practically impossible.

The determination of $\pi\pi$ scattering phases from an analysis of decays $K \to \pi\, \pi\, \pi$ is also model-dependent.

The scattering lengths and Δ are proportional to the quark mass and hence to the explicit symmetry breaking part in $\mathcal{L}_{\rm QCD}$. Should it turn out that a direct and more precise measurement leads to an apparent discrepancy between theory and experiment, the standard picture of the vacuum structure of QCD would have to be revised [STER93].

2.4 Atoms consisting of π^+ and π^- mesons as a source of model-independent data on $\pi\pi$ scattering in the S-state

After the clear evidence [AFAN93A] for the production of bound state of $\pi^+\pi^-$ (atom $A_{2\pi}$) a study of the $A_{2\pi}$ properties should allow to measure at first the difference $|a_0 - a_2|$ with the required precision and then a_0 and a_2 separately. In the following these properties and their connection to a_0 and a_2 will be discussed.

2.4.1 Lifetime of $A_{2\pi}$

The decay probability of $A_{2\pi}$ is mainly determined by the charge exchange process

$$\pi^+ + \pi^- \to \pi^0 + \pi^0 \tag{2.15}$$

(branching $\sim 99.6\%$) and is equal to [URET61]

$$W_{n,0}(\pi^0\pi^0) = \frac{1}{\tau_{n,0}} = \frac{8\pi}{9}\left[\frac{2\Delta m}{\mu}\right]^{1/2}(a_0 - a_2)^2|\psi_{n,0}(0)|^2\,. \tag{2.16}$$

Here, $\tau_{n,0}$ is the lifetime of the atom with the principal quantum number n and the orbital angular momentum $l = 0$, $\psi_{n,0}(0)$ is the atom wave function in coordinate representation at zero distance between π^+ and π^-, $\Delta m = M_A - 2m_{\pi^0}$, M_A is the atom mass, and μ is the reduced atom mass. The relation (2.16) is model-independent and its uncertainty does not exceed a few percent. The calculation of corrections reduce the uncertainty down to the percent level [MOOR94].

Strong interaction and vacuum polarization lead only to small corrections to the Coulomb wave function $\psi_{1,0}(0)$ [EFIM86, BELK86]:

$$\psi_{1,0}(0) = \psi^c_{1,0}(0)(1 + 3.3 \cdot 10^{-4})\,. \tag{2.17}$$

For the Coulomb wave function one has

$$|\psi^c_{n,0}(0)|^2 = \frac{p_B^3}{\pi n^3}\,, \tag{2.18}$$

where p_B is the Bohr momentum of the $\pi^+\pi^-$ atom: $p_B = \alpha\mu$, α is the fine structure constant. Using (2.16) and (2.18) one receives,

$$\tau_{n,0} = \tau \cdot n^3 \tag{2.19}$$

where τ is the $A_{2\pi}$ lifetime in the ground state. If the atom orbital momentum is odd then the decay into two π^0 mesons is forbidden by angular momentum conservation and Bose symmetry. If the orbital momentum l is even and $l > 0$, then annihilation is suppressed by α^2. Consequently the $A_{2\pi}$ lifetimes for $l > 0$ are by a factor of 10^4 larger than τ. Hence, $A_{2\pi}$ annihilation takes place mainly from $l = 0$ states with lifetimes given by (2.19). By measuring the atom annihilation probability and knowing the distribution of $A_{2\pi}$ over n, one is able to obtain the lifetime τ and, finally, to extract a value for $|a_0 - a_2|$.

Using the chiral theory prediction (2.8) one can estimate

$$\tau = (3.7 \pm 0.3) \cdot 10^{-15}\,\mathrm{s}\,. \tag{2.20}$$

2.4.2 Relation between probabilities for $A_{2\pi} \to \gamma + \gamma$ and $A_{2\pi} \to \pi^0 + \pi^0$ decays

The probability for the decay of $A_{2\pi}$ into two photons [URET61] is given by

$$W_{n,0}(\gamma\gamma) = \frac{2\pi\alpha^2}{m_\pi^2}|\psi_{n,0}|^2 \tag{2.21}$$

and is about 250 times less than the probability of decay into two π^0 (2.19). By measuring $W_{\gamma\gamma}/W_{\pi^0\pi^0}$ with 10% accuracy one can obtain $|a_0 - a_2|$ with 5% precision.

In the Letter of Intent [VIGD92] an experiment is proposed to observe $A_{2\pi}$ at the Indiana University accelerator (IUCF Cooler). Dimesoatoms will be generated in the reaction

$$p + d \to {}^3He + A_{2\pi} \tag{2.22}$$

at the proton energy exceeding the threshold of $\pi^+\pi^-$ pair production by 1 MeV. If the yield of $A_{2\pi}$ is sufficiently high, then the authors will plan an experiment to measure $W_{(\gamma\gamma)}/W_{(\pi^0\pi^0)}$ with a precision of 10%.

2.4.3 Energy difference between np and ns levels

Strong interaction and vacuum polarization lead to a splitting of energy levels and so to a difference ΔE_{ns-np} between ns and np energy levels. For $n = 2$ the value $\Delta E^{(s)}_{2\mathrm{s}-2\mathrm{p}}$ resulting from strong interaction [EFIM86] amounts to

$$\Delta E^{(s)}_{2\mathrm{s}-2\mathrm{p}} = -\frac{2\pi}{3m_\pi}|\psi_{1,0}(0)|^2(2a_0 + a_2) \approx -0.3 \text{ eV}\,. \tag{2.23}$$

This "strong" contribution constitutes the main part of the splitting, as the vacuum polarization adds to $\Delta E_{2\mathrm{s}-2\mathrm{p}}$ only $\Delta E^{(pol)}_{2\mathrm{s}-2\mathrm{p}} = -0.06$ eV.

Simultaneous measurement of lifetime and Lamb shift allows to obtain a_0 and a_2 separately in model-independent way and to test further predictions of CHPT.

2.5 CP violation and $\pi\pi$ scattering lengths

One of the parameters connected with direct CP violation is ϵ'. The phase of ϵ' is given [REVI94]:

$$\phi(\epsilon') = \frac{1}{2}\pi - \delta\,, \quad \delta = \delta_0 - \delta_2\,, \tag{2.24}$$

where $\delta_0(\delta_2)$ is the S-wave phase of $\pi\pi$-scattering with isospin 0(2) at a c.m.s. energy of $\pi\pi$ ($M_{\pi\pi}$) equal to the K meson mass. Up to now the value of δ was found [OCHS91] using the phases δ_0 and δ_2 in the interval $0.6 \le M_{\pi\pi} \le 1$ GeV [GRAY74]. The values δ_0 and δ_2 were described using dispersion relations. The $\pi\pi$ scattering length a_0 was considered as a free parameter. Its value was found to be

$$a_0 = 0.30 \pm 0.13 \quad \text{(from } \delta_0 \text{ approximation)} \tag{2.25}$$

$$a_0 = 0.17 \pm 0.13 \quad \text{(from } \delta_2 \text{ approximation).} \tag{2.26}$$

The corresponding value of δ is:

$$\delta = (47 \pm 6)^\circ . \tag{2.27}$$

The analysis made in other experiments does not contradict (2.27) if the systematical errors of the experimental data are taken into account [OCHS91].

A model-independent measurement of $a_0 - a_2$, that defines the behaviour of δ at low energy, would allow to reach substantially better reliability in the determination of δ.

In this proposal it is planned to determine $|a_0 - a_2|$ with 5% precision by measuring the lifetime $\tau_{1,0}$. The way to measure scattering lengths is based on the fact that the proposed method of $A_{2\pi}$ observation and the lifetime measurement [NEME85] was experimentally demonstrated [AFAN93A, AFAN94].

Chapter 3

Production of $A_{2\pi}$ and pionic pairs in high energy collisions

We intend to measure the lifetime of $A_{2\pi}$ produced in interactions of 24 GeV protons with target nuclei. The atoms will be observed by detecting $\pi^+\pi^-$ pairs from the atom breakups which occur in the target where they are produced. The pions from $A_{2\pi}$ breakup have a low relative momentum (< 3 MeV/c) and are to be observed as an excess above a large background of $\pi^+\pi^-$ free pairs.

In this Chapter we give the equation which relates the $A_{2\pi}$ production cross section with the doubly inclusive cross section of $\pi^+\pi^-$ pair production. The effects of Coulomb and strong correlations for free $\pi^+\pi^-$ pair production cross section are also considered. The measurement methods of $A_{2\pi}$ lifetime are described in Chapter 4.

3.1 Cross section of $A_{2\pi}$ production and $A_{2\pi}$ quantum numbers

In ref. [NEME85] the production of $\pi^+\pi^-$ atoms (and of other hadronic atoms) in inclusive processes was discussed, and a method for the observation of these atoms and their lifetime measurement was proposed. Based on quantum mechanics only, there was given an exact formula (3.1) relating the atom production cross section to the double inclusive production cross section for the particles forming the atom.

Thus the probability of $A_{2\pi}$ production is proportional to the double inclusive cross section for the production of π^+ and π^- with a small relative momentum and to the atom wave function squared at zero particle distance. The atoms are generated in S-states with the cross section:

$$\frac{d\sigma_n^A}{d\vec{p}_A} = (2\pi)^3 \frac{E_A}{M_A} |\Psi_n(0)|^2 \left. \frac{d\sigma_s^0}{d\vec{p}_1\, d\vec{p}_2} \right|_{\vec{p}_1=\vec{p}_2=\vec{p}_A/2}, \qquad (3.1)$$

where $\vec{p}_A$, E_A and M_A are momentum, energy and mass of the $\pi^+\pi^-$ atom in the laboratory system, respectively; $|\Psi_n(0)|^2$ is the atomic wave function squared at the origin (see (2.17), (2.18)); $d\sigma_s^0/d\vec{p}_1\, d\vec{p}_2$ is the double inclusive production cross section for $\pi^+\pi^-$ pairs from short-lived sources without taking into account $\pi^+\pi^-$ Coulomb interaction in the final

state (see Section 3.2); $\vec{p}_1$ and $\vec{p}_2$ are the π^+ and π^- momenta in the laboratory system. The π^+ and π^- momenta obey the relation $\vec{p}_1 = \vec{p}_2 = \vec{p}_A/2$.

The $A_{2\pi}$ are produced with orbital momentum $l = 0$, as $|\Psi_n(0)|^2 = 0$ for $l \neq 0$, and in atomic states with principal quantum numbers n, distributed according to $|\Psi_n(0)|^2 \sim n^{-3}$: $W_1 = 83\%$, $W_2 = 10.4\%$, $W_3 = 3.1\%$, $W_{n\geq 4} = 3.5\%$. Note that $\Sigma_{n=1}^{\infty}|\Psi_n(0)|^2 = 1.202|\Psi_1(0)|^2$.

The double inclusive cross section may be written in the form [GRIS82]

$$\frac{d\sigma^0}{d\vec{p}_1\, d\vec{p}_2} = \frac{1}{\sigma_{in}} \frac{d\,\sigma}{d\,\vec{p}_1} \frac{d\,\sigma}{d\,\vec{p}_2}\, R(\vec{p}_1, \vec{p}_2)\,, \tag{3.2}$$

where $d\sigma/d\vec{p}_1$ and $d\sigma/d\vec{p}_2$ are single particle inclusive cross sections, σ_{in} is the inelastic inclusive cross section of hadron production, R is a correlation function due to the strong interactions only. In the case of π^+ and π^- mesons, satisfying the requirement $\vec{p}_1 = \vec{p}_2$ $R = 1.65 \pm 0.05$ [GRIS82, URIB94]. Note that the absolute values of R and cross sections have not to be known exactly for the atom lifetime measurement.

3.2 Free pairs. Coulomb and hadron correlations.

The inclusive spectrum of free $\pi^+\pi^-$ pairs consists of a sum of two kinds of events which are different with respect to the size of the π^+ and π^- meson formation region.

Events of the first kind contain particles arising from short-lived sources and broad resonance decays (ρ, ω, Δ, ...). In this case the typical range of pion formation is $r_{\rm form} \sim 1/m_\pi \sim 1 \div 3$ fm, much less than the Bohr radius of the $\pi^+\pi^-$ atom: $r_B = 387$ fm. The differential production cross section of these pairs at small relative momenta (in pair c.m.s. $q < 10$ MeV/c) is enhanced by the Coulomb interaction between the pions in the final state [AFAN91A]. The pion pairs, produced by short-lived sources, will therefore be named "Coulomb" pairs.

The second kind of pion pairs are events in which one or both particles are coming from long-lived sources (η, K^0_S, Λ, ...). In this case the typical range between pions is > 1000 fm and hence Coulomb and strong interaction effects in the final state are negligible. These pairs will be called "non-Coulomb" pairs.

At $r_{\rm form} \ll r_B$ the production cross section of "Coulomb" pairs with pion momenta $\vec{p}_1$ and $\vec{p}_2$ can be written:

$$\frac{d\sigma_s}{d\vec{p}_1\, d\vec{p}_2} = A_c(\beta)\frac{d\sigma^0_s}{d\vec{p}_1\, d\vec{p}_2} = A_c(\beta)\frac{1}{\sigma_{in}} \frac{d\sigma_s}{d\vec{p}_1} \frac{d\sigma_s}{d\vec{p}_2}\, R_s\,(\vec{p}_1, \vec{p}_2)\,, \tag{3.3}$$

where the index s is a reminder for the short-lived sources and $A_c(\beta)$ is the Coulomb factor [SAKH48].

The Coulomb factor $A_c(\beta)$ is a precisely calculated function and depends on the relative velocity β of π^+ and π^- in their c.m.s.:

$$A_c(\beta) = 2\pi\eta/\left(\exp\left(2\pi\eta\right) - 1\right)\,, \qquad \eta = -\frac{\alpha}{\beta}\,, \tag{3.4}$$

where α is the fine structure constant.

The relativistic corrections to $A_c(\beta)$ do not exceed 0.5% [BAYE69] and lead only to a modification of $\eta = p_B/q$, where p_B is the Bohr momentum of $A_{2\pi}$.

The Coulomb interaction of pions with residual nucleus has an negligible influence on the correlation function because of the relativistic velocity of pions. A numerical evaluation of this effect will be obtained using approach developed in [ERAZ94].

The hadron correlation function $R_s(\vec{p}_1, \vec{p}_2)$ accounts for the pion pair production dynamics and strong interaction of the pions in the final state. In what follows we are mainly interested in the q-dependence of R_s in the interval $0 \leq q \leq 30$ MeV/c. The function R_s is parametrized in the form [URIB94]

$$R_s(q) = (1 + F(q))\, S(q^2)\,, \tag{3.5}$$

where $F(q)$ takes into account the $\pi\pi$ interaction in the final state and $S(q^2)$—the dynamics of $\pi^+\pi^-$ pair production.

The relative change of $S(q^2)$ in the range of q from 0 to 30 MeV/c is about $1.6 \cdot 10^{-3}$ [URIB94]. This result is explained by the small difference of $\pi^+\pi^-$ effective mass $M_{\pi\pi}$ from $2m_\pi$: $M_{\pi\pi} = 2m_\pi + 1.6$ MeV at $q = 30$ MeV/c.

The correlation function $F(q)$ can be obtained [KALI94] in the framework of the independent source model [KOPY72, LEDN82, LEDN90]. Figure 3.1 shows the full correlation function for detected pion pairs. We see that $F(q)$, in the interval $0 \leq q \leq 30$ MeV/c, can be described by the relation:

$$F(q) = F(0) - \xi q\,. \tag{3.6}$$

In practice, ξ is found to be independent on the model parameter and equals $\xi \approx 1.2 \cdot 10^{-3}$ (MeV/c)$^{-1}$.

To summarize this point, the hadron correlation function changes at most by $\sim 4 \cdot 10^{-2}$ in the interval $0 \leq q \leq 30$ MeV/c. This is confirmed by the experimental observation [AFAN93A].

Obviously the production cross section of the "non-Coulomb" $\pi^+\pi^-$ pairs σ_l may be written:

$$\frac{d\sigma_l}{d\vec{p}_1\, d\vec{p}_2} = \frac{d\sigma}{d\vec{p}_1\, d\vec{p}_2} - \frac{d\sigma_s}{d\vec{p}_1\, d\vec{p}_2}\,. \tag{3.7}$$

As for these pairs the Coulomb correlation is absent, the q-dependence of these pairs differs greatly from the distribution of "Coulomb" pairs at $q \leq 10$ MeV/c. This difference is taken into account in the data analysis.

The q-dependence for atomic, "Coulomb" and "non-Coulomb" pairs are shown in Figure 3.2.

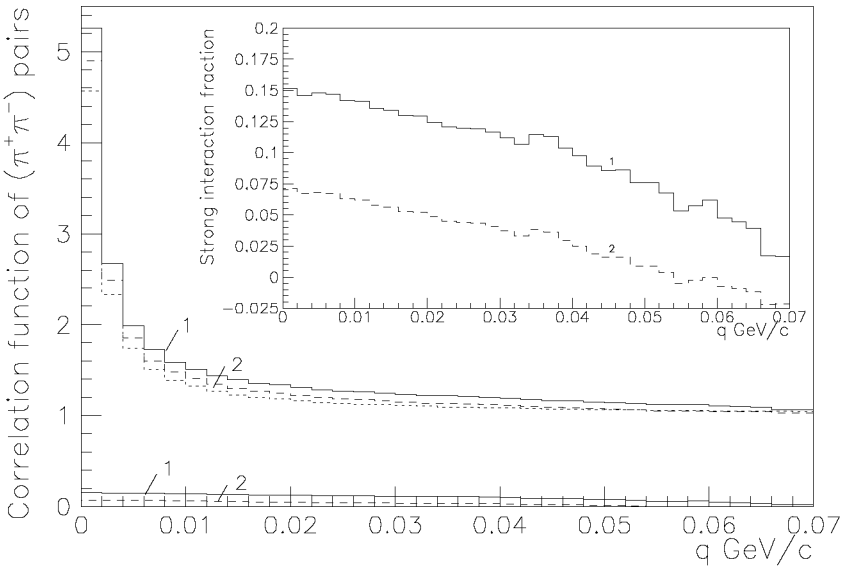

Figure 3.1: Correlation function of $\pi^+\pi^-$ versus relative momentum q for pion pairs detected in the setup. Calculations have been performed in the framework of the independent source model [LEDN82] with the spherically symmetric space-time Gaussian distribution of the pion sources. The time parameter of the Gaussian was $\tau_0 = 1.0$ fm/c and the space one was varied: $r_0 = 1.2$ fm — solid lines 1 and $r_0 = 2.0$ fm — dashed lines 2. The pure Coulomb correlation function is shown by dotted line. The correlation due to strong interaction $F(q)$ is shown at the bottom of the figure and in the insertion (larger scale).

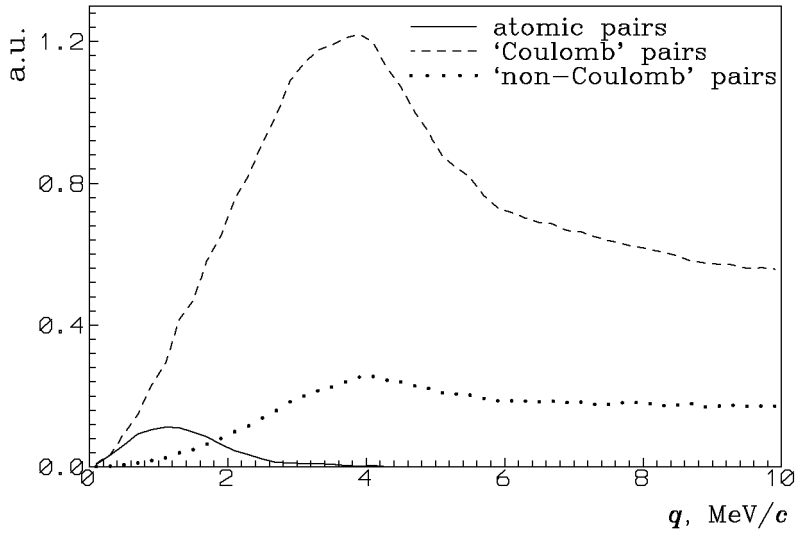

Figure 3.2: q-dependence for atomic, "Coulomb" and "non-Coulomb" pairs. The relation between the shot-lived and long-lived sources was obtained with the Lund model. The curves fall off for $q > 4$ MeV/c due to the cut on the transversal components of q: $q_X < 4.$ MeV/c and $q_Y < 3.$ MeV/c, which will be applied at data processing.

Chapter 4

Detection of relativistic $A_{2\pi}$ and lifetime measurement

4.1 Method of $A_{2\pi}$ detection

The lifetime of $\pi^+\pi^-$ atoms is very small (Section 2.4.1): $A_{2\pi}$ can only be observed by detecting $\pi^+\pi^-$ pairs from the atom breakup which occurs in the production target [NEME85].

The $\pi^+\pi^-$ pairs are produced either as free pairs or as bound states (atoms $A_{2\pi}$). The atoms may annihilate into $\pi^0\pi^0$ or break up (get ionized) into $\pi^+\pi^-$ pairs (atomic pairs) due to $A_{2\pi}$ interactions with the target atoms. The number of atomic pairs depends on the lifetime of the atoms, their breakup cross sections and the target thickness.

Let us assume that the target is made of material with an atom breakup length $\lambda_{\rm br}$, approximately equal to the atom annihilation length $\lambda_{\rm anh}$. Let first the target thickness l be much less than the breakup length: $l \ll \lambda_{\rm br}$. Then most of the atoms produced in the ground state get out of the target into vacuum and annihilate. If such a thin target for atom production is used and if the setup detects charged pions then these charged pairs will be free pairs and not atomic pairs.

If the target thickness is $l \approx \lambda_{\rm br} \approx \lambda_{\rm anh}$ the fraction of atoms which break up inside the target increases and the setup will detect, besides free pairs, some atomic pairs.

For atomic pairs arising from $A_{2\pi}$ breakup, the value of the relative momentum q in the $\pi^+\pi^-$ c.m.s. is less than 3 MeV/c with a probability of ~ 95 %. Therefore, atomic pairs have approximately equal energies $E_+ \approx E_-$ in lab system and only a small opening angle $\Theta \approx 6/\gamma$ mrad, where γ is the Lorentz-factor. In the region of small relative momenta both atomic and free pairs will be detected. The number of atomic pairs is found by subtraction. The measurement of the ratio of the atomic pair number to the full number of produced atoms or the measurement of the atomic pair number as a function of the target thickness allows to determine the atom lifetime.

4.2 Methods for $A_{2\pi}$ lifetime measurement

For a fixed target thickness and atom momentum the probability of $A_{2\pi}$ breakup is defined by the dynamics of dimesoatom interactions with the target matter and by its lifetime in the ground state τ. To obtain τ one has to obtain the numbers of produced (N_A) and broken up (n_A) atoms. Comparison of the measured breakup probability $P_{\rm br} = n_A/N_A$

with the calculated (see Section 5.3) dependence $P_{\rm br}$ on τ gives the value of the lifetime.

The measurement of n_A is realized through the analysis of the experimental distribution of $\pi^+\pi^-$ pairs. In the region $q > 3$ MeV/c there are only free pairs. This part of the spectrum is fitted with a function obtained from the experimental distribution of $\pi^+\pi^-$ accidental pairs (see below). This function depends on two parameters, their nature being clearly understood, and includes also a normalization factor. The extrapolation of the approximation function to the region $q \leq 2$ MeV/c yields the number of free pairs in this relative momentum interval and, hence, the value n_A.

The number of free pairs with low q is strictly related to the number N_A of atoms produced in the target (3.1). In this way N_A is determined.

So, the procedure of obtaining the breakup probability $P_{\rm br}$ through the measurement of n_A and N_A is based only on the analysis of the experimental $\pi^+\pi^-$ pair distributions and includes only relative measurements. The knowledge of the absolute value of the setup efficiency is not needed as the efficiency for detecting low q free pairs is the same as that for atomic pairs. The absolute number of proton interactions in the target is also of no importance as the detection of free pairs and of $A_{2\pi}$ proceeds in parallel.

Two important measurements with other targets have to be done to test fundamental aspects of the analysis. The first one is checking up the correctness of the extrapolation procedure. For this purpose a target made of beryllium will be used consisting of several thin foils with gaps between them. With this type of target the atoms mainly annihilate in the gaps and the breakup probability is very low and practically does not depend on the atom lifetime. So one should observed a small predictable number of dimesoatoms independent of τ.

The other point to be checked is the experimental verification of the correctness of the calculated breakup cross section. This can be done by means of a target made of high Z and high density material (Ta, Pt). In such a target the breakup probability and, hence, the observable value n_A is only weakly depending on τ as in this case the breakup length is much less than the annihilation length. The number of detected $A_{2\pi}$ may be compared with the calculated one without being affected by the lifetime value.

4.2.1 Method of extrapolation

The method of extrapolation was used in the experiment [AFAN93A] for the observation of $A_{2\pi}$. Besides real coincidences of π mesons, accidental coincidences of pions were also recorded. The distribution of the time difference between hits in the positive and negative particle arms contained a real coincidence peak above a uniform background from accidental coincidences. The real coincidence peak consists of atomic and free pion pairs. To obtain the distribution of real pion pairs versus relative momentum the normalized distribution of accidental pairs is subtracted from the distribution of all events in the time window of real coincidencies.

The accidental pairs are used to describe the free pion pair distribution as the accidental $\pi^+\pi^-$ pair distribution $dN_a^{\pi\pi}/dq \equiv \Phi(q)$ coincide with the free $\pi^+\pi^-$ pair distribution $dN_{\rm r}^0/dq$ without taking into account final state interactions. This follows from the fact that both distributions are proportional to the product of the single inclusive production cross sections of π^+ and π^- mesons [GRIS82]. The distribution $\Phi(q)$ is obtained from the accidental event distribution dN_a/dq by subtraction of the π^-p and πK accidental pairs, their small contribution being measured by means of the time-of-flight technique during a calibration run.

The distribution $\Phi(q)$ is the sum of the pair distribution $\Phi(q)w_s(q)$ from short-lived sources (pairs from direct processes and from decays of ρ, w, Δ, ...) and of the pair distribution $\Phi(q)[1 - w_s(q)]$ from long-lived sources (one or both π mesons arising from η or K_s^0 decays). Here the weight $w_s(q)$ is the probability that two pions in an accidental pair originate from short-lived sources. For the simulation $w_s(q)$ is taken from the Lund model. For data analysing $w_s(q)$ will be obtained using accidental pair distributions only. An estimation of an systematical error in this approach is discussed in Section 13.1.5.

The Coulomb interaction in the final state is taken into account by multiplying $\Phi(q)w_s(q)$ with the Coulomb factor $A_c(\beta)$. The pion pairs from long-lived sources do not interact in the final state, and therefore no correction is applied to the distribution $\Phi(q)[1 - w_s(q)]$.

From the above we can write:

$$G(q) = N\Phi(q)\left\{w_s(q)A_c(\beta)\,(1 + aq) + f[1 - w_s(q)]\right\} \ , \tag{4.1}$$

where N is a normalization factor; f is a free parameter which accounts for the uncertainty of $w_s(q)$; the factor $(1+aq)$ takes into account strong interaction effects in the final state (see Eq. (3.6) and Section 13.1.4) and a is a free parameter. With such a description of the data the particle production dynamics as well as the setup efficiency are taken into account.

The experimental distribution $dN_{\rm r}/dq$ is fitted for $q > 3$ MeV/c (where atomic pairs are absent) by the distribution (4.1). The number of atomic pairs is determined by the difference between the number of $\pi^+\pi^-$ pairs measured in the interval $q < 2$ MeV/c and the corresponding number of free pairs, obtained for $q < 2$ MeV/c by extrapolaton of the distribution (4.1) which fits the data in the region $q > 3$ MeV/c.

The equations (3.1–3.4) give the possibility to calculate the total number of produced $A_{2\pi}$ by means of the experimental number of Coulomb pairs. The spectrum of $A_{2\pi}$ may be obtained by also using (3.1). The ratio of the atomic pair number to the number of produced $A_{2\pi}$ is the so-called $A_{2\pi}$ breakup probability $P_{\rm br}$. In Figure 5.1 the $A_{2\pi}$ breakup probability is shown as a function of the atom lifetime for different target materials. From the measured value $P_{\rm br}$, one can therefore determine the $A_{2\pi}$ lifetime.

4.2.2 Subtraction method

To measure the dimesoatom lifetime in another way one can use the subtraction method based on the use of three targets (for details see Appendix C). The targets T_1, T_2 and T_3 are made of the same material and have the same total thickness but they consist of 1, k_2 and k_3 $(1 < k_2 < k_3)$ layers separated with gaps. In the case of T_3 most of the $A_{2\pi}$ produced in any layer annihilate between this layer and the next one.

If experimental data are accumulated for the same number of interactions in each of the three targets, one has for all targets the same number of free pairs N_f, but different numbers of atomic pairs n_A, as the probability of $A_{2\pi}$ breakup differs for the three targets. The value $x = (N_2 - N_3)/(N_1 - N_3)$, where $N_i = N_{fi} + n_{Ai}$, actually depends on n_A only and consequently on the $A_{2\pi}$ lifetime.

This method requires more statistics than the extrapolation method for a lifetime measurement of the same precision, but is free from the assumptions made in the extrapolation method concerning the shape of the free pair spectrum.

A similar method was applied in the π^0 meson lifetime measurement [ATHE85] where two targets in three different distances between them were exposed to the beam.

Chapter 5

Interaction of relativistic $A_{2\pi}$ with matter

The interaction of $A_{2\pi}$ with matter is of great importance for the experiment as the $A_{2\pi}$ breakup is involved in the procedure of lifetime measurement. So the corresponding cross sections have to be known with high precision. To measure the atom lifetime with a precision of 10% the probability of its must be known with a precision not worse than a few percent.

5.1 Interaction cross section of $A_{2\pi}$ with atoms

After production in hadron-nucleus interaction the $A_{2\pi}$ atom is moving in the target material. Electromagnetic interaction cross sections of $A_{2\pi}$ in the ground state with atoms are of the order of 10^{-20} cm^2. We shall neglect the strong interaction between $A_{2\pi}$ and nuclei of the target atoms.

Electromagnetic cross sections depend on the charge as Z^2, so the interaction cross section of $A_{2\pi}$ with atom electrons is Z times smaller than with nuclei. The exact calculation performed for interaction of $A_{2\pi}$ with different materials [AFAN91B] shows that the precision of this simple estimation is sufficient. For target materials with Z about 30 which are considered below the account of interaction with atom electrons (so called incoherent scattering) increases the cross sections by ~3–4%. Now we do not take into account this influence but it will be considered for precise calculations. One should note that this influence corresponds to the upper limit of the uncertainty of all present calculations.

The atom $A_{2\pi}$ interacts predominantly with the electric field of the nuclei (Coulomb interaction). There is also an interaction of $A_{2\pi}$ with magnetic fields due to Lorentz boosts. As shown in [MROW87, DENI87] for the interaction of relativistic $A_{2\pi}$ with Cu the total cross section of the magnetic interaction is 0.6% of the electric one and should be considered in precise calculations.

To describe the Coulomb interaction of a hydrogenlike atom with other atoms we used the first Born approximation (see for example [GILL78]) which considers only single photon exchange. The precision of this approach can be estimated as $(Z\alpha)^2$ (α is the fine structure constant) so for target materials with Z about 30 this leads to 4%. Other calculation methods are available, such as the Coulomb-modified Glauber approximation,

allowing to take into account all multiphoton exchanges and so providing much higher accuracy [TARA91]. It is shown [TARA91] that all cross sections within this approach are smaller than the corresponding ones in the Born approximation by a value not exceeding the estimated accuracy of the latter one.

In the first Born approximation the excitation (transition between discrete states i and f) and total cross sections of atom-atom interactions are expressed via atom form factors:

$$\sigma_i^f = 4\pi \frac{(Z\alpha)^2}{\beta^2} \int_0^\infty \left(1 - \frac{F_t(q)}{Z}\right)^2 |F_i^f(q/2)|^2 \frac{dq^2}{q^4} \tag{5.1}$$

$$\sigma_i^{tot} = 8\pi \frac{(Z\alpha)^2}{\beta^2} \int_0^\infty \left(1 - \frac{F_t(q)}{Z}\right)^2 \left(1 - F_i^i(q)\right) \frac{dq^2}{q^4} \tag{5.2}$$

Here β is velocity of $A_{2\pi}$ ($\hbar = c = 1$), i and f denote the initial and final states of $A_{2\pi}$, $F_i^f(q)$ is the transition form factor of $A_{2\pi}$, $F_t(q)$ is the atomic form factor of the target atom and q is transfer momentum.

For the $A_{2\pi}$ form factors $F_i^f(q)$ we used exact analytic expressions (see [AFAN93C]) and for target atom form factors $F_t(q)$ the Moliére parametrization of the Thomas-Fermi potential [MOLI47] (T.F.M.). There exists also a more accurate representation of these form factors based on the self-consistent field method of Hartree-Fock [HUBB75, HUBB79]. Calculations performed for interactions of $A_{2\pi}$ with various materials using these two methods [AFAN91B] showed that the uncertainty of the cross sections calculated within the T.F.M. parametrization is about 1% for the $A_{2\pi}$ ground state and slightly more for excited states.

Thus we calculated the excitation and total cross sections for $A_{2\pi}$ interaction with target atoms with an uncertainty not greater than 4%. This value will be reduced with methods discused above.

5.2 Description of $A_{2\pi}$ passing through the target material

In this section we calculate the probability of the $\pi^+\pi^-$ pair yield from the $A_{2\pi}$ breakup inside the target (probability of $A_{2\pi}$ breakup). (For details see Appendix A.)

Using the calculated total and excitation cross sections we can describe the evolution of the atomic state populations during the passage of $A_{2\pi}$ through the target by a set of differential equations. The lifetime and momentum of $A_{2\pi}$ are parameters of the equation set. Since $A_{2\pi}$ can get excited or deexcited in the interaction, an exact solution for any state may only be obtained as a solution of the infinite set of equations. Hence we have to limit the set of equations in order to get a solution ($n \leq 7$).

Populations of all states, with the principal quantum number $n \leq 7$, as a function of the path in the target have been found and so the summed population $P_{\rm dsc}$ of all discrete states with $n \leq 7$. This function takes into account the interaction of $A_{2\pi}$ with target atoms and the $A_{2\pi}$ annihilation.

The summed population P_{tail} of all other atomic states, that are not included in the equation set ("tail" with $n > 7$), has been estimated using the asymptotical behaviour of discrete state population over n.

The $A_{2\pi}$ atoms annihilate mainly from 1S state (2.19). The population of the first few states is known with high accuracy and thus the probability of $A_{2\pi}$ annihilation (P_{anh}), too.

Having calculated the probabilities for $A_{2\pi}$ to remain in one of discrete states or to annihilate, while passing through the target, the remainder, that is probability of $A_{2\pi}$ breakup, P_{br}, is given by

$$P_{\text{br}} = 1 - P_{\text{dsc}} - P_{\text{tail}} - P_{\text{anh}} \,. \tag{5.3}$$

In such a way we can calculate the probability of $A_{2\pi}$ breakup in any target for arbitrary values of the atom momentum and lifetime.

In Table 5.1 the values P_{dsc}, P_{tail}, P_{anh} and P_{br} are given for various thicknesses of the Ti target. The $A_{2\pi}$ lifetime was assumed to be $3.7 \cdot 10^{-15}$ s. Calculations were performed for 4.7 GeV/c $A_{2\pi}$ momentum corresponding to the mean value for the setup. (This momentum value is used in all further calculations.) The accuracy of P_{br} calculations is estimated to be not worse than 0.5%.

Table 5.1:

S μm	P_{dsc}	P_{tail}	P_{anh}	P_{br}
70	0.219	0.004	0.497	0.280
175	0.088	0.002	0.569	0.341
263	0.059	0.001	0.586	0.354
351	0.044	0.001	0.594	0.361
439	0.035	0.0006	0.598	0.366

In the approach discussed above we neglected two effects. The first one is the formation time of atomic states. This time is low in comparison with the time between subsequent collisions and therefore all states are considered to be already formed. This assumption is valid for levels with principal quantum numbers $n \leq 7$. Secondly we neglect a possible interference between atomic states with equal quantum numbers n and m and with orbital quantum numbers l which differ by $\Delta l = 2$. This interference occurs due to Coulomb degeneracy of atomic states. Its influence cannot be significant because the interference is possible only for states with $n \geq 3$ which have small populations. These two effects could be taken into account if one describes the atom evolution by quantum mechanical equations in terms of density matrix elements.

5.3 Probability of $A_{2\pi}$ breakup as a function of the atom lifetime. Target choice for the method of extrapolation

Using the method discussed above we calculated the probability of $A_{2\pi}$ breakup for various targets. To compare different targets they have to be equivalent with respect to

multiple scattering as this leads to equal accuracy in the procedure of $A_{2\pi}$ selection. We thus consider sets of targets having equal S/x_0 ratio, where x_0 is the radiation length and S is the target thickness. In Figure 5.1 the probability of $A_{2\pi}$ breakup as a function of the atom lifetime is shown for a set of various material for targets equivalent to 20 μm of Ta.

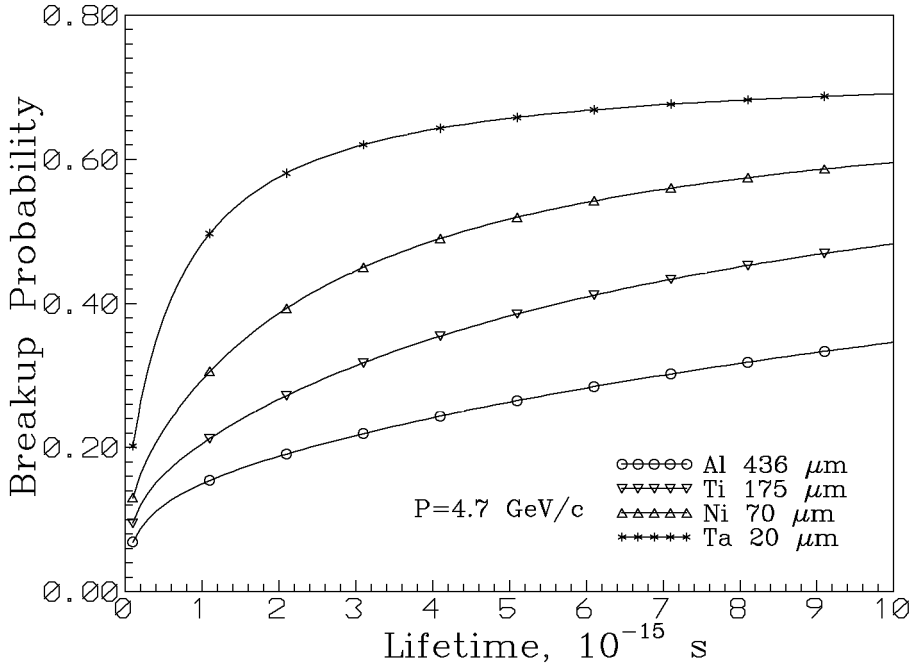

Figure 5.1: Probability of the $A_{2\pi}$ breakup as a function of the atom lifetime for different materials of targets having equal thickness in radiation length units.

From such functions one can calculate the required precision in the measurement of the breakup probability. In Figure 5.2 the relative accuracy of the breakup probability $\delta P_{\rm br}$, required to obtain the $A_{2\pi}$ lifetime with an accuracy of 10%, is shown as a function of target nucleus charge Z for different targets and thicknesses. The thicknesses were chosen to have the same S/x_0 ratio as for tantalum foils of 8, 20 and 50 μm. Solid lines are drawn between points for equivalent thicknesses. The data correspond to the lifetime value predicted by chiral perturbation theory: $3.7 \cdot 10^{-15}$ s.

Using the results from the calculation of $A_{2\pi}$ and $\pi^+\pi^-$ pair production (Chapter 9) and from the simulation of the setup performance (Chapter 10) as well as the precision of $A_{2\pi}$ selection with the method of extrapolation (Section 4.2.1), we can evaluate the number of $A_{2\pi}$ which has to be produced in the target in order to achieve the required precision in $P_{\rm br}$ and thus in lifetime measurements. In Figure 5.3 the number of $A_{2\pi}$, to be produced to obtain the $A_{2\pi}$ lifetime within 10%, is shown as a function of target nucleus charge Z for different targets (the same targets as in Figure 5.2). In this calculation the ratio of accidental to real coincidences in the setup was assumed to be 2.0, close to the expected one (Chapter 11 Table 11.1).

From Figure 5.3 ($A_{2\pi}$ lifetime of $3.7 \cdot 10^{-15}$ s) one sees that the smallest required number of produced $A_{2\pi}$ is for the iron target of 215 μm (equivalent to 50 μm of tantalum). However the minimum is not deep, and for the choice of the target material and thickness some other considerations should be taken into account (e.g. feasibility of the target

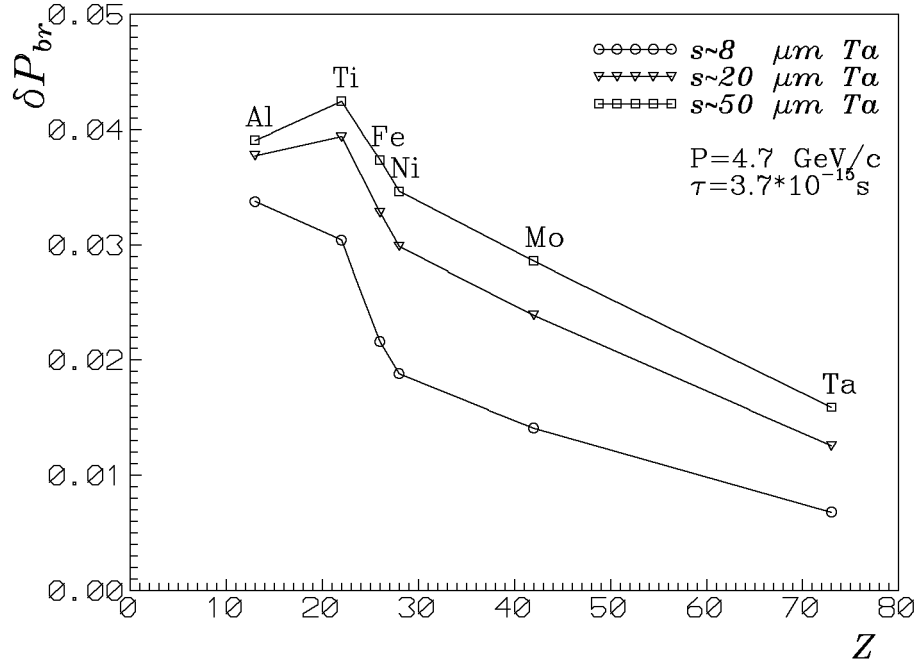

Figure 5.2: The relative accuracy of the breakup probability $\delta P_{\rm br}$ required to obtain the $A_{2\pi}$ lifetime within 10% as a function of the target nucleus charge Z for different thicknesses of targets. Solid lines are drawn between points for equivalent target thicknesses.

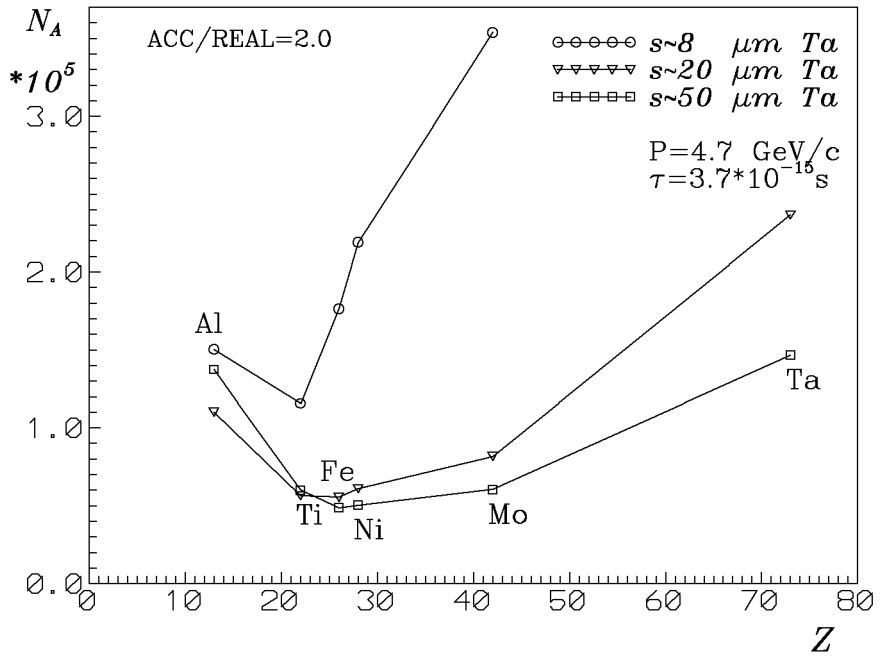

Figure 5.3: The number of $A_{2\pi}$ to be produced in the target to obtain the $A_{2\pi}$ lifetime within 10% as a function of target nucleus charge Z for different targets and thicknesses. Solid lines are drawn between points for equivalent targets thicknesses.

manufacturing, production of background not considered in the simulation etc.)

In Figure 5.4 the number N_A versus the ratio of accidental to real coincidences is shown for targets equivalent to 20 μm of tantalum. This figure illustrates the importance of accidental coincidences for the lifetime measurement in the case of the extrapolation method.

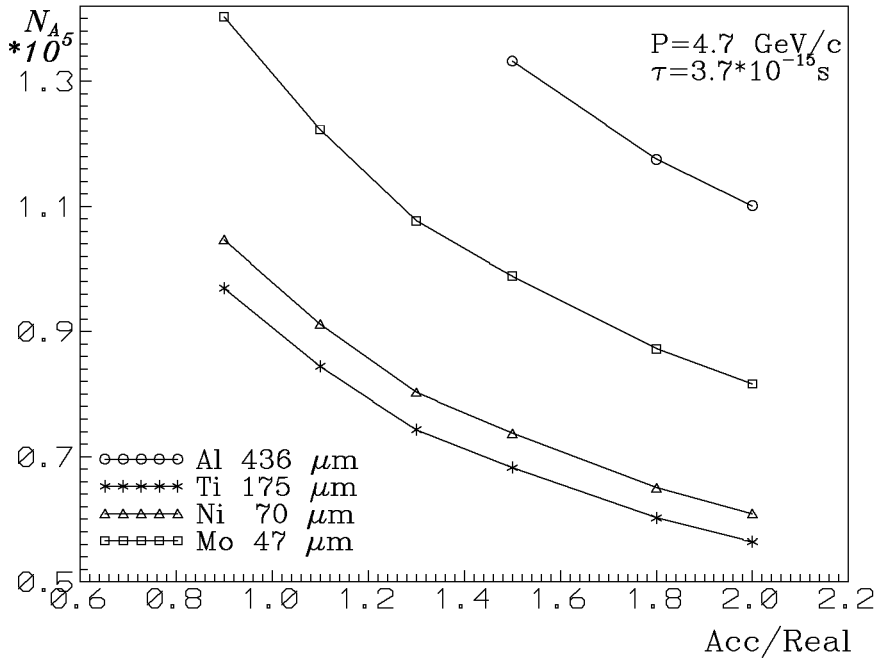

Figure 5.4: The number of $A_{2\pi}$ to be produced in the target to obtain the $A_{2\pi}$ lifetime within 10% versus the ratio of accidental to real coincidences for targets equivalent to 20 μm of tantalum.

In Figure 5.5 the number of $A_{2\pi}$, to be produced in the target to obtain the $A_{2\pi}$ lifetime within 10%, is shown as a function of the atom lifetime for targets equivalent to 20 μm of tantalum and the ratio of accidental to real coincidences equal to 2.0. For a wide range of the $A_{2\pi}$ lifetime there are target materials which require approximately the same minimal numbers of produced $A_{2\pi}$ to measure the lifetime within 10%.

Let us summarize this discussion with some illustrative and final numbers in Table 5.2. For different materials with nucleus charge Z and for the ground state of $A_{2\pi}$ the total cross sections σ_{1S}^{tot} and corresponding interaction lengths $\lambda_{\rm int} = A/\sigma_{1S}^{tot}\rho N_0$ are given. Calculations were performed for the $A_{2\pi}$ lifetime $3.7 \cdot 10^{-15}$ s and momentum 4.7 GeV/c, leading to an annihilation length $\lambda_{\rm anh} = 18.7\,\mu$m. For targets with thicknesses S, which are equivalent in radiation lengths to 20 μm of tantalum, the following numbers are found: the probabilities of $A_{2\pi}$ annihilation $P_{\rm anh}$ and of breakup $P_{\rm br}$, the relative accuracy in $P_{\rm br}$ measurement $\delta P_{\rm br}$ and the number of produced atoms N_A, required to obtain the lifetime within 10%. One can see that targets in the range from Ti to Cu require approximately the same number N_A. From Figure 5.5 one can conclude that the Ti target is the most suitable for the $A_{2\pi}$ lifetime measurement for the wide range of the lifetime from 3.5 to $9 \cdot 10^{-15}$ s. If, however, a smaller value of the lifetime is found, targets with high Z should be used.

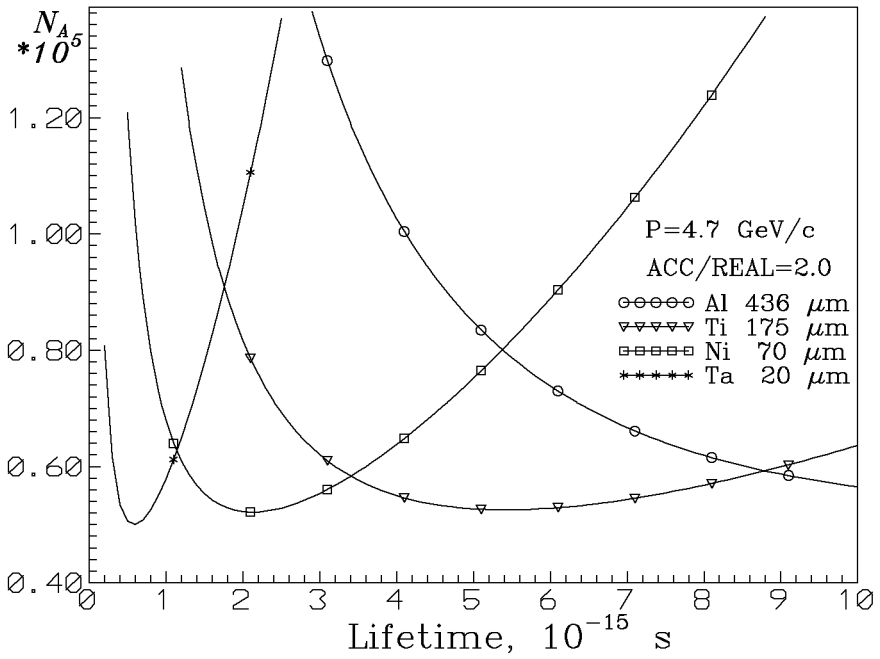

Figure 5.5: The number of $A_{2\pi}$ to be produced in the target to obtain the $A_{2\pi}$ lifetime within 10% as a function of atom lifetime for different targets equivalent to 20 μm of tantalum.

Table 5.2:

	Z	σ_{1S}^{tot} cm^2	$\lambda_{\rm int}$ μm	S μm	$P_{\rm anh}$	$P_{\rm br}$	$\delta P_{\rm br}$	N_A
Be	04	$1.35\cdot10^{-22}$	600.	1723.	0.840	0.139	$3.1\cdot10^{-2}$	$6.6\cdot10^5$
Al	13	$1.29\cdot10^{-21}$	128.	436.2	0.717	0.234	$3.8\cdot10^{-2}$	$1.1\cdot10^5$
Ti	22	$3.53\cdot10^{-21}$	49.7	175.4	0.569	0.341	$3.9\cdot10^{-2}$	$5.6\cdot10^4$
Fe	26	$4.86\cdot10^{-21}$	24.1	85.9	0.420	0.444	$3.3\cdot10^{-2}$	$5.5\cdot10^4$
Ni	28	$5.60\cdot10^{-21}$	19.4	69.5	0.374	0.476	$3.0\cdot10^{-2}$	$6.1\cdot10^4$
Cu	29	$5.97\cdot10^{-21}$	19.6	70.1	0.375	0.475	$3.0\cdot10^{-2}$	$6.1\cdot10^4$
Mo	42	$1.21\cdot10^{-20}$	12.8	46.9	0.290	0.534	$2.4\cdot10^{-2}$	$8.2\cdot10^4$
Ta	73	$3.47\cdot10^{-20}$	5.18	20.0	0.148	0.635	$1.3\cdot10^{-2}$	$2.4\cdot10^5$
Re	75	$3.65\cdot10^{-20}$	4.01	15.5	0.119	0.655	$1.0\cdot10^{-2}$	$3.5\cdot10^5$
Pt	78	$3.93\cdot10^{-20}$	3.84	15.0	0.114	0.659	$9.8\cdot10^{-3}$	$3.8\cdot10^5$

Chapter 6

Proton beam and secondary particle channel

6.1 General description

The experimental setup will be placed in the south part of the PS East Hall at the proton beam line ZT7. A schematic view of the proton channel and the experimental setup is shown in Figure 6.1. Channel optics function is shown in Figure 6.2. Figure 6.3 depicts top and side views of the experimental setup in detail.

The proton beam extracted from PS is focused on the target of the experimental setup. Then the beam passes between the poles of the spectrometer magnet close to the lower one and is absorbed in the catcher downstream of the setup.

The secondary particle channel is arranged at 3.5° relative to the proton beam. Atomic and free $\pi^+\pi^-$ pairs arising in the target are detected with coordinate detectors placed before the spectrometer magnet and with two telescopes behind the magnet.

The coordinate detectors are the scintillation fibre detector with position sensitive photomultipliers and the scintillation hodoscope for the double energy loss measurement.

The telescopes consist of drift chambers, scintillation hodoscopes, gas Cherenkov counters and μ-identifiers. The last are made up of cast-iron absorbers and scintillation counters. The Cherenkov counters are used to suppress detection of electrons and μ-identifiers — muons.

6.2 The proton beam line ZT7

The proton beam line is described in detail in Appendix D. The ZT7 area uses the PS slow extraction channel SE61. The energy of the ZT7 beam equals 24 GeV and its intensity for proposed experiment needed is about 10^{11} protons per spill.

The spill length is actually equal to 350 ms and it can be increased up to 450 ms. During the slow extraction the beam momentum increases by 0.3%.

6.2.1 Magnetic and vacuum elements of the channel

The magnetic channel (Figure 6.1) consists of two quadrupole doublets separated by a string of dipoles [DURI94] and of feedback-controlled correction magnets to tune the

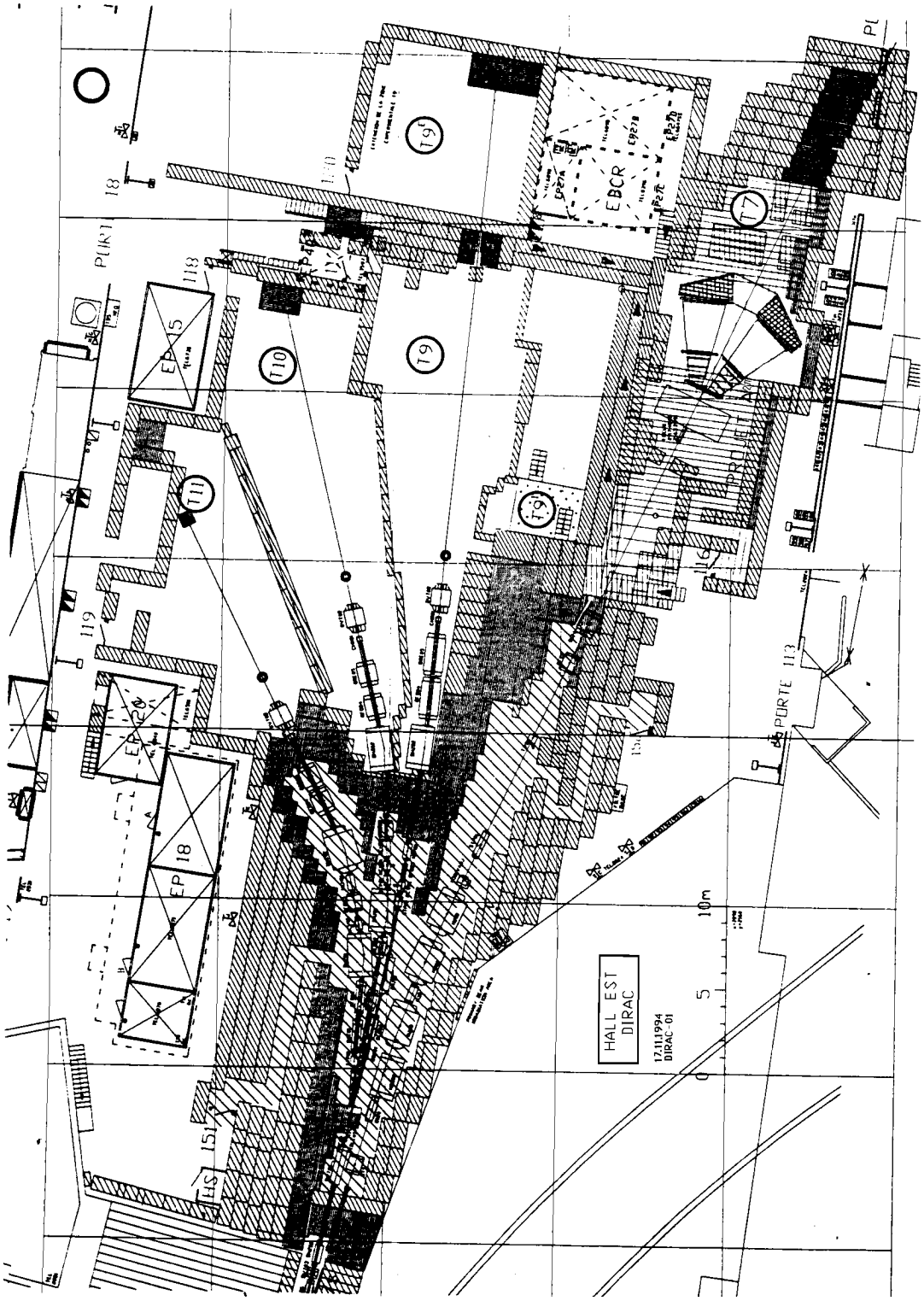

Figure 6.1: The PS East Hall with the proton beam line ZT7 and the experimental setup.

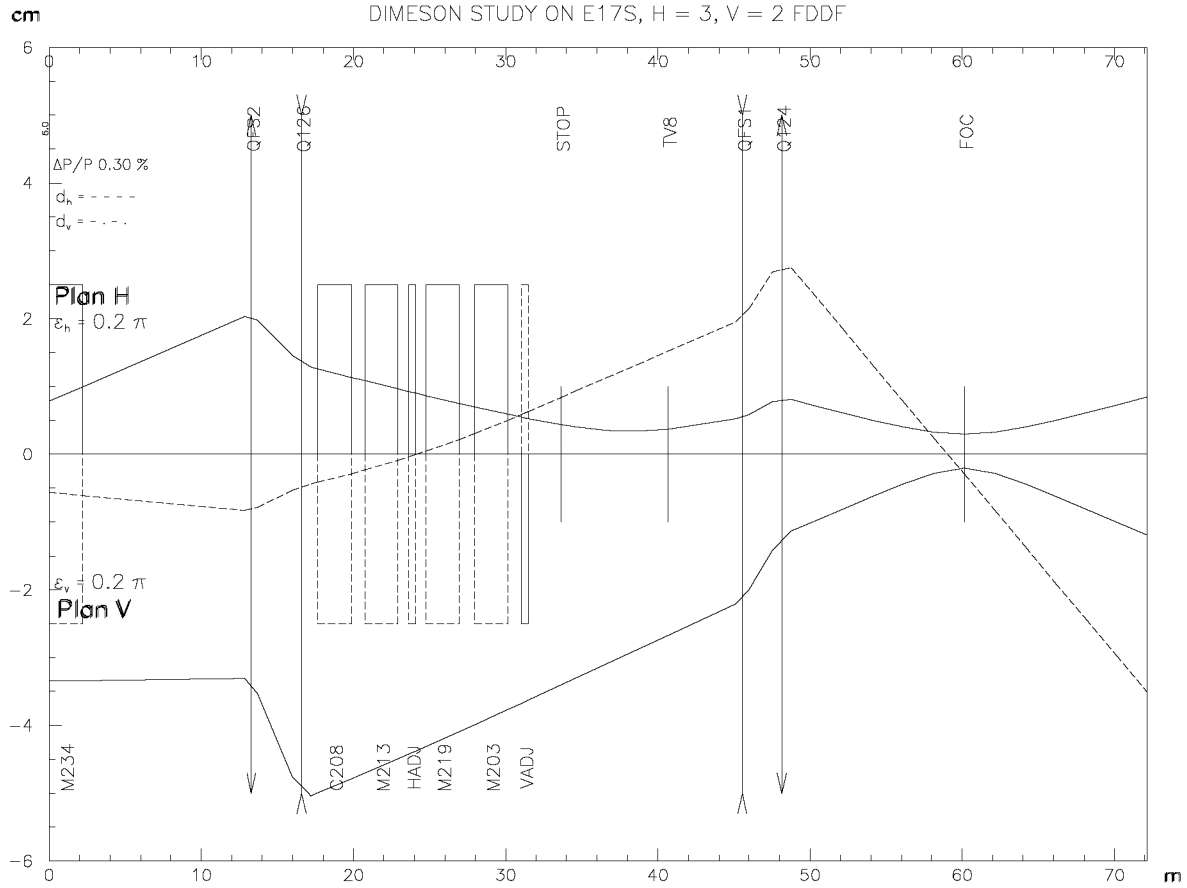

Figure 6.2: Channel optics function.

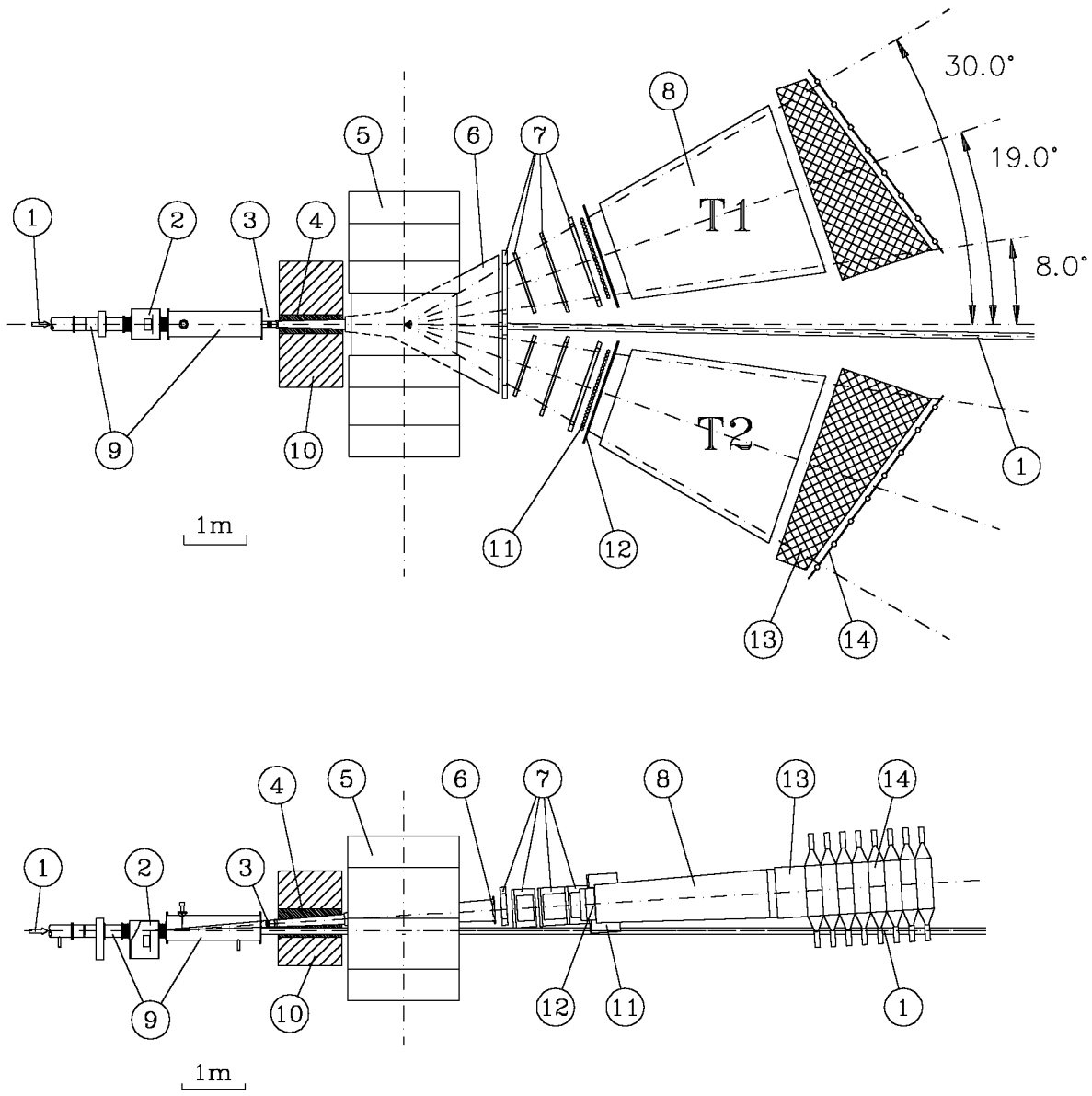

Figure 6.3: Experimental setup: 1 — proton beam, 2 — target device, 3 — coordinate detectors, 4 — collimator, 5 — spectrometer magnet, 6 — vacuum chamber, 7 — drift chambers, 8 — Cherenkov counters, 9 — sections of the vacuum pipe, 10 — radiation shield, 11 — vertical hodoscopes, 12 — horizontal hodoscopes, 13 — cast-iron absorbers, 14 — muon scintillation counters.

proton beam location on the target. Stability of the beam centre of gravity at the target of about 0.5 mm or better is needed inside the spill and from spill to spill.

The magnetic elements of the channel allow to obtain horizontal H and vertical V dimensions of the beam on the target: $H = 3$ mm, $V = 2$ mm at the 2σ level (Figure 6.2). The focus position can be shifted 2 m upstream by simply changing the currents in the quadrupoles. The beam divergence is ± 1 mrad.

The experiment is sensitive to the beam distribution far from the core. Level of the beam halo must be low to diminish a counting rate of the coordinate detectors located off the axis of the proton beam.

The proton beam passes in the vacuum. For mounting and change of the targets the CERN target device of "Marguerite" type will be used. The target device is connected with the vacuum tube through the vacuum valve and bellows. The vacuum volumes are evacuated down to 10^{-2} Torr with the backing pumps.

The proton beam downstream of the target passes in the vacuum also through a hole in the radiation shield and between the poles of the spectrometer magnet close to the lower pole.

In the magnet the proton beam is deflected in horizontal plane up to the angle $\pm 1.3°$ in accordance with the value and polarity of the magnetic field. So the flexible vacuum tight connection of the tube in the magnet centre is envisaged in order to keep the proton beam in the tube at any value of the magnetic field.

The vacuum tube for the proton beam downstream of the magnet is ended with a thin outlet window near the catcher where the proton beam is absorbed.

6.2.2 Catcher

The proton beam is absorbed in the catcher consisting of iron and concrete (Figure 6.1). The catcher dimensions were determined by the PS division. The central part of the catcher about 1 m high and 2 m wide is made of iron.

Swing of the beam in front of the catcher at change of the polarity of the spectrometer magnet field is equal to 66 cm, i.e. the beam at both polarities of the field gets into the catcher.

An additional concrete shield in front of the catcher with a horizontal narrow slot for the beam must be foreseen in order to reduce back-scattering particles from the catcher. At a fixed value of the magnetic field the slot in the horizontal plane may be diminished by insertion some concrete blocks.

When the proton beam hits the catcher a flux of neutrons is produced in the direction of the setup which increases a counting rate of the detectors. So a wall of concrete of about 2 m thick will be made nearby the detectors that will reduce a background from the catcher to acceptable level. The wall has a hole for the proton beam and a possibility must be foreseen to make this hole smaller in order to reduce the neutron flux through it.

To estimate the wall thickness the results of measurements of neutron flux from the catcher (24 GeV proton beam dump) carried out in the transfer tunnel TT5 [TUYN72] and the absorption lengths in concrete for neutrons of various energies have been used. We have obtained that for our setup the increase of counting rate of any detector due to neutrons is less 10% if the concrete wall thickness is 2 m.

6.2.3 Proton beam position, profile and intensity measurements

After extraction the proton beam passes 20 cm in an air gap where a secondary emission chamber (SEC) is installed for intensity measurements and then the beam enters forevacuum channel. The SEC is calibrated in a fast extraction mode of the ejection with help of a charge transformer. The accuracy of intensity measurement with the transformer is $\pm 2\%$.

Measurements of the intensity (flux/per spill), position, profile and halo of ZT7 proton beam will be performed in three positions along the beam: after the splitter, in the immediate region of the target and at the end of the vacuum tube downstream of the setup. Permanent measurement of the beam intensity after the splitter is performed with a standard SEC.

The position of the proton beam, its profile on the target and intensity will periodically be controlled during the runs. Rough measurement of the beam position on the target is achieved with a luminescence screen that is mounted on the holders of the target device "Marguerite". The luminous spot arising from the beam interaction with the screen is observed by means of a TV camera. The luminescence detector is fabricated in the form of a grid made of 10 μm diameter berillium copper wires with 100 μm pitch. The wires are covered with inorganic phosphor, ZnS for example. Transparency of the grid is 95%.

The basic measurement of the beam profile and position on the target is provided by a special secondary emission chamber. The number of wires in the device is 20 in horizontal and the same in vertical planes, spacing between wires is 0.5 mm. So the whole spatial interval covered is ± 5 mm.

This unit will be placed in the vacuum box of the target device and inserted in the beam for the time of measurements. This chamber has additional electrodes made of foils to measure beam intensity also. After the measurement has been carried out the chamber is retracted from the beam and halo because the numbers of proton interactions with SEC and the main targets are comparable.

To monitor the intensity and profile of the beam downstream of the spectrometer magnet both in horizontal and vertical planes the secondary emission chamber fastened at the outlet of the tube will be used. This SEC can be similar to that described above.

Permanent relative measurement of the number of protons interacting with the target is performed with a scintillation counter telescope placed above the shielding roof. The telescope detects charged particles emitted from the target at the angle of 90°.

6.3 Secondary particle channel

The channel for secondary particles is arranged at an angle of 3.5° with respect to the proton beam (Figures 6.3, 6.5). The secondary particles arising in the target go through the upper part of the space between the magnet poles. At such geometry the coordinate detectors may be placed at quite a large distance to the proton beam.

The distance between the target and the magnet centre is equal to 4 m. The channel aperture is $\pm 1.5°$ in horizontal and vertical planes. Hence the beam cross section in the magnet centre (when the magnetic field is turned off) is a square of 21×21 cm^2 dimensions.

The secondary particle momentum distribution at the angle of 3.5° has a maximum that gets into the dynamical range of the main detectors.

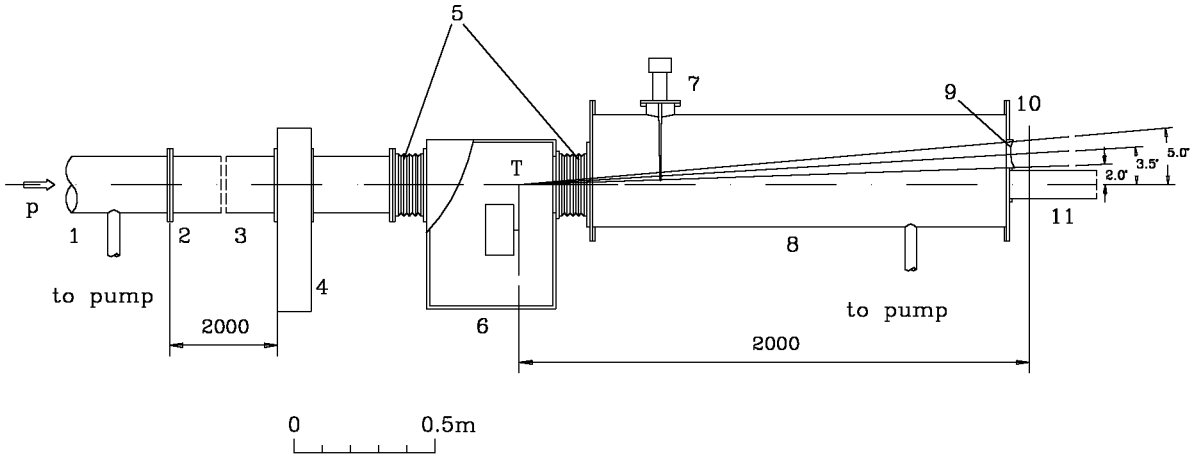

Figure 6.4: Proton beam vacuum tube, target device and vacuum tube for primary and secondary particle beams: p — proton beam, T — target, 1 — vacuum tube, 2 — flange with aluminium seals for quick junction, 3 — vacuum tube of 2 m long, 4 — vacuum valve with 150 mm body–size hole, 5 — bellows, 6 — target device of "Marguerite" type, 7 — scintillation counter for calibration measurements, 8 — vacuum tube, 9 — thin vacuum tight window of square section, 10 — blank flange, 11 — proton beam vacuum tube.

6.3.1 Initial part of the channel

The initial part of the channel for secondary particles is shown in Figure 6.4. In the experiment we shall use targets of different thicknesses made of different materials and they will be exchanged during a run.

Consequently in the target device there will be foreseen a target changing mechanism. Now we intend to use a target device of "Marguerite" type which will be connected with the proton beam pipe by means of bellows.

The target control system must carry out a change of the targets after a few spills so that the measurement conditions should be the same for all targets. The rate of change of the targets will depend on the stability of the accelerator running.

The type of the target settled in the beam must be identified unambiguously and remotely by means of TV camera. Possibility one should foresee to inspect the target visually.

In the distance between the target and the coordinate detectors the proton and secondary particle beams pass in the common vacuum tube (Figure 6.4). This tube has a big cross section in order to reduce the particle scattering on the tube walls into the setup aperture. For analogous reasons one must avoid installation of a radiation shield around the tube.

Along this section a weak leakage field of the spectrometer magnet exists. This field distorts trajectories of the atomic pairs and hence leads to errors in measuring of transversal components q_x and q_y of the relative momenta of pairs. So the measurements of the weak magnetic field along the section must be carried out to introduce corresponding corrections in q_x and q_y. Magnetic shield of the channel will probably be needed for reduction of the magnetic field to a tolerable level.

At the end of the pipe there is a thin foil window for the secondary particle beam.

A scintillation counter will be settled near the target in the secondary particle beam. The counter will be used prior to the main measurements for determination of K meson

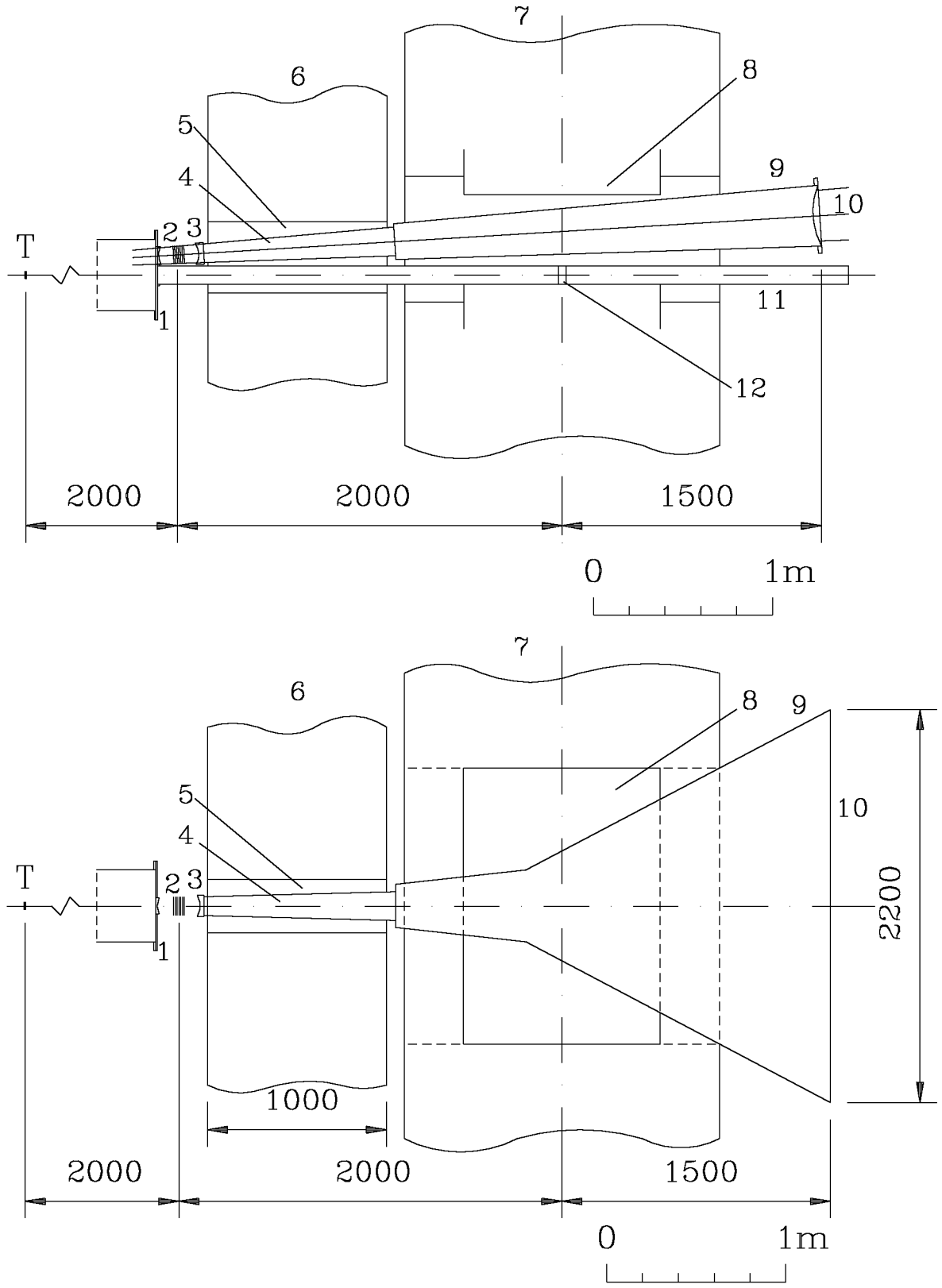

Figure 6.5: Secondary particle vacuum channel: T — target, 1 — blank flange, 2 — coordinate detectors, 3 — thin inlet window, 4 — vacuum tube of square section, 5 — collimator, 6 — radiation shield, 7 — spectrometer magnet, 8 — magnet pole, 9 — flat vacuum chamber, 10 — thin outlet vacuum window, 11 — proton beam vacuum tube, 12 — flexible connection.

and proton amount with respect to π meson yield with help of time-of-flight method.

After the thin window there is an air gap. Into the air gap the coordinate detectors (Chapter 7) will be settled. The function of the coordinate detectors is a precise measurement of coordinates of particles passing through the detectors.

6.3.2 Collimator, radiation shield and vacuum

Another vacuum volume begins with the inlet window of 105 mm square (Figure 6.5). The air gap between this window and the window placed on the blank flange of the wide tube is about 100 mm. The tube after the air gap, placed immediately in front of the spectrometer magnet, has a square cross section with the opening angle $\pm 1.5°$ both in horizontal and vertical planes.

Around this section of the vacuum channel and the nearest part of the proton vacuum tube there are laid blocks of non-magnetic material (stainless steel, for example) in order to form the outside surface of rectangular shape. This vacuum section together with the blocks is named here as a collimator. The collimator determines the angular aperture of the setup. Outside the collimator a radiation shield from lead of about 1 m thick will be placed. An additional shield can also be placed between the magnetic coils of the magnet.

Parts of the tube of square cross section must be enlarged outside both ends of the collimator to lessen the amount of particles scattered on the tube walls.

Inside the interpole space of the spectrometer magnet the vacuum tube of square cross section turns out into the large vacuum chamber with the flat walls. The angular opening of the chamber in the vertical plane is $\pm 1.5°$. In the horizontal plane the chamber dimension at the outlet of the magnet is as large as the transversal dimension of the magnet poles (153 cm). The chamber walls are fastened with stiffening ribs. The chamber has a large thin window of 200×35 cm^2 on its outlet. For the vacuum window an aluminium alloy of 0.5 mm thick will be used.

The tube of the square cross section and the large flat chamber may be made as a whole or of two parts connected close to the magnet centre that may facilitate their manufacturing.

The vacuum volume of the channel placed inside the radiation shield and between the magnet poles is independent of the rest of vacuum volume and it is pumped with a separate backing pump to a pressure of 10^{-2} Torr. The vacuum is measured with a Pirani gauge.

All parts of the secondary particle channel must be manufactured from non-magnetic material.

6.3.3 Spectrometer magnet

A magnet of type MNP21 will be used. The magnet parameters are listed in the table.

Interpole gap	— 50 cm
Pole width (across the secondary beam)	— 153 cm
Pole length	— 110 cm
Magnetic field value	— 1.65 T
Parameters of the current source	
Current	— 2500 A
Voltage	— 500 V
Power	— 1430 kW
Weight	— 110 tons

At the entrance and the outlet of the magnet the magnetic screens are attached to decrease the spreading magnetic field. Between the floor of the experimental hall and the magnet a support must be foreseen.

Magnetic field of the magnet will be measured with the standard CERN NMR and Hall probes with a relative precision of $5 \cdot 10^{-4}$.

Chapter 7

Detectors

The experimental setup is schematically depicted in Figure 6.3. A scintillation hodoscope and a scintillating fibre detector are placed upstream of the spectrometer magnet. Two telescopes consisting of drift chambers, scintillation hodoscopes, gas Cherenkov counters and μ-identifiers are located downstream of the magnet. All detectors are described in detail below.

7.1 Scintillating fibre detector ($SciFi$)

To know the relative momentum of a pion pair one needs to measure the opening angle of a pair (besides the particle momenta). It may be obtained through the measurement of the particle coordinates with a scintillating fibre detector placed at 2 m from the target.

7.1.1 General description

The detector is designed on the technical basis recently achieved in fast readout of scintillating fibres ($SciFi$) by using position sensitive photomultipliers (PSPM) [AGOR91]. This technique provides a high spatial resolution as well as excellent time characteristics allowing to endow the device with two important functions: coordinate determination of the dimesoatomic pairs at high rate and trigger-incorporating "topological" criteria in real time.

Among several types of PSPMs the present design is based on the so–called "confined secondary electron" type PSPM having a minimum cross talk ($\sim$5%) between adjacent channels, such as H4140-20 (256 channels) or XP1724 (96 channels).

The mechanical structure is illustrated in Figure 7.1. Each plane, $\sim$10 cm wide, consists of 512 columns of 12 fibres 0.25 mm Ø(KURARAY CSCF38) aligned perpendicular to the incident particle direction. The effective thickness is therefore $\sim$3 mm (0.7% radiation length) so that the average number of photoelectrons per hit is $\geq$ 18. This guarantees a good detection efficiency close to 100% [AGOR93]. The scintillation light from each column of 12 fibres is sent to the photocathode of the PSPM through a bundle of clear fibres (0.25 mm Ø) or a Plexiglas ribbon, the extremity of which is fitted on the centre of the corresponding PSPM channel (Figure 7.2). A high precision in the lateral position of $SciFi$ columns, of the order of tens microns, can be achieved with the help of a mounting bench with triangular grooves to hold fibres in position during the construction of the $SciFi$ arrays.

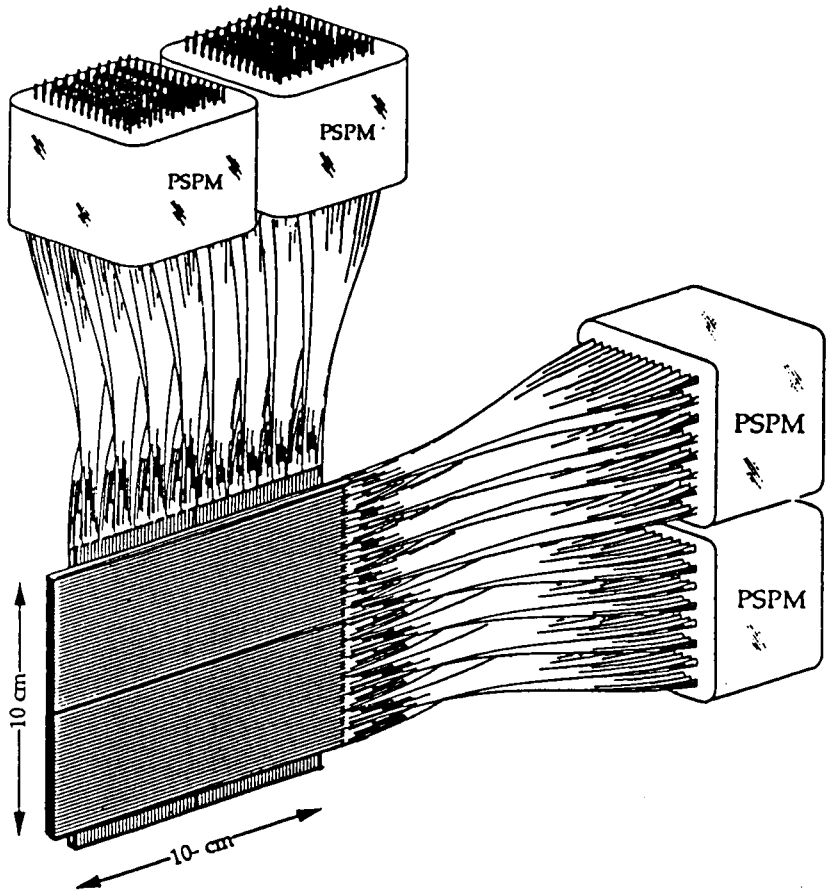

Figure 7.1: Mechanical structure of high-resolution $SciFi$ detector.

The signals from multianodes can be handled with standard electronics consisting of a series of leading-edge or preferably constant-fraction discriminators arranged in some logic scheme. However, taking into account the large number of channels needed, we foresee a custom-made circuit based on the so-called "ORIGINE" IC chips [DITT94] and further the ORIGINE-base electronics is considered. The circuit was initially designed for handling anode signals from cross-talk type PSPMs. A version of this circuit for our experiment is shown in Figure 7.3 and consists of "slope sensitive" adders followed by ECL comparators which detect the peak position of the amplitudes coming out of adjacent PSPM anodes. The typical performances of the chips are as follows:

Bandwidth:	DC to 250 MHz,
Transit time:	$\leq$3 ns,
Input dynamic range:	min. 30 – max. 160,
Output dynamic range:	$\sim$70,
Non-linearity:	$\leq$2%,
Power dissipation:	$\sim$55 mW/anode.

The first samples of ICs and the complete electronic system are presently under examination at LAPP.

Compared to the standard electronics, the ORIGINE circuit is particularly suited to this experiment for the following reasons. As seen in Figure 7.4, it delivers only one digital

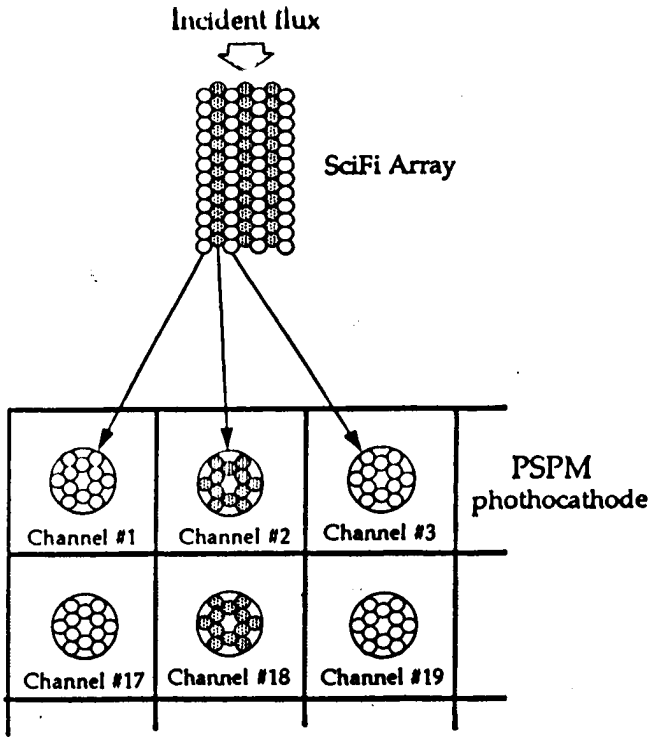

Figure 7.2: Mapping of $SciFi$ columns on the PSPM photocathode.

output per single track by "absorbing" nearby smaller pulses originated from optical, electronic cross talks or electronic noises. This behaviour greatly simplifies the selection of double-hit events in real time as described later.

7.1.2 Expected performances

Taking into account the geometric configuration of $SciFi$s, the statistical fluctuations of pulse heights according to the Landau distribution and also the peak sensitive nature of the ORIGINE circuits, we estimated the single- as well as the double-hit resolutions. The estimation has been done under the following simplified conditions:

1. "straight stacking" of 12 $SciFi$s along the incident particle direction, without taking in consideration the dead space due to the cladding,

2. neither optical nor electronic cross talk considered inside PSPM,

3. neglecting the cross talk between $SciFi$ columns due to delta rays.

The single-hit resolution can be estimated from the detection efficiency of a given channel as a function of the distance of an incident particle from the middle of the channel. The results are shown in Figure 7.5 for the incident angles $\Theta = 0$ and 25 mrad — the FWHM, $\sim$0.22 mm, is almost independent of Θ, but the $\sigma_{\text{r.m.s.}}$ increases from $\sim 60\,\mu$m at $\Theta = 0$ to $\sim 70\,\mu$m at $\Theta = 25$ mrad due to a higher probability of two adjacent excited columns.

In a similar way, the double-hit resolution was estimated by plotting the two-hit detection efficiency as a function of the separation of tracks. The results are shown in Figure 7.6.

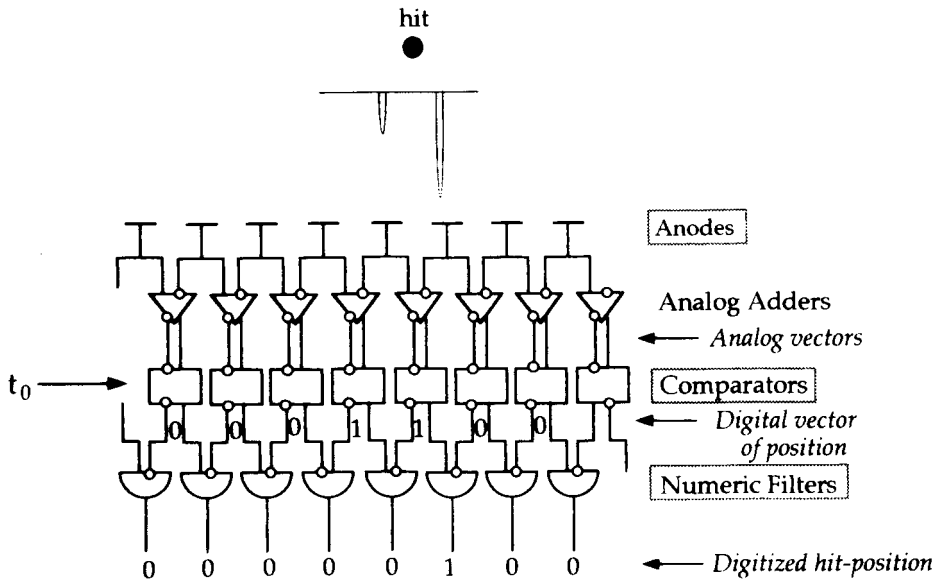

Figure 7.3: Front-end electronics based on the "ORIGINE" ICs.

As one can easily imagine, the efficiency rises from 0 as soon as two hits can excite 3 adjacent *SciFi* columns — as the probability of having a lower pulse height in the middle channel becomes non-zero due to statistical fluctuations. Then, the efficiency reaches 100% beyond a separation of the hits greater than the maximum width of two columns. Two-hit events are thus defined by two fired bins separated by, at least, one vacant bin. As long as the incident angle is smaller than (fibre diameter)/(column length) ~83 mrad, this definition of two-hit events is clear and rigorous — in the sense that the number of fired bins is equal to the number of tracks. The two-hit resolution thus obtained is $320 \pm 50\,\mu$m at $\Theta = 0$, and $320 \pm 80\,\mu$m at $\Theta = 25$ mrad.

The time characteristics of the detector are estimated from experimental data on the PSPM accumulated since several years. Such a type of photomultiplier, incorporating grid or mesh dynodes has, in general, excellent time characteristics thanks to the quasi-straight acceleration of electrons, and therefore the short transit time ($\leq$10 ns). It stands intrinsically up to a rate of ~20 MHz/channel without any significant deformation and overlap of pulses [KURO81]. In practice, we need, however, a summing up of a certain number of channels — for reasons of simplicity and cost-effectiveness — to provide a reference time t_0, which defines the decision time of hit channels by the numeric filters (Figure 7.3). Assuming for example a row of 16 channels coupled together for this purpose and the same rate capacity for each row (16/tube), the counting-rate capacity of the detector will be ~20 MHz×16 (rows)×2 (tubes) = 640 MHz. This is sufficiently large to deal with the expected incident flux ~ $2 \cdot 10^7\,\mathrm{s}^{-1}$. Concerning the time resolution we refer to a recent measurement on a *SciFi* hodoscope resulting in $\sigma_t \leq 0.7$ ns [AGOR94].

7.1.3 Topological information in real time

The front-end electronics based on the ORIGINE circuits delivers the digitized hit position(s) in ~3 ns ($+t_w$, time window for accepting accidental pairs) after arrival of the anode signals at the inputs. The pattern of the hits can then be handled in "real time"

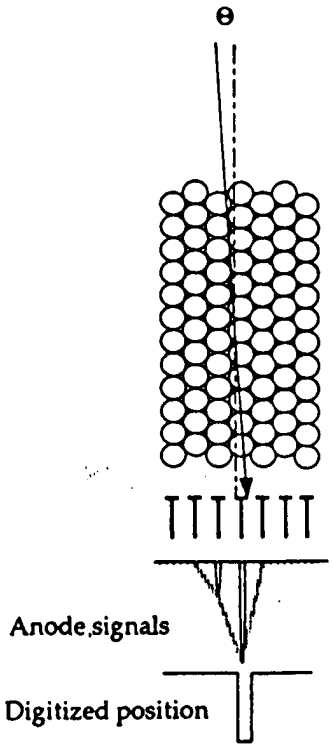

Figure 7.4: Peak-sensitive function of the ORIGINE circuits.

by a logic network which defines useful topological criteria for improving the "quality" of the trigger.

As described in Section 8.4 a suitable cut on the opening angle of $\pi^+\pi^-$-pairs allows to reject efficiently the background coming from free pairs, as the dimesonic pairs are confined in $\Theta \leq 3$ mrad, while the free pairs extend over $\Theta \leq 50$ mrad. Such a selection of events can be done by means of a special logic network. In Figure 7.7 there is shown one of possible realizations of this logic. It consists essentially of multifold linear FAN-INs summing up the digitized outputs of the ORIGINE circuits. In the first stage, 4 bins of the digital outputs are "linearly" mixed so that the precision on the upper limit of the distance d between π^+ and π^- is $\sim$1 mm — at 2 m from the target; this corresponds to $\Delta\Theta \sim 0.5$ mrad. Six "super"-bins thus defined are then coupled together in the second stage by shifting adjacent branches by a step of one super-bin, so that any pair with $d < 6$ mm can be detected by checking the pulse height of signal coming out of this stage, any pair of $d > 6$ mm failing to produce a superposed pulse higher than the standard pulse-height (800 mV). Also illustrated are some typical examples of events as well as their signal propagation in the network. Note that the time window for non-correlated π^+ and π^- pairs is defined by the adjustable width of the digital outputs from the last stage of the ORIGINE circuits.

The detection efficiency of two-hit events defined by such a logic system is shown in Figure 7.8. The inefficiency around $d = 0$ comes from the confusion of two-hits inside the two-hit resolution estimated in the preceding paragraph. As described in Section 8.4 a loss of good events due to this inefficiency — which is in fact the general problem of tracking

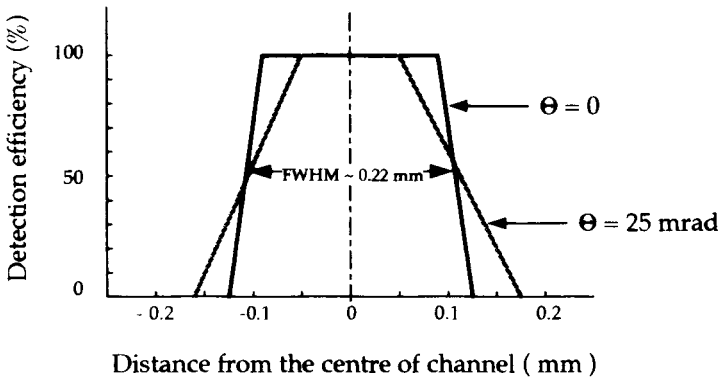

Figure 7.5: Detection efficiency for single-hit events.

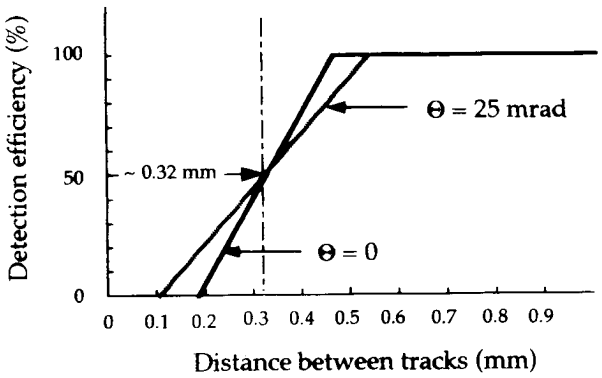

Figure 7.6: Detection efficiency for double-hit events.

detectors with finite resolution — can be mostly recovered (as discussed in Section 8.4) if the *SciFi* detector delivers also a tagging signal for single-hit events in real time. This is the second task (not reflected in Figure 7.7) for the logic network.

The whole logic network may be realized in a special fast processor based on commercially available ICs. It receives the signals from digital outputs of ORIGINE circuits and may produce two types of positive decisions for (1) close double-hit ($d < 6$ mm) or (2) single-hit events. The transit time of the processor is about 10 ns, an additional dead time is not involved.

Another approach is development of such network in ASIC. There is no need of any new technology for this aim. The transit time in this case would be the same but the electronics to be well much compact.

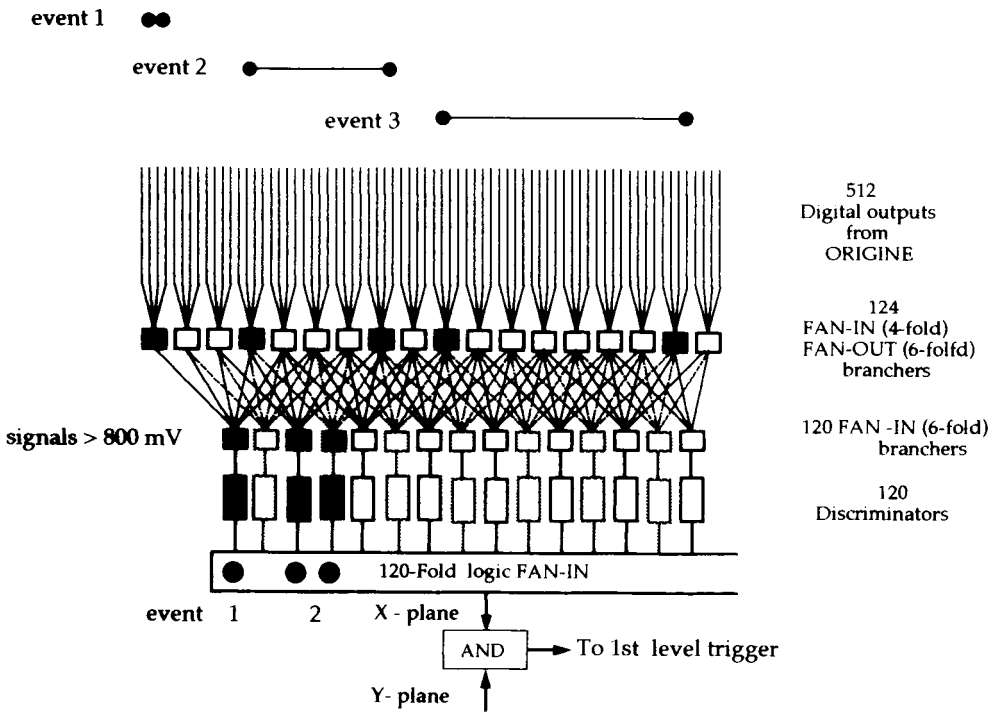

Figure 7.7: Logic network for rejecting the free pairs with large opening angles.

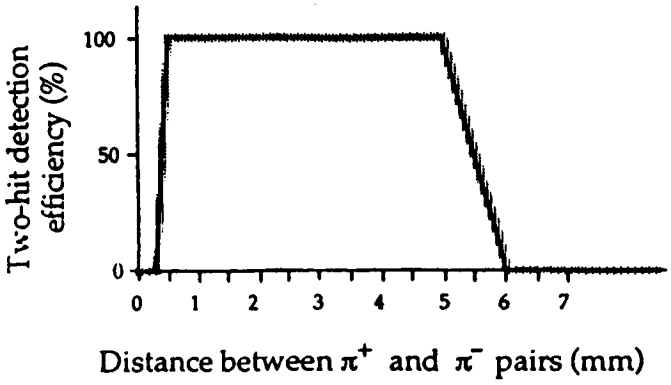

Figure 7.8: Detection efficiency for two-hit events defined by the logic network.

7.2 Forward scintillation hodoscope (FSH) for the double energy loss measurement

7.2.1 General description

The distinctive property of atomic pion pairs is the passing of two charged pions at rather small relative distance while they are detected before the magnet. This causes double energy release by ionization in a small sensitive volume of the detector comparing to the ionization loss by a single pion. It is essential that the double energy loss can be measured regardless of whether the tracks are resolved in space or not. Therefore, the uncertainties resulting from the inefficiency for detecting two tracks with relative distance approaching to zero, can be excluded.

In addition, good time properties of the FSH and its, though rather limited, space resolution make possible to use coordinate information from the hodoscope at the trigger stage.

The hodoscope will be placed at 2 m distance from the target at the position shown in Figure 6.3 as "the coordinate detectors". It consists of one layer set of polystyrene scintillator strips assembled together to overlap a sensitive area of size 10×10 cm^2 defined by the angular acceptance of the spectrometer. For this geometry the pions from the atomic pairs are distributed within the area of about 6 mm diameter. If the width of the scintillator strip is taken equal 6 mm then most of the atomic pairs will cross a single strip and the rest will cross a pair of neighbour strips. Therefore, the events of interest should be selected by the criterion of the double energy release in a single strip or in a pair of neighbour strips. All other pion pairs are widely spread over the total area of the hodoscope and so give rise to single ionization loss signals. We intend to use only a set of vertically arranged strips, selecting the pairs with a small relative distance in the horizontal projection. (Rejection of pairs with large distances in the vertical projection is provided by the scintillation hodoscope HH behind the magnet.)

The device realized in this way will perform the next main tasks:

1. To select the pion pairs with small distance in horizontal projection by double ionization cut. This information is used for producing the fast trigger signal (second level trigger, see Section 8.4).

2. To select the pion pairs with small relative longitudinal momenta using joint information on the direction of the total momentum of the pion pair and the coordinate information in the detectors after the magnet. This is achieved by the fast processor (third level trigger, Section 8.5) operating with the ordinal numbers of the FSH hit elements and of the coordinate detectors in both arms of the spectrometer.

Note that accidental pairs, detected within 20 ns resolution time of the fast trigger coincidence scheme, are subject to selection just in the same way as for real coinciding pairs. It is achieved owing to dedicated scheme of amplitude discrimination of signals.

The forward scintillation hodoscope will be used also to improve the pion identification by means of time of flight measurement at the distance between FSH and scintillation hodoscopes downstream of the magnet. FSH may be useful to suppress background arising from particle decays before the magnet, from interactions in the channel walls and from particles coming from outside of the channel.

7.2.2 Design of the *FSH*

The plastic strips, made of fast and efficient scintillator (NE104, NE111A, Pilot U) have dimensions: vertical length 10 cm, width 6.25 mm and thickness along the pions path 3 mm. They are assembled to form a plane of dimensions 10 $\times$ 10 cm^2 placed normal to the axis of the setup. The strips are separated each other by thin films and connected with the PM cathodes by polystyrene (or fibreglass) light guides of about 15 cm long. Light is guided through the top end of the strips so that PMs are most removed from the primary proton beam. Hamamatsu R647 PMs with 10 mm Ø photocathode and 15 mm Ø total width are arranged into space-saving two-layer set of 16 units with a total size (including the magnetic shield) of $14 \times 12 \times 5$ cm^3. The use of a separate photomultiplier tube for each element allows a fine and flexible tuning of the system and completely eliminates the problem of cross-talk between the channels.

The RMS angle of multiple scattering in the strip material is rather small: 0.91 mrad for $P_\pi = 1$ GeV/c and 0.30 mrad for $P_\pi = 3.0$ GeV/c. This is still smaller than a full opening angle of the atomic pairs (about 2.5 mrad) and does not deteriorate essentially the total angular resolution of the setup.

The electronic scheme of the device should provide:

1. Amplitude discrimination of the summed signals coming from pairs of neighbour channels. (It will be done for the charge produced by integrating the signal current during the 20 ns time interval. This provides the discrimination level independent on the time interval between the signals of two pions and therefore the same registration efficiency for all pion pairs — real or accidental.)

2. Shaping of signals in the channels where double energy loss occurred. (It should be done by constant fraction discriminators. These signals will be used to measure the hit times in the detector.)

3. Working out the double energy loss analog signals for the ADCs.

4. Formation of the ordinal numbers of the hit strips with "double energy loss" and of all strips where single particles were detected within the time interval determined by the "double energy loss" signal arrival.

The scheme with these functions should be developed as dedicated CAMAC unit.

7.2.3 Simulation of the device performance

Simulation of energy loss was done using the GEANT code under the next conditions: strip material — polystyrene scintillator; pion momentum range 1.8–3.0 GeV/c; normal hit of pions at the strip surface. Fluctuation of the ionization losses and energy loss of the secondary particles were taken into account. Thickness D_l of the strips was taken equal to 0.5, 1.0, 3.0 and 6.0 mm.

The energy loss distribution $\varphi_1(\Delta E)$ for one pion and $\varphi_2(\Delta E)$ for two pions traversing the strip are shown in Figure 7.9a (for the $D_l = 3$ mm case). Conversion of the energy loss ΔE into photoelectron emission in the photomultiplier tube was calculated at usual assumptions (e.g. [REVI94]). The light attenuation in the 10 cm long scintillator and 15 cm light guide was neglected. The number of photoelectrons n corresponding to the calculated average number $\bar{n}$ was considered as governed by the Poisson distribution. The

light collection nonhomogeneity along the strip length was neglected owing to a possibility to minimize it by the appropriate small variation of the strip thickness D_l along its length.

The resulting distributions $f_1(n)$, $f_2(n)$ of the photoelectron number are shown in Figure 7.9b. The relevant integral distributions are given in Figure 7.9c. One can choose from them the optimum value of the threshold that ensures a high efficiency of double pion detection at rather low single pion admixture.

Dependence of the efficiency ε_1 (at $\varepsilon_2 = 95\%$) on the strip thickness D_l is presented in Figure 7.10. It is seen that the strips of 1.5–3.0 mm width guarantee rejection of the single pion events at a level of about 10%. Then the probability to produce the double ionization signal by at least one of pions from the pair crossing two strips, that are not neighbour, is 20% and hence the rejection factor for such pion pairs is about $R = 1/2\varepsilon_1 \simeq 5$. The rejection factors of the device operating in the full trigger system, including the selection by relative longitudinal momenta of the pairs, are presented below in the Chapter 11.

The rejection efficiency of the FSH can be improved, as known for a long time [AKIM60], by using the multiple amplitude discrimination (in scintillators placed in series). It can be done in the FSH with two or three layers of scintillator while conserving its total thickness.

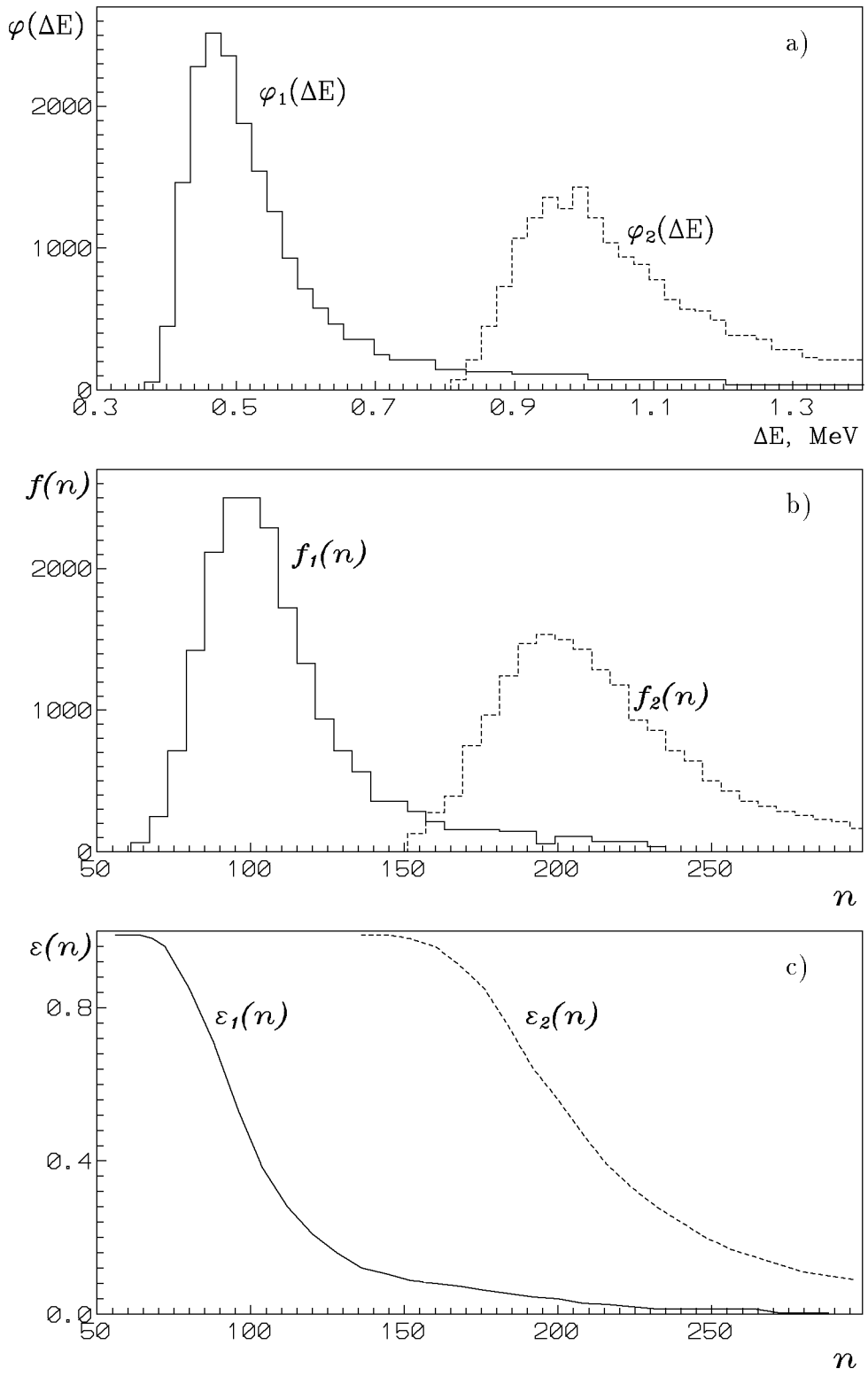

Figure 7.9: Computer simulation of the energy loss separation for the single pion and pion pair events at $D_l = 3$ mm: a) energy loss distributions; b) distributions over the PM photoelectron number n; c) integral distributions of photoelectron number.

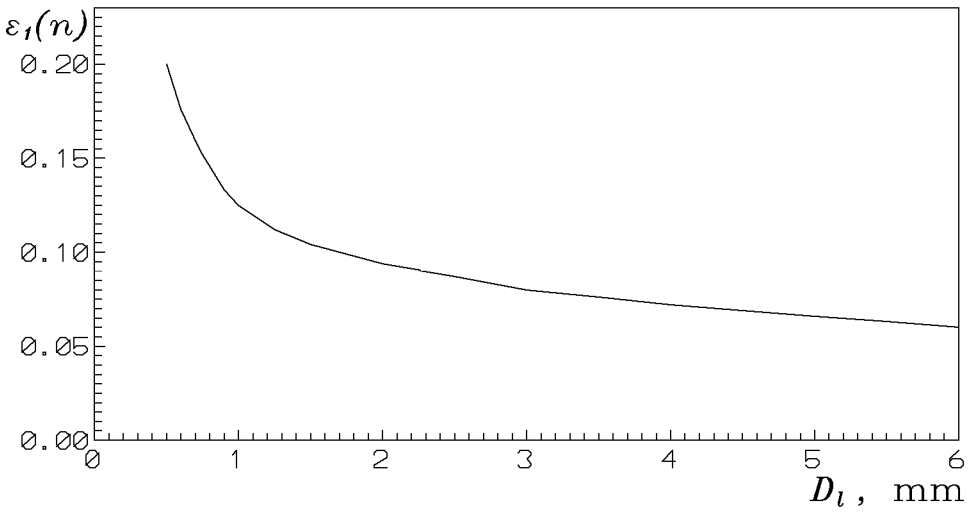

Figure 7.10: Calculated dependence of the single pion detection efficiency on the strip thickness at threshold set for 95% efficiency of the pion pair detection.

7.3 Drift chambers (DC)

7.3.1 General

The drift chamber system ($DC1-DC4$) is used to provide charge particle tracking through the spectrometer (see Figure 6.3).

The drift chambers contain the following sets of coordinate planes:

$$\begin{aligned} DC1 &- X,\ Y,\ W,\ X,\ Y,\ W; \\ DC2 &- X,\ Y; \\ DC3 &- X,\ Y; \\ DC4 &- X,\ Y,\ X,\ Y\ . \end{aligned}$$

As the accuracy of track reconstruction at a certain coordinate accuracy of the chambers is determined, in general, by the distance between the extreme measured points on the track, the $DC1$ and $DC4$ chambers have two coordinate planes in each projection.

The W-planes with inclined anode wires in $DC1$ are provided for rejecting false combinations of X and Y coordinates during track reconstruction at passing of a few particles through the chambers. The angle between the wires in the W - and X - planes is 11.3°.

7.3.2 Chamber electrodes

A schematic drawing of chamber cells is shown in Figure 7.11. The cathodes are made of carbon-coated Mylar foil of 20μm thick. Surface resistivity of the coating equals about 400 Ohm per cm^2. The gap between the cathode electrodes equals 10 mm.

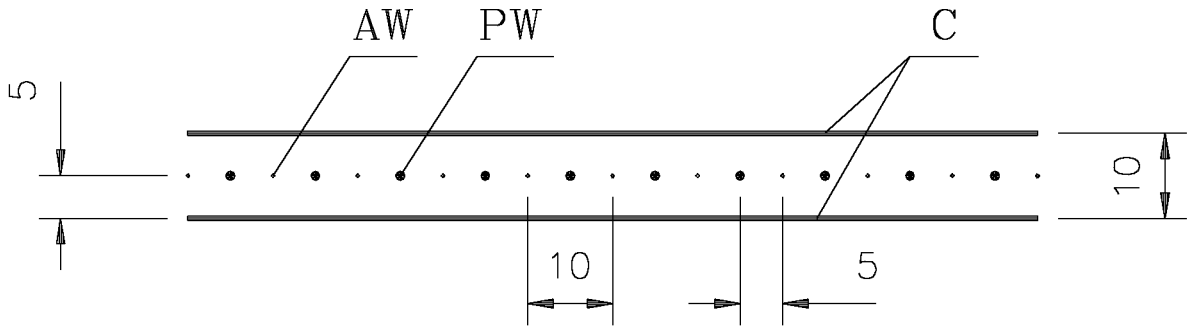

Figure 7.11: Schematic view of wire chamber electrodes.

The signal plane placed in the middle of the gap consists of an alternating set of anode and potential wires. The wire material is copper-beryllium. The diameter of an anode wire is 50μm and that of a potential wire is 100μm. The distance between the anode and potential wires equals 5 mm.

So an elementary drift chamber cell has a "square" (10 $\times$ 10 mm^2) shape with an anode wire placed in its center. As was shown in [DAVY86], this geometry is optimum to provide minimum size of the region of drift characteristic nonlinearity near the potential wire.

7.3.3 Chamber construction

A sketch of the $DC2$ chamber and its cross section are shown in Figure 7.12. The chamber has a sensitive area 80×40 cm^2 and consists of two coordinate planes: an X-plane with wires directed along the short chamber side and an Y-plane with wires directed along the long chamber side.

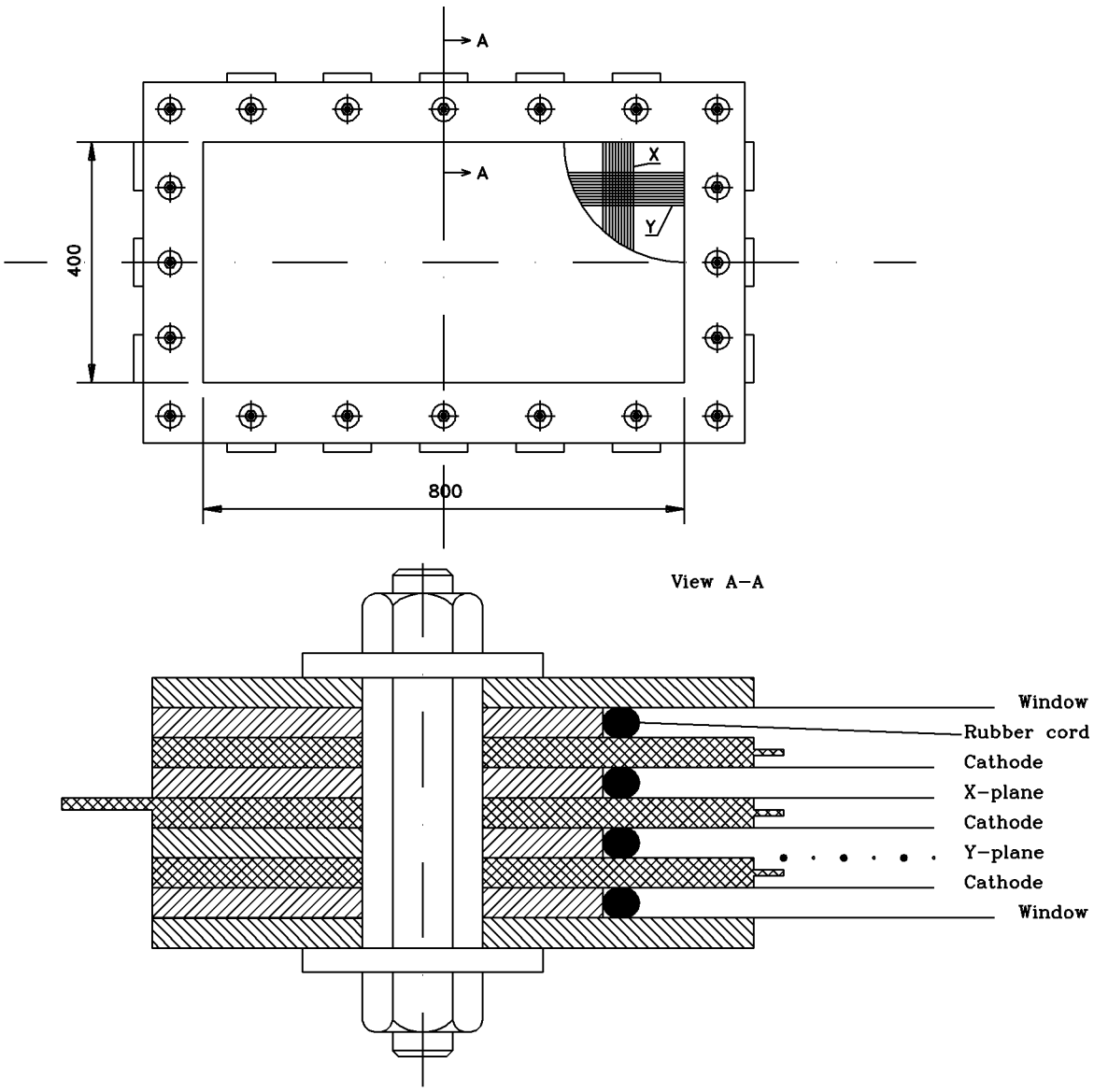

Figure 7.12: Construction of $DC2$ chamber.

As seen in this figure, the chamber is a stack of frames. The frame thickness is 5 mm. One group of frames is made of fibreglass strips glued together. One side of the frame has printed electrodes to solder the anode and potential wires, and the opposite side has a printed electrode to fix the cathode foil by conductive glue.

There are aluminium frames placed between the fibreglass frames. The aluminium frames fix the gap between a signal plane on one fibreglass frame and a cathode plane on another. The rubber cord glued along the inner edge of the aluminium frame is for

gas isolation of the chamber. The Mylar windows of 50 μm thick are fixed on the outer aluminium frames.

The construction of the $DC3$ and $DC4$ chambers is similar to $DC2$. The $DC3$ chamber, like $DC2$, has one X- and one Y- coordinate planes. Its sensitive area is 112×40 cm^2. The $DC4$ chamber has two X- and two Y-coordinate planes. The wires in the planes of the same name have 5 mm shift to one another to simplify deciding of the left-right ambiguity pecular to drift chambers. The size of the $DC4$ sensitive area is 128×40 cm^2.

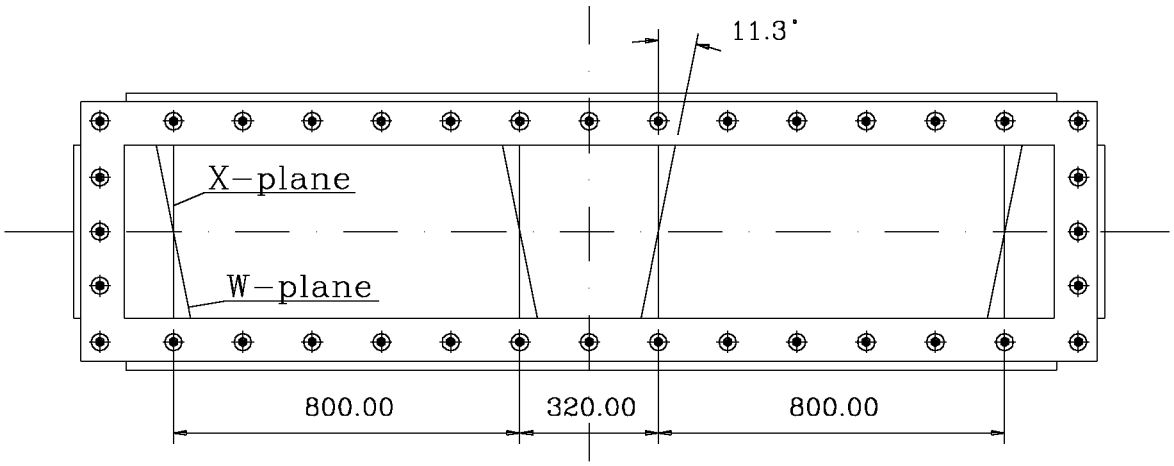

Figure 7.13: Construction of $DC1$ chamber.

The $DC1$ construction differs from the one shown in Figure 7.12. It especially relates to the chamber electrodes, which is illustrated by Figure 7.13. As can be seen in this figure, the electrodes are separated into two independent 80×40 cm^2 groups, placed symmetrically to the axis going through the center of frames. The zone 32 cm in width between these groups is insensitive to particle passage. Both the left and the right parts of the chamber have two X- , two Y- and two W- coordinate planes. The wires in the planes of the same name have 5 mm shift to one another like in the $DC4$ chamber.

7.3.4 Readout electronics

An electronic channel consists of an amplifier-discriminator and time-to-digital converter (TDC). The 16-channel amplifier boards are mounted on the chamber planes and TDCs are placed close to the drift chambers. Minimal threshold of the amplifier is 1 μA. The TDC boards will be based on 4-channel ultra-fast memory chip. The bin width is 5 ns which corresponds to 250 μm at the drift velocity 50 mm/μs.

Full description of readout electronics is given in Section 8.7.1.

7.3.5 Summary

General parameters of the drift chamber system:

- number of chamber blocks – 7;
- number of signal planes – 28;

- number of electronic channels ≈ 2000;
- maximum drift time $\approx 100ns$;
- thickness of chamber block $\approx 1 \cdot 10^{-2} L_{\rm rad}$;
- coordinate resolution – $\sigma \leq 200\mu$m.

7.4 Scintillation hodoscopes (HH, HV)

In order to perform the fast coincidence between two spectrometer arms for the first level trigger, as well as the selection of two particles for the higher level trigger, a couple of scintillation hodoscopes HH and VH will be installed in each arm. The sensitive area extends over 1300 mm(H) $\times$ 400(V) mm^2.

One of the planes HH consists of 16 horizontally aligned scintillator slabs 1300 mm long 25 $\times$ 25 mm^2 in cross-section. High time resolution of this hodoscope is crucial, as a large bulk of detected events comes from accidental coincidence between the two arms. In addition, backgrounds such as π^-p, π^+K^- or π^-K^+ will also be partly suppressed by the precise timing constraint. Each scintillator is viewed by two photomultipliers from both ends and the signals are sent to a mean-timer so as to compensate the time fluctuation coming from different hit positions in the slab length. From previous experiment [AFAN93B] where two hodoscopes each of 8 slabs 1.4 m long were used, a time resolution of $\sim$200 ps can be expected in this way for the currently proposed experiment. The choice of the photomultiplier type is oriented towards fast and compact (small diameter) tube such as Philips XP1911(Ø 19.2 mm), Hamamatsu R1450(Ø 18.6 mm) or the Russian tube FEU-175(Ø 22 mm).

Due to low relative momentum of π^+ and π^-, in c.m.s., coming from the dimesoatom break-up and to the fact that the magnetic field does not deflect particles in the vertical direction, the pions in both arms have almost equal vertical coordinates. So only elements with equal or adjacent numbers in HH_1 and HH_2 will be hit. The selection of such events will be done at the first level trigger (see section 8.3). Taking into account the relative momentum of π^+ and π^- and the multiple scattering, the optimum width of the element is estimated to be 20–25 mm and the value 25 mm has been chosen.

The probability of two hits within the same scintillator element, that leads to a wrong measurement of time, is nearly 3% under the realistic beam conditions (see chapter 11).

Another plane VH is dedicated to realize the selection (in couple with FSH) of low Q_L and Q_X events at the third level trigger and to help in sorting out and analysing of multi-track events. It consists of 24 scintillator slabs, 56 mm wide, 400 mm high and 25 mm thick, all aligned in the vertical direction. Each slab is viewed by two photomultipliers of 2 inch diameter, such as XP2020, R1828 or FEU-143.

For all hodoscope elements the time and amplitude information will be recorded through TDCs and ADCs, and used in off-line analysis. Materials needed are listed in Table 7.1.

Table 7.1: Summary data on hodoscopes

	HH	VH
Scintillators	32 $1300 \times 25 \times 25\,\mathrm{mm}^2$	48 $400 \times 56 \times 25\,\mathrm{mm}^2$
Photomultipliers	64	96
Mean-timers	32	48
TDC channels	32	48
ADC channels	64	96

7.5 Cherenkov counters

Threshold gas Cherenkov counters are used for suppression of triggers from electrons at statistics runs and for calibrations with electrons (see chapter 13). The efficiency of counters must be more 99% for electrons and as low as possible for other particles.

The area of the entrance window is $1400 \times 420\,\mathrm{mm}^2$ (width $\times$ height). The angular aperture is $\pm 11°$ in horizontal plane, the mean incident angle depending on horizontal coordinate. The angular divergency in the vertical plane is much lower ($\pm 1.5°$) and is defined by the distance from the target and the vertical size of the window.

The counter has 3 m long air radiator at atmospheric pressure. The Cherenkov light is reflected by parabolic (or maybe spherical) mirrors onto a set of photomultipliers provided with light collection cones. The area of the exit window which has to be covered by mirrors is $2.8 \times 0.75\,\mathrm{m}^2$. The number of photomultipliers, the shape, number and dimensions of the mirrors will be obtained after detailed calculations of the light collection system. Now it seems reasonable to use about 6 photomultipliers per one counter.

The light collection from a large surface at rather large angular spread is the main difficulty in developing these counters. But likewise problems have been successfully resolved in other experiments. In particular, in Protvino experiment [AFAN93A] the freon-12 filled 1.5 m long Cherenkov counters [GORC84] were used to detect electrons spread over $1.0 \times 0.5\,\mathrm{m}^2$ entrance surface in $\pm 10°$ angular range. The light was collected onto 2 photomultipliers FEU-49 by 2 parabolic-like mirrors, each of $0.75 \times 0.6\,\mathrm{m}^2$. The mirrors were produced in the laboratory workshop from epoxy resin and then were coated by evaporated Al. The counter signal corresponded to 5 photoelectrons per incident electron.

In the present case we are going to use high quantum efficiency quartz window photomultipliers of a large diameter (like XP2041Q or R1250). The mirrors could be done with higher quality, too. Then assuming a light collection efficiency equal to 0.5 and integrating the photocathode sensitivity [PHIL89] over the Cherenkov photon spectrum one can calculate the number of photoelectrons being 19 for XP2041Q or 12 for usual glass window XP2041 at 3 m long air radiator.

Other gases have been considered also as possible radiators. Freon-12 produces 3.7 times more Cherenkov photons than an air radiator does. So the counter length could be less. But the threshold of Cherenkov radiation in freon-12 is 3.0 GeV/c for pions and 2.2 GeV/c for muons, so these particles may be detected in the high momentum region of the spectrometer range (up to 4.5 GeV/c) that would lead to loss of events. Besides, the

gain in decreasing of dimensions is not proportional to the growth of the Cherenkov photon output: the length of the counter may be 2-2.5 times less, but the lateral dimensions will be shortened by 30% only. One has also to make a hermetic radiator volume and take care of a gas filling system that should prevent freon from blowing out into the atmosphere. In addition the larger Cherenkov cone makes light collection some more complicated. Taking into account all positive and negative factors we prefer to use air as a radiator.

Another option is to use CO_2. With this radiator the Cherenkov photon output is 40% larger than with air. The only disadvantage in this case is the necessity of hermeticity of the gas volume. A gas filling system is also needed but very simple.

The Cherenkov counters are the main detectors to identify electrons in this setup. But if their efficiency is not sufficient to obtain as large rejection factor of electrons as needed, each telescope will be supplemented with a simple shower detector consisting of a Pb sheet of several radiation lengths followed by a plane of scintillation counters. This shower detector could be placed between the Cherenkov counter and the iron absorber.

7.6 Muon detectors

An array of scintillation counters will be placed behind each iron absorber to identify muons. The absorber has a variable thickness from 0.6 to 1.2 m corresponding to the lower and upper limits of the momentum range.

Taking into account the divergence of particle trajectories and the scattering of muons, the size of the detector is 3.6×0.75 m^2. The full area may consist of, for example, 8 scintillator slabs of 45×75 cm^2, each viewed by two photomultipliers at both ends through Plexiglas light guides with the "adiabatic" light-transmission.

7.7 Monitor counters

To monitor the secondary beam intensity a small scintillation counter telescope combined with Pb converter will be installed on the spectrometer axis downstream of the muon detector. The counter detects photons coming from the target. This photon counter is preferable to charged particle monitors as the counting rate is proportional to the number of interactions only, and does not depend on magnetic field environment.

The counts are integrated during the time between trigger signals, and recorded event by event together with the main content of each event. This information will be used off-line to count the total number of interactions as well as to exclude the events recorded under abnormal beam conditions.

7.8 Microstrip gas chamber ($MSGC$)

In addition to the scintillating fibre detector ($SciFi$ described in Section 7.1) we intend to use a microstrip gas chamber ($MSGC$). This 10×10 cm^2 device can be placed at a distance between 10 to 20 cm downstream of the $SciFi$.

The main purpose of this detector is to provide a direct measurement of the slope of incoming charged tracks before they enter the magnet, independent of the knowledge of the beam position. In addition the MSGC will provide:

- some redundancy in the first lever arm of the spectrometer;
- improvement in the alignment procedures of the general detector;
- linear pattern recognition algorithms;
- improved momentum resolution of charged particles.

The technical characteristics of the MSGC are presented below in Appendix E together with its general description and expected performances.

To get a good estimate of the error obtained in the measurement of the momentum, we have to know the variance-covariance matrix due to both multiple scattering and hit measurements and evaluate its elements inside the magnetic field region. Without entering in technical details of the resolution of the corresponding set of linearized equations, one can say that introducing the MSGC detector leads to roughly divided by a factor of 1.5 the sigma of the angular deviation of any trajectory in the magnet. This factor has been computed for a 20 cm separation between the two detectors ($SciFi$ and $MSGC$).

We therefore are confident that using such a $MSGC$ located at a few tenth of a meter downstream of the $SciFi$ will ensure a noticeable gain in precision without perturbing the quality of our general setup and that such a gain can be obtained for a reasonable investment. In particular, we have to emphazise that this type of detector is the most transparent we may imagine to use in addition to the main devices already discussed in this proposal.

Chapter 8

Trigger scheme and data acquisition system

8.1 General description of trigger

To suppress the high rate of background events a multilevel trigger is used (Figure 8.1).

The first level trigger signal is formed by coincidences of the two arms of the magnetic spectrometer:

$$(VH \cdot HH \cdot \overline{C} \cdot \overline{S_\mu})_1 \cdot (VH \cdot HH \cdot \overline{C} \cdot \overline{S_\mu})_2 \tag{8.1}$$

Here VH and HH denote the scintillation hodoscopes with vertically and horizontally oriented slabs, C is the threshold Cherenkov counter for rejection of electrons, S_μ is the scintillation counters behind the iron absorber for rejection of muons (muon counters). The resolution time of coincidences is chosen to be 20 ns because it is necessary to ensure accumulation of enough accidental pion pairs which are used to simulate the free pion pair distribution.

The elements of HH_1 and HH_2 are included into the first level trigger in a special way that takes into account specific features of the dimesoatom breakup to suppress background. As the opening angle of pions from atomic pairs is very small and is hardly affected in the vertical plane by passing through the magnet, the two pion tracks are equally inclined with respect to the median magnetic field plane. This leads to close vertical coordinates of tracks in the hodoscopes. The logic of the first level trigger is arranged in such a way that a coincidence occurs only for those events in which the difference of hit slabs in HH_1 and HH_2 is ≤ 1. For the chosen width of slabs this condition does not cause losses of atomic pairs.

At the second stage the information from detectors placed upstream of the magnet is added. This includes a topological criterion, based on the opening angle, from the scintillating fibre detector $SciFi$ as well as a double ionization loss criterion from the forward scintillation hodoscope FSH. The topological criterion selects events characterized by low relative momentum in a particle pair. The ionization criterion demands double ionization within a single or two adjacent strips of the detector. Both devices produce their decision in real time.

Two hardware processors that handle the data from detectors downstream of the magnet (and from FSH in one case) provide further suppression of background at the third level of the trigger. They exploit the same feature of smallness of relative momentum

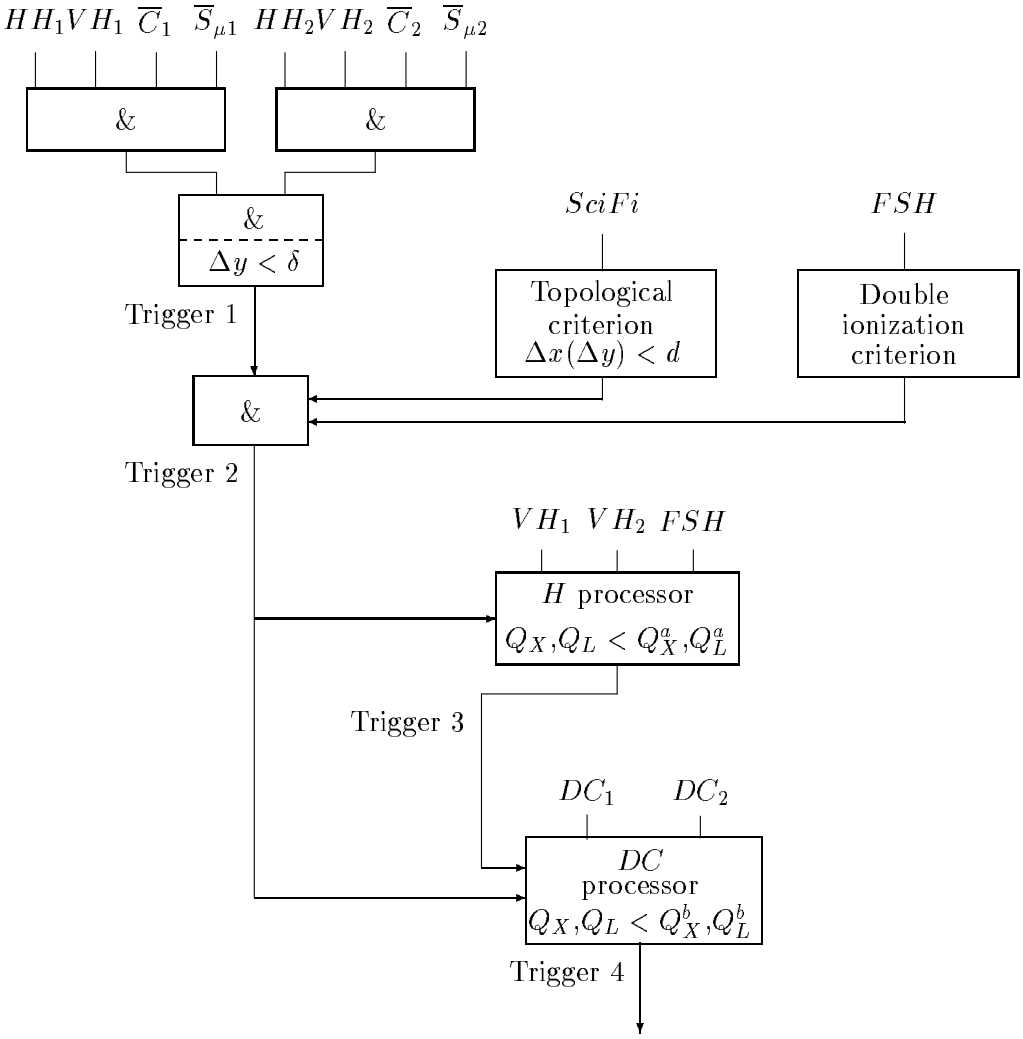

Figure 8.1: Scheme of trigger.

for useful events through the test of kinematical limitations inherent in the process under study. Due to the separation of positive and negative particles after the magnet and to a lower track multiplicity in the restricted momentum acceptance region compared with the upstream detectors, these processors produce additional rejection of background events.

The first processor (hodoscope processor HP) receives the signals from hodoscopes VH_1, VH_2 and FSH. As the positive and negative pions from atomic pairs have almost equal laboratory momenta, the numbers of hit elements in VH_1 and VH_2 are correlated. The table of permitted combinations changes with the X-coordinate of a pair as measured by the FSH. The HP checks if the combination of hits is allowed and so performs a fast preliminary selection of events by Q_L and Q_X values. The positive decision of this processor produces the third level trigger signal.

The second processor (drift chamber processor DCP) handles the numbers of hit DC wires in order to reconstruct tracks in the X-plane. It selects more precisely the pion pairs by the values of the Q_X and Q_L components of the relative particle momentum. The positive decision of the DCP defines the final, fourth level trigger.

A more detailed description of all trigger stages is given below in this chapter. The background rejection performance of the processors depends on the beam intensity and is given in Chapter 11.

8.2 Front-end electronics for scintillation and Cherenkov detectors

The same electronics will be used for scintillation hodoscopes both with vertically and horizontally oriented slabs and for muon counters.

Signals of photomultipliers looking at opposite sides of slabs go to a module containing constant fraction discriminators (CFD) and mean timers (MT). About 20 CFDs and 10 MTs will be placed in one CAMAC module of double width. CAMAC crates with these modules will be placed near the detectors. Thresholds and zero detector levels of CFDs may be changed remotely and recorded.

Outputs of these modules are connected to the inputs of the fast trigger and to time-to-digital converters (TDC) after suitable delays.

The signals of all PMs of each Cherenkov counter are linearly summed in a CAMAC module and arrive at discriminators producing the signals of Cherenkov counters as a whole. Discriminators may be of constant fraction or leading edge type.

8.3 First level trigger (fast trigger)

To form a fast trigger we intend to use units that allow different kinds of trigger in one spill. For example, besides pion triggers the electron-positron pairs may be stored for calibration.

Signals of detectors of each spectrometer arm come to programmable modules which form the telescope signals $T1$ and $T2$. To detect different particles the signals of detectors may be combined in different ways:

$$T(\pi) = VH \cdot HH \cdot \overline{C} \cdot \overline{S_\mu} \tag{8.2}$$

$$T(e) = VH \cdot HH \cdot C \cdot \overline{S_\mu} \tag{8.3}$$

$$T(\mu) = VH \cdot HH \cdot \overline{C} \cdot S_\mu. \tag{8.4}$$

Some control signals may also be included in the process of fast trigger forming for some tuning measurements. Combining the telescope signals one obtains the resulting fast trigger signals.

The universal logic modules LeCroy CAMAC Model 2366 may be used for fast trigger. In the first level trigger the selection of events that have a difference ≤ 1 between the numbers of hit slabs in HH_1 and HH_2 will be also realized with these modules. For this purpose a signal from any HH_1 element with the number n is checked to coincide with the "OR" signal of the HH_2 elements with the numbers $n-1$, n and $n+1$. All coincidence circuits (16 units, equal to the number of slabs in HH_1) are "OR"'ed and the resulting signal gets to coincidences with other detectors.

In order to prevent fast trigger generation during data processing dead time the logic modules have an "Inhibit" input.

8.4 Second level trigger (upstream detectors)

Trigger 2 signal is worked out if Trigger 1 is accompanied by a positive decision of $SciFi$ and FSH logic.

As described in Section 7.1, the logic network of $SciFi$ is able to provide in real time the tagging signal for those events where two or more hits are detected with at least one pair with a distance between fired fibres smaller than some preset value. For pion pairs from dimesoatom breakup the maximum distance between particles at the $SciFi$ position is 6 mm. Imposing this criterion (type 1 positive decision) in both coordinate planes could lead to a large background rejection. But this simple cut alone cannot be applied as a noticeable part of dimesoatoms would be lost due to the finite two-hit resolution of $SciFi$. As a result, two unresolved hits are detected as a single-particle hit. The losses are about 10% for breakup from 1S state and even more and, that is essential, unknown for higher states. So we need to eliminate or to measure accurately these losses.

To keep a major part of unresolved pairs the logic network of $SciFi$ will also produce a tagging signal if only one hit is detected in the whole plane (type 2 positive decision). In this case only those unresolved dimesoatom pairs are lost that are accompanied by a third, accidental or not, particle that is at a distance larger than 6 mm. The lost fraction, about 30% of unresolved pairs, can be determined precisely during off-line data analysis by comparison of the numbers of two- and three-particle events detected by a type 1 positive decision as just the same relation is valid for type 2 events. To make this feasible, the record of any event must contain the indication of the decision type.

Note that type 2 decision arises both for unresolved pairs and for any single-particle hit in $SciFi$. The high rate of single-particle signals somehow decreases firstly after the double ionization cut imposed in FSH. Finally those type 2 events, that are initiated by single particles, are eliminated after coincidences with the two telescope branches requiring at least two particles to be found downstream of the magnet. The rest events of type 2 are unresolved pairs which are processed further together with type 1 events. All selected in this manner pairs have a distance less 6 mm between particles. So the addition of the single hit detection does not decrease rejection power of $SciFi$ for Trigger 1 events, but let one to utilize the most of unresolved pairs.

The trigger logic of $SciFi$ is seen in Figure 8.2 where the whole logic of Trigger 2 is shown.

The electronics of the scintillation hodoscope FSH placed near $SciFi$ gives a trigger if the amplitude in one or two adjacent strips exceeds the threshold set for double ionization detection. The amplitude is integrated in the resolution time of coincidences (20 ns) to ensure adequate conditions for detection of real and accidental pairs.

The coincidence of $SciFi$ and FSH positive decisions with Trigger 1 produces the Trigger 2 signal.

8.5 Third level trigger (HP processor)

The processor HP analyzes the numbers of the hit elements in hodoscopes VH_1, VH_2 and FSH. It has a fast memory containing a set of look-up tables, one for each of the 16 scintillators in the FSH. Each table contains all allowed combinations of hit elements in VH_1 and VH_2 for a given FSH channel. The processor looks into the corresponding table and checks if the detected combination is an allowed one. The decision time of the HP will be about 100 ns.

If the HP produces its positive decision then a further processing of data is performed. Otherwise, a "RESET" signal is generated.

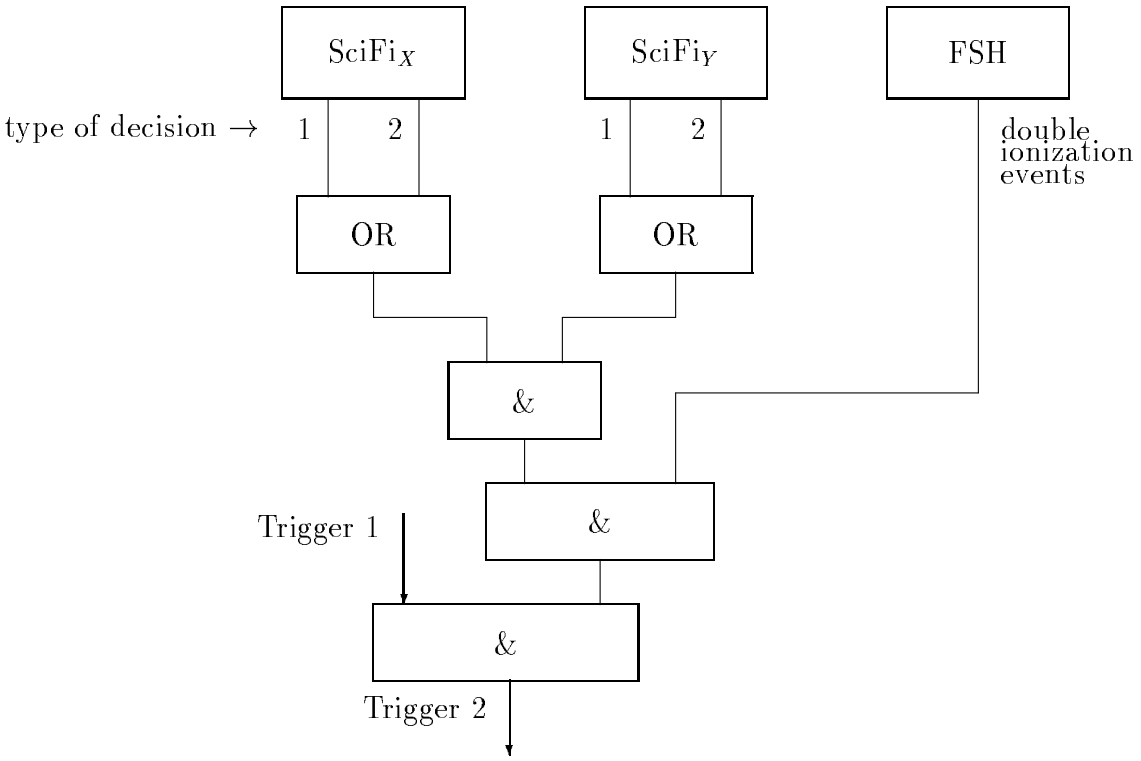

Figure 8.2: Logic of Trigger 2.

8.6 Forth level trigger (DC processor)

A special hardware processor (DCP) selects events that satisfy the following criteria for the components of the relative momentum Q in the center of mass system:

$$|Q_L| < 30 \text{ MeV}/c \quad (8.5)$$

$$|Q_x| < 3 \text{ MeV}/c \quad (8.6)$$

All pion pairs coming from dimesoatom ionization are within these ranges of Q_L and Q_X. In the lab system these conditions correspond to limitations on the difference between the two pion momenta (8.5) and on the X-coordinate difference before the magnet (8.6).

8.6.1 Selection of the algorithm. Simulations.

Each spectrometer arm contains 6 X-planes of drift chambers combined into 4 stacks (see section 7.3). The tangent of the angle θ_x between the track projection on the XZ-plane and the Z-axis of the setup as well as the X-coordinate of a track in the first plane of the drift chambers are the initial values for calculation of the momentum and of the emission angle of a particle from the target.

To find track parameters we define a straight line by the hit wires in planes 1 and 6, considering it as the track of a particle (edge track points algorithm).

Table 8.1 shows the values of RMS (σ) and maximum errors (S) in measuring the X-coordinate in the first plane and the tangent of θ_x for track edge points and χ^2 algorithms:

Table 8.1: Precision of track reconstruction

	σ_x	S_x	$\sigma_{\tan\theta_x}$	$S_{\tan\theta_x}$
χ^2	1.86	5.5	$2.4 \cdot 10^{-3}$	$9 \cdot 10^{-3}$
Track edge points	2.88	5.0	$3.4 \cdot 10^{-3}$	$10 \cdot 10^{-3}$

The losses of useful events in the on-line phase of the analysis should be minimal, so we must apply our criteria under the assumption of maximal errors. Table 8.1 shows that the χ^2 algorithm (which is obviously more complicated to implement in hardware) does not give a significantly better performance.

A simulation has been performed in order to estimate the efficiency of the track edge points algorithm. We generated 20,000 events with one track in each spectrometer arm. Pair of numbers N_1 and N_6(numbers of hit wires in the first and the 6-th planes of the drift chambers) formed an address which was used to extract the track parameters from the look-up table. Each table entry contained the limits p_{min} and p_{max} for momentum and the limits $\sin\alpha_{min}$ and $\sin\alpha_{max}$ for the sine of the angle between the Z-axis of the setup and the track projection on the XZ-plane before the magnet. Events were rejected if any of the following conditions was not fulfilled:

$$\begin{aligned} p_{max_1} - p_{min_2} &> 0 \\ p_{max_2} - p_{min_1} &> 0 \end{aligned} \tag{8.7}$$

$$\begin{aligned} \sin\alpha_{max_1} - \sin\alpha_{min_2} &> 0 \\ \sin\alpha_{max_2} - \sin\alpha_{min_1} &> 0 \end{aligned} \tag{8.8}$$

Here subscripts 1 and 2 correspond to the parameters of the tracks found in the first and the second spectrometer arms. The values of the limits for track parameters in the table have been calculated in such a way that the result of applying criteria (8.7) and (8.8) was equivalent to (8.5) and (8.6).

No useful events have been lost during the test of the algorithm with simulated events.

8.6.2 Possible hardware implementation of the DC-processor

The work of the DC-processor can be divided into two stages. In the first one, two identical devices (track finders) find tracks in each spectrometer arm. In the second stage, conditions (8.7) and (8.8) are checked for all pairs of tracks which have been found.

In the first stage, taking into account the efficiency of the drift chambers, we accept tracks if hit wires are present in at least four DC planes and if in the first as well as in the last stack of planes there is at least one hit wire. So we must then consider the following combinations of the base planes: 1 and 5; 1 and 6; 2 and 5; 2 and 6.

For each combination all possible pairs of hit wires are used as addresses in the table that contains digital windows for wire numbers which can be hit in intermediate planes. We accept a track if at least two intermediate planes contain hit wires in these windows.

With such an approach, in the case of a particle hitting wires in all 6 planes we shall find four tracks; 3 of them are subsets of the track found for the 1-st and 6-th DC planes. We ascribe an identifier to each track that describes track contents. The comparison of identifiers of tracks, traced through different numbers of planes allows rejection of such subsets.

The estimated amount of memory for a hardware implementation of such a track finder is 300-350 KBytes for each spectrometer arm.

In the second stage (if at least one track was found in each spectrometer arm), we apply criteria (8.7) and (8.8) for all pairs of tracks in the two arms. A positive decision (the forth level trigger signal) is generated if the processor finds a pair satisfying the given criteria.

There are two possible ways of developing a hardware processor for the second stage. The first one assumes the extraction of values p_{min}, p_{max}, $\sin\alpha_{min}$ and $\sin\alpha_{max}$ corresponding to a track from the look-up tables and the testing of conditions (8.7) and (8.8). The second assumes that we enumerate all possible tracks coming from the target. A simulation shows that there are 6000 possible tracks for one spectrometer arm. Pairs of track numbers in the two arms are then used as a 26-bit address for lookup in a 64 Mbit table. If the address cell of this table contains 1 (flag of positive decision) it means that the pair satisfies criteria (8.7) and (8.8).

The choice between these two methods has not been done yet. In any case, the total time of decision will be 1 μs if each arm contains one track, and 3 μs if there are two tracks in each arm.

8.7 Data acquisition system.

The data acquisition system consists of five subsystems: drift chamber readout system; ADC and high resolution TDC system; readout electronics of the $SciFi$ detector; fast processors for rejection of bad events and a VME-based system for data collection, processing and recording.

During a spill the data from the detectors are recorded in readout subsystems and collected in buffer memories (see Figure 8.5). Within the interval between spills the data are processed by VME processors and transferred to tape and to the host computer. All readout subsystems transfer data to the buffer memories in parallel. This allows to reduce the dead time of the setup. All second level Trigger 2 (T2) events are recorded in all subsystems simultaneously and all fourth level Trigger 4 (T4) events are transferred to the buffer memories in a parallel manner. Below, each subsystem is shortly described.

8.7.1 Drift chamber readout system.

The system (Figure 8.3) consists of amplifiers (B), time-to-digital convertors (TDC), bus drivers (BD), and buffer memories (FIFO). The amplifier boards are placed immediately on the signal planes of the drift chambers and TDC units are placed on special mother boards closely to the drift chambers (Figure 8.4).

The TDC boards are linked by a data bus (32 bits) which is attached (via the bus driver) to the FIFO. In each telescope all Y and W signal planes are linked by the only

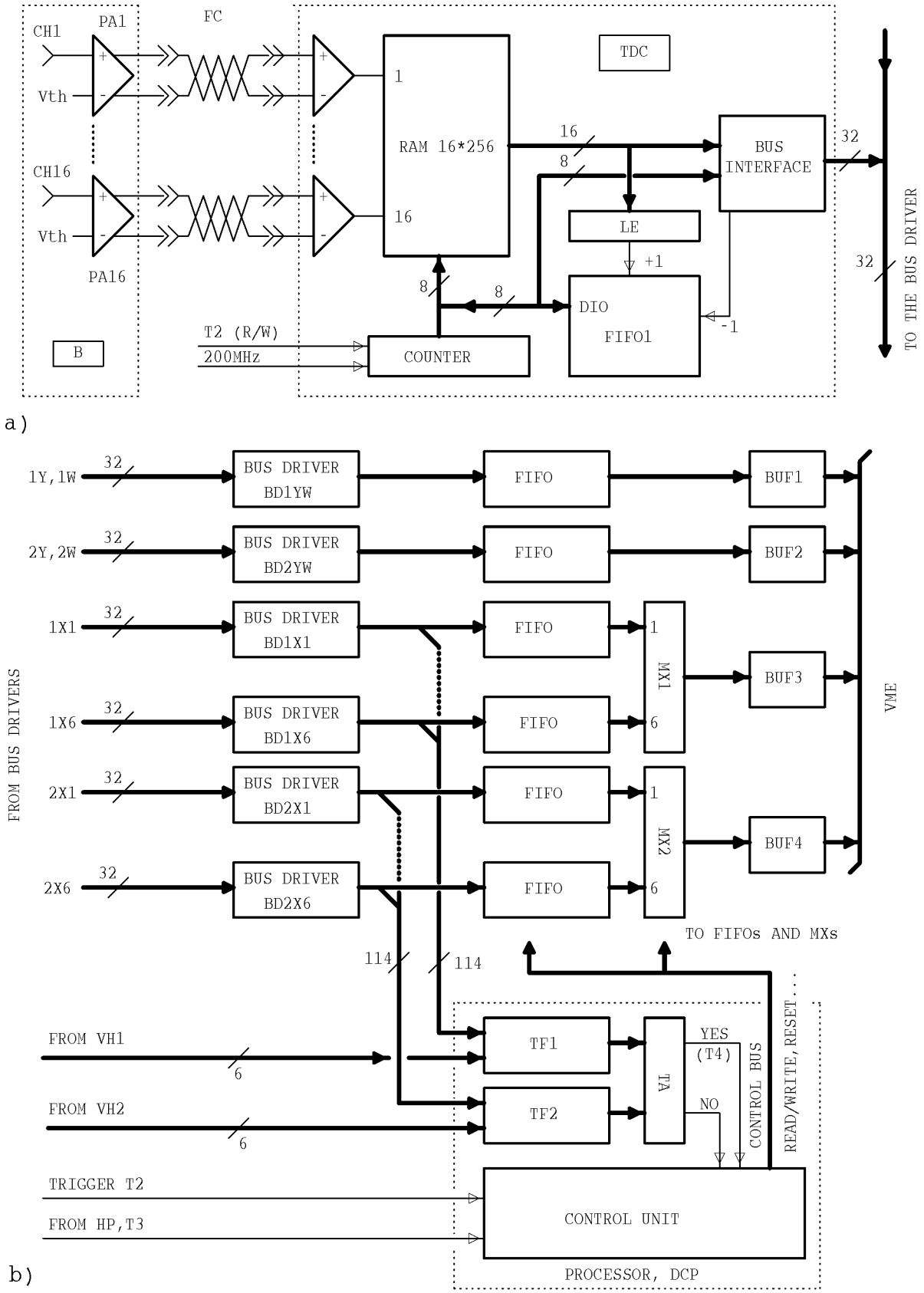

Figure 8.3: Scheme of the drift chamber readout system and processor.

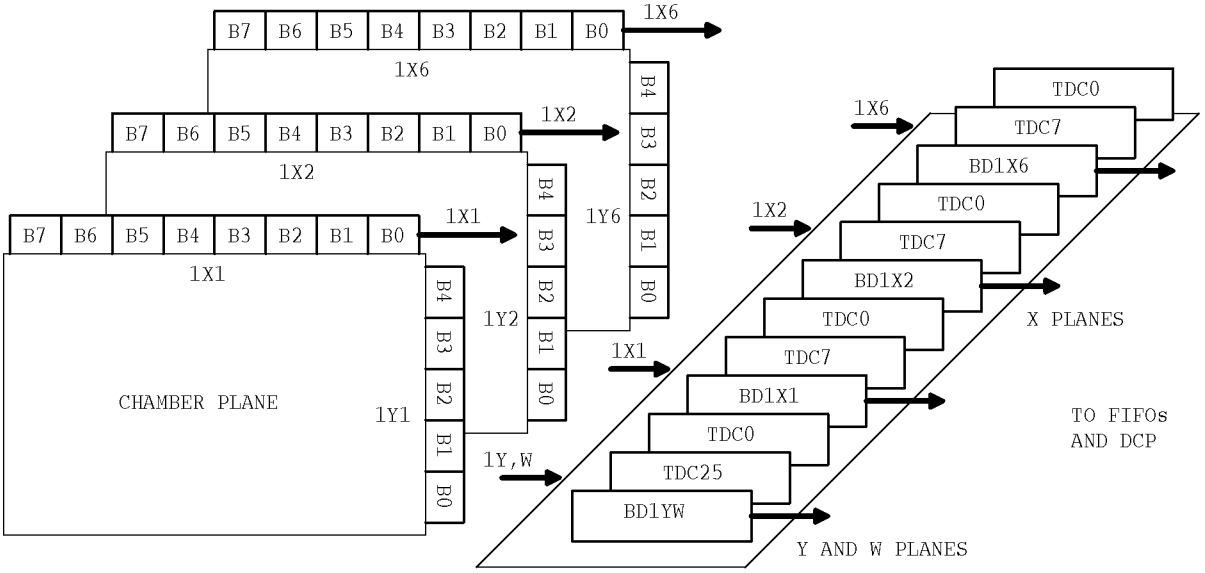

Figure 8.4: The placement of the amplifiers and TDCs

data bus, but X signal planes have individual data buses. This allows to reduce the access time to the hit wires in X planes what is needed to obtain the decision of the DCP in a shorter time.

The 16-channel amplifier board B (Figure 8.3a) contains 16 amplifiers and discriminators PA. Output digital signals are transferred to the TDC units via the twisted pair flat cables (FC). The TDC unit is based on circular memory RAM of 16×256 bits (CY100E422). During the write phase the hits are recorded in memory cells with a frequency of 200 MHz. The second level Trigger 2 changes the write mode into a conversion mode. During this conversion phase the memory address counter is incremented and contents of memory cells are passed to the leading edge detector LE. Only cells that correspond to the drift chamber gate are read out. Each time when the LE detects a hit the address of the memory cell is loaded into FIFO1 (Figure 8.3a). After the conversion phase, FIFO1 stores the numbers of memory cells in which the leading edges of hit wires are recorded. After data conversion the bus drivers (Figure 8.3b) start the data readout. During readout FIFO1 is decremented and the hit patterns (16 bits) along with number of the corresponding memory cell are transferred to the FIFOs. Note that only valid data words are transferred to the FIFOs. The data format of the drift chamber data bus is shown below:

31	30	29	28	27	26	25	24	23	22	21	20	19	18	17	16	15	...	1	0
M2	M1	S7	S6	S5	S4	S3	S2	S1	S0	P2	P1	P0	B2	B1	B0	X	...	X	X
M2	M1	T7	T6	T5	T4	T3	T2	T1	T0	P2	P1	P0	B2	B1	B0	HIT PATTERNS			

where M = marker, S = memory address at Trigger 2, T = memory addresses in which the leading edges were detected, P = number of the signal plane, B = board number in the plane, X = do not care. The drift time is calculated as $t_d = (T - S) \cdot 5$ ns.

After the transfer of the X coordinates to the FIFOs (Figure 8.3b) the drift chamber processor DCP handles these to check the event. If the event is accepted, data from the FIFOs and all other subsystems are loaded to the VME buffer memories (Figure 8.3b,YES), otherwise the recorded event is discarded (NO).

8.7.2 ADC and TDC system.

To convert and read out data from the scintillation hodoscopes, Cherenkov counters and the $SciFi$ detector (if necessary) we intend to use FERA ADC and FERA TDC systems from LeCroy (models 4300B and 4303). ADCs and TDCs are gated by Trigger 2 and cleared by a NO decision (Figure 8.5).

8.7.3 Readout system for the $SciFi$ detector.

The system is based on circular memories (similar as RAM in TDC for drift chamber, Figure 8.3a). During the write phase the memory address counter is clocked with a frequency of 200 MHz and the numbers of fired fibres are recorded in the memory cells. The second level trigger (T2) changes the write phase to the read one. In the read phase the memory cells which correspond to the fibre detector gate are selected. For the fourth level trigger (T4) events the data from these memory cells are transferred into buffer memory (BUF7). This scheme allows to eliminate delay lines and read out data of the $SciFi$ detector in parallel with other subsystems.

8.7.4 Fast processors.

To reject bad events two fast processors will be used in the setup. The first one, the hodoscope processor HP (see Section 8.5 and Figure 8.5), is started by the second level Trigger 2.

After 100 ns (decision time) either the recorded event is discarded or a third level Trigger 3 (T3) signal is issued (if the event is accepted).

The second processor, DCP, handles hit wires of the DC (Section 8.6). This processor reconstructs tracks in the X projection of DC and VH. The processor consists of three units: TF1, TF2 — track finders of telescopes 1 and 2, and track analyzer TA (Figure 8.3b). The identifiers of detected tracks are fed into TA which handles these to produce a final decision. In order to have a minimal decision time the data from the chamber planes are transferred to DCP in parallel. The decision time of the DCP will not exceed 5 μs (including data readout).

DCP is started by Trigger 2 also. If the event is accepted (HP=YES AND DCP=YES) then DCP issues a fourth level Trigger 4, otherwise DCP generates a CLEAR signal (NO). Note that a CLEAR signal is generated in 100 ns after T2 if HP=NO and in 5 μs if HP=YES but DCP=NO.

8.7.5 System for data collection, processing and recording.

This VME-based system (Figure 8.5) consists of standard modules from CES. During a spill good events are loaded into triple port memories HSM8170 (BUF1-BUF7) via ECL ports. Within the interval between spills the recorded events are handled by fast intelligent controller FIC8234 and written on tape. VME and CAMAC crates are connected to the host computer via VICbus. In Figure 8.5 'VIC' stands for the VIC/VME interface module VIC8251F, 'VCC' for the VIC/CAMAC interface module VCC2117.

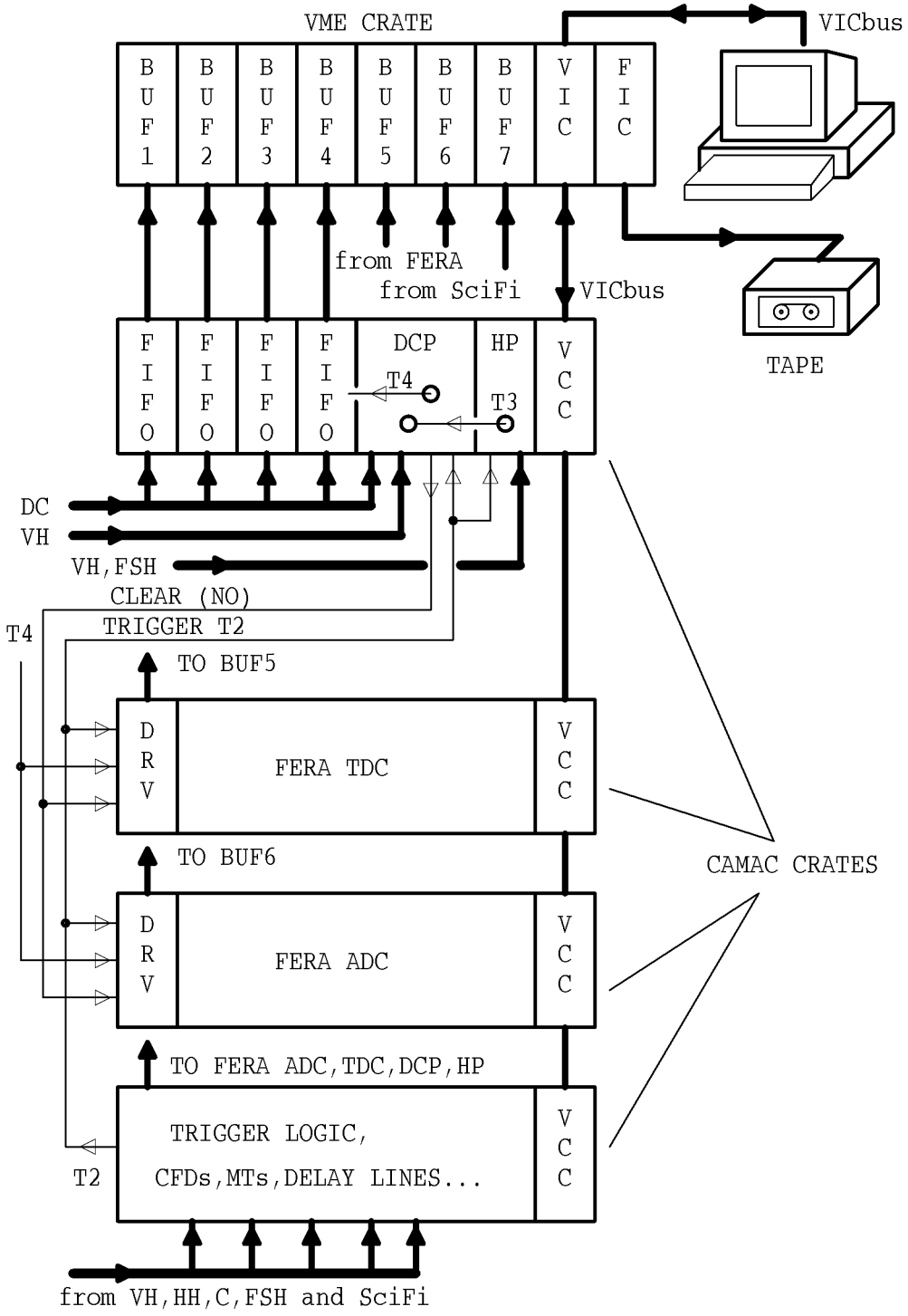

Figure 8.5: Scheme of the data acquisition system.

For the VME-based data collection, the intention is to use CASCADE, a general purpose real time data acquisition package developed and supported by the CERN ECP–DS group. CASCADE runs on the hardware platform (CES FIC 8234 VME CPU and SUN workstation) and the software platform (OS–9 and SUNOS) foreseen in the DAQ architecture that we propose. The expected volume of data and event rate, as described in Chapter 11, can be handled by CASCADE.

8.7.6 Main parameters of the data acquisition system.

1. *DC* system: threshold range is Vth = 1 – 10 μA; least count is 5 ns; data conversion time is 200 ns; data transfer rate is 50 ns/word.

2. FERA system: conversion time is 4.8 μs; dynamic range is 10 bits; least count is 250 fC (ADC) and 50 ps (TDC). Data transfer rate is 100 ns/word.

3. Dead time of the data acquisition system for events rejected:

   - by the third level of trigger — 1 μs;
   - by the fourth level of trigger — 6 μs;

   Dead time for accepted events — 8 μs.

4. Maximum number of fourth level triggers per spill — is determined by the volume of buffer memory. Note that HSM8170 is the cascadable memory, therefore the memory volume can be easy expanded if necessary.

Chapter 9

The $\pi^+\pi^-$ atom and particles yields

In this chapter we estimate the yields of charged particles and of atoms to be expected. This will be used to evaluate the required performance of the experimental setup, the detector counting rates and the volume of information to be written to tape.

The expression that relates the inclusive cross section of the atom production to the inclusive cross section of π^+ and π^- meson production in a free state has been given in Section 3.1, equations (3.1, 3.2).

The number of π mesons and atoms per one interacting proton is calculated using the inelastic cross section value σ_{in}

$$\frac{dN}{d\vec{p}} = \frac{d\sigma}{d\vec{p}}\frac{1}{\sigma_{in}}.$$

We need π meson and $A_{2\pi}$ yields per interacting proton $dN/(dp \cdot d\Omega \cdot 1 \text{ proton})$ as a function of the laboratory angle and into the angular aperture of the experimental setup $dN/(dp \cdot 1 \text{ proton})$.

9.1 Lund model, phenomenological formula and experimental data

For the estimation of the particle yields we have used the simulation Lund program FRITIOF 6.0.

In order to be convinced of the reliability of the calculations the results have been compared with the $\pi^{\pm}$ meson yields obtained experimentally [EICH72] in pA-interactions (A = Be, Al, Cu, Pb) at proton energy of 24 GeV and for π meson laboratory emission angles Θ in the interval 17 to 137 mrad.

The experimental data [EICH72] were obtained with an accuracy of $\pm 15\%$. The errors in the experimental data arose mainly from uncertainties in the spectrometer acceptance and in the absolute calibration of the primary proton beam intensity.

The discrepancy between the experimental data and the Lund model does not exceed $15 \div 20\%$ as a rule. It was found that the experimental data in the most interesting angular region ($37 \div 87$ mrad) lie somewhat lower than simulated data.

The experimental data [EICH72] were only obtained for π meson laboratory momenta $p_\pi > 4$ GeV/c and consequently the simulated π meson distributions at $p_\pi < 4$ GeV/c cannot be compared to experimental data.

We have used a phenomenological formula to compare particle production rates calculated with the Lund model for the whole interval of the π meson momenta. There are many empirical formulae to describe inclusive cross sections of the π meson production. We have used an analytical representation of π meson differential cross sections for pp-collisions [BADH77].

The formula was checked in [BADH77] using the experimental data for which $p_\perp^{min} = 0.2$ GeV/c, however. In our case the $p_\perp$ values are much smaller ($p_\perp^{min} = 0.04$ GeV/c). The validity of the phenomenological formula needs therefore further investigation.

To this aim, we have used the experimental data on differential cross section of $\pi^\pm$ meson production in pp-collisions: [ROSS75] — data compilation, [GUET76] — $\sqrt{s} = 23$ and 45 GeV, [AKER71] — $p_\mathrm{p} = 12.45$ GeV/c, [DIDD64] — $p_\mathrm{p} = 19$ and 24 GeV/c, [DEKK65] — $p_\mathrm{p} = 18.8$ and 23 GeV/c and [ALLA70] — $p_\mathrm{p} = 12.2$ GeV/c.

The formula describes the data with accuracy of 20% except [DEKK65] which are badly described at 0°. Unfortunately experimental data on differential cross sections of π meson production in the region of interest $\Theta = 2° \div 5°$ and the lab momentum $p_\pi = (1 \div 4)$ GeV/c are missing.

The formula describes the particle yields in pp-collisions only. So to take into account the dependence of the π meson yield on the target atomic number the results of the Lund simulation were used. On the base of these results we obtain the ratios K(Θ) of π meson yields for Be, Al, Cu and Pb nuclei to those for hydrogen as a function of emission angle. The phenomenological formula was multiplied by K(Θ) so that A-dependence of π meson yield could be taken into account.

Finally the momentum distributions of $\pi^\pm$ mesons obtained with the formula were multiplied by a factor 0.7 in order to equate the calculated yields of π mesons to the experimental data [EICH72] at the π meson momentum 5 GeV/c, so that the distributions of pions into the setup aperture are close to the calculated ones with the Lund model (see Figure 9.1). Hence, we believe that using of the Lund model will not introduce a large error in the evaluation of the conditions of the proposed experiment.

9.2 Yields of $\pi^\pm$ mesons and other charged particles

Distributions of π^+ and π^- mesons reaching the aperture of the experimental setup in the case of p Ti interactions at 24 GeV obtained as described above are shown in Figure 9.1. In the same figures the distributions of the π mesons from short-lived sources only are also given.

The distributions of $\pi^\pm$ mesons from short-lived sources are of more interest as long-lived sources like η, η', Λ, K_s^0, Σ which also contribute to the inclusive cross sections of π meson production do not contribute to $\pi^+\pi^-$ atom formation . Of course the formula describes the total π meson yields, both for the long-lived and short-lived sources.

One can see that the Lund model and the formula give results that differ by $\leq$20% in the π meson momentum region of interest ($1 \div 4$ GeV/c).

The particle production rates, detector counting rates and trigger rates have been simulated. As input data, we have used the particle yields $dN/dp/d\Theta$ obtained from

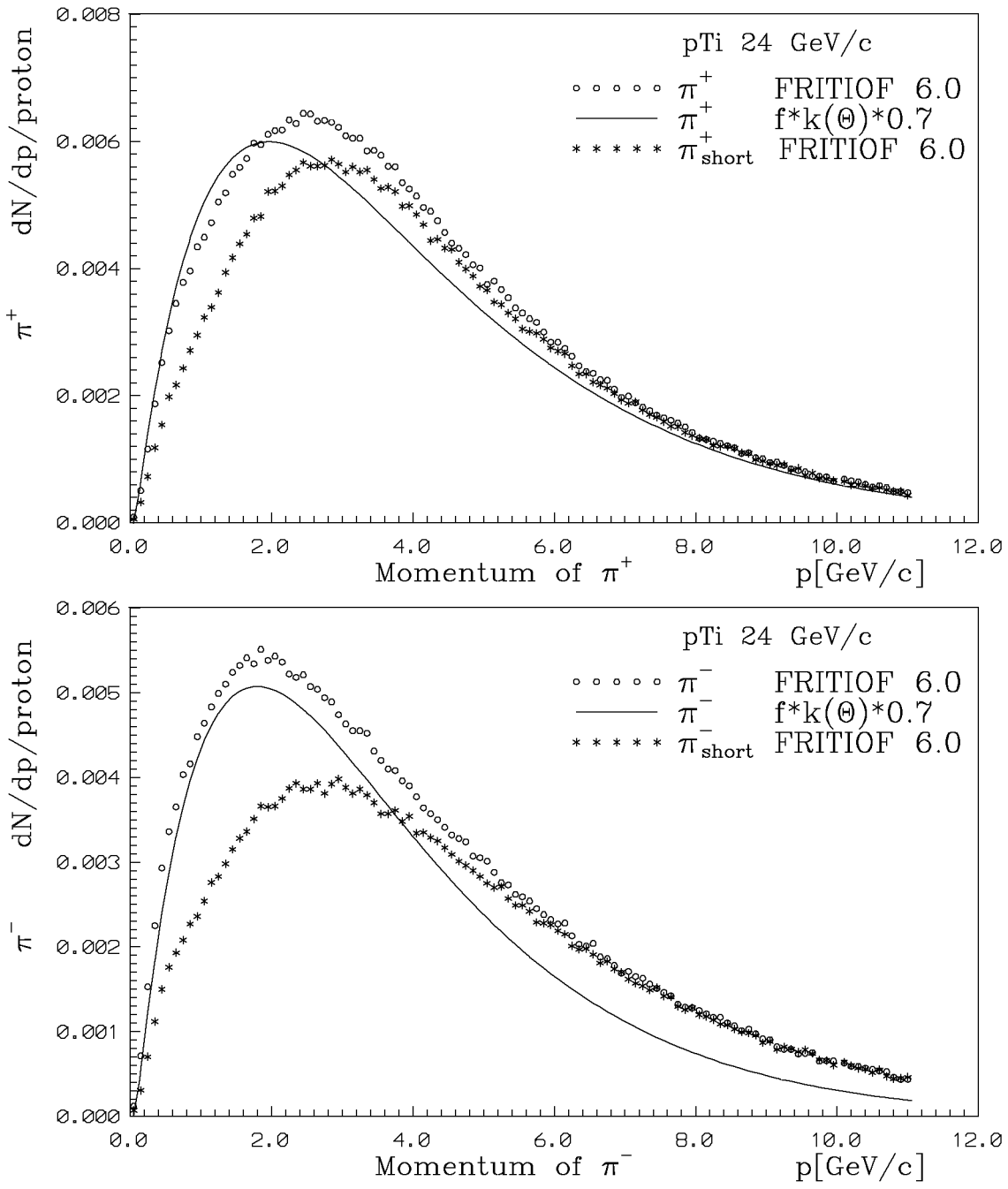

Figure 9.1: Yield of π^+ and π^- mesons versus lab momentum per p Ti interaction into the angular aperture of the setup. FRITIOF 6.0: long-lived and short-lived sources (circles), short-lived sources only (asterisks) and the yield obtained with the empiric formula [BADH77] (solid line).

Table 9.1: Particle productions per proton-Ti interaction

Particle	In the channel aperture	In momentum range	Ratio
π^+ short	$3.0 \cdot 10^{-2}$	$1.5 \cdot 10^{-2}$	0.51
π^+ long	$3.6 \cdot 10^{-3}$	$2.1 \cdot 10^{-3}$	0.58
π^- short	$2.3 \cdot 10^{-2}$	$1.1 \cdot 10^{-2}$	0.47
π^- long	$5.2 \cdot 10^{-3}$	$3.3 \cdot 10^{-3}$	0.63
K^+	$3.8 \cdot 10^{-3}$	$1.2 \cdot 10^{-3}$	0.33
K^-	$1.5 \cdot 10^{-3}$	$5.4 \cdot 10^{-4}$	0.35
p	$4.1 \cdot 10^{-2}$	$6.8 \cdot 10^{-3}$	0.17
$\bar{\text{p}}$	$6.4 \cdot 10^{-4}$	$3.5 \cdot 10^{-4}$	0.55
γ	$6.2 \cdot 10^{-2}$	0.	0.
e^+	$1.25 \cdot 10^{-3}$	$3.9 \cdot 10^{-4}$	0.31
e^-	$1.25 \cdot 10^{-3}$	$3.9 \cdot 10^{-4}$	0.31

FRITIOF. The multiplicity of particles of each kind was generated using Poisson distribution with a mean value obtained as the integral of $dN/dp/d\Theta$ over the setup aperture and over particle momentum. We took into account charged pions, kaons and protons. Electrons and positrons, coming from conversion of gamma quanta in the target, fibre and ionization detectors, have been considered too. For pions from short-lived sources the Coulomb correlations were taken into account. For all hadrons, strong correlations increased the correlated particle yields by 1.65.

Figure 9.2 shows the expected particle spectra into the channel aperture. We see that the proton production is the most intense process along with the π meson production.

The relative contribution of pions to the spectrum of all detected charged particles can be seen in Figure 9.3. The distributions for charged particles are given for all particles passing through the channel and through the detectors.

The mean yields of particles reaching the secondary particle channel as well as getting into the spectrometer momentum range per p Ti-interaction are presented in Table 9.1. As mentioned above the electrons and positrons come from conversion of gamma quanta in the target (175 μm Ti) and from the fibre and ionization detectors (9 mm scintillator). The last column in Table 9.1 shows which part of produced particles may be detected by one or another arm of the spectrometer.

The mean number of all charged particles emitted into the channel per a single p Ti-interaction in the whole momentum interval is:

$$\bar{n}_{ch} = 1.1 \cdot 10^{-1} .$$

The mean number of positive and negative charged particles hitting the hodoscopes are:

$$\bar{n}'_{+} = 2.5 \cdot 10^{-2}, \quad \bar{n}'_{-} = 1.6 \cdot 10^{-2} .$$

The probability to detect a pair of oppositely charged hadrons from one act of proton-target interaction is:

$$P_{\text{real}} = 1.1 \cdot 10^{-4} .$$

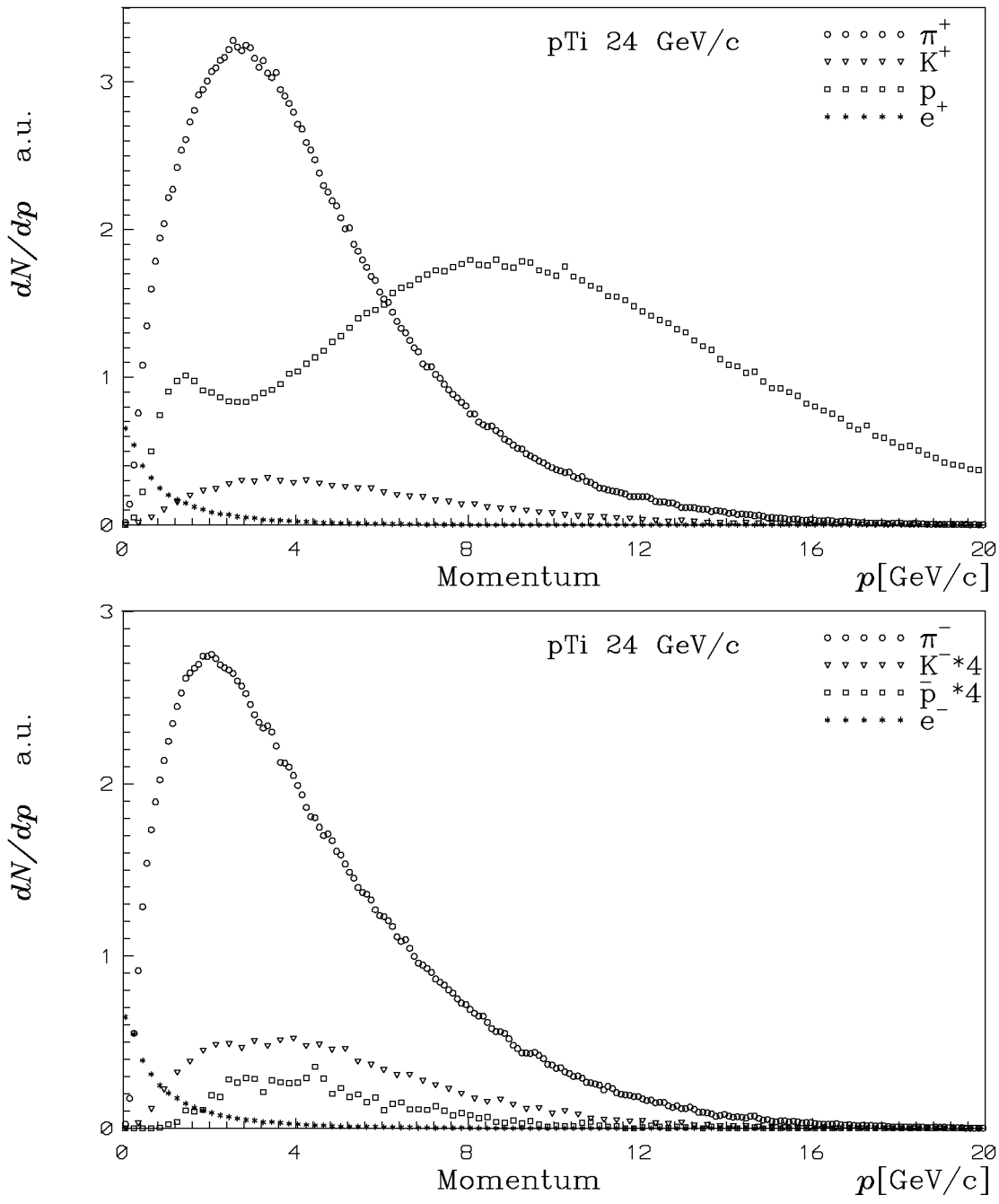

Figure 9.2: Spectra of secondary particles into the channel angular aperture of $2.5 \cdot 10^{-3}$ sr obtained with FRITIOF 6.0. Spectra of K^- and $\bar{p}$ are multiplied by 4.

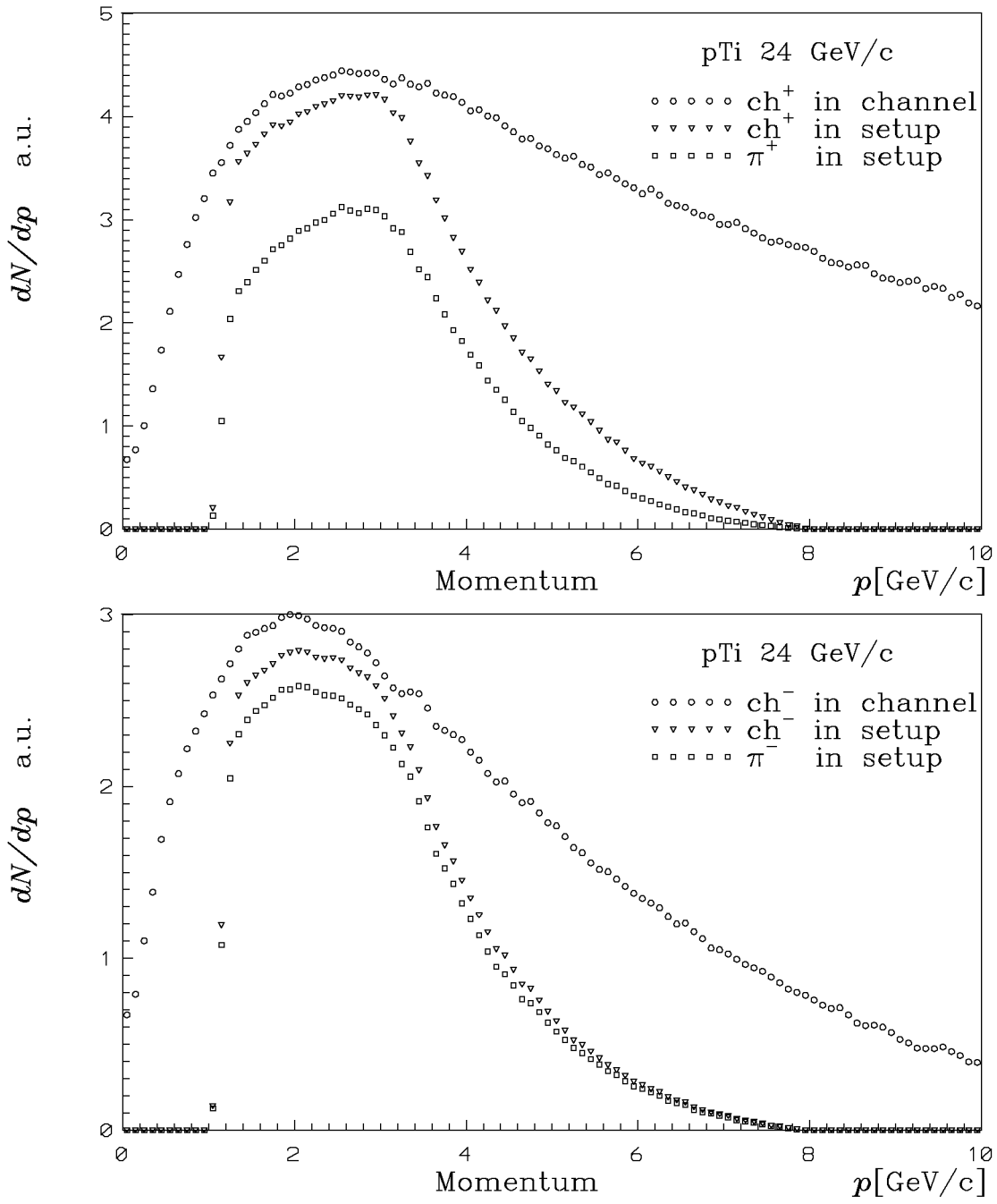

Figure 9.3: Spectra of all charged particles passing through the channel angular aperture (circles) and through the detectors (triangles) and for only pions detected (squares). Particle decays along the channel have been taken into account.

Table 9.2: Probabilities to meet N particles in the detectors for the first level trigger events.

N	$SciFi$	HH_1+HH_2	HH_1	HH_2
1	0.	0.	0.849	0.919
2	0.563	0.786	0.128	$7.6 \cdot 10^{-2}$
3	0.308	0.177	$2.23 \cdot 10^{-2}$	$4.5 \cdot 10^{-3}$
4	$9.81 \cdot 10^{-2}$	$2.88 \cdot 10^{-2}$	$7.82 \cdot 10^{-3}$	$1.1 \cdot 10^{-4}$
5	$2.50 \cdot 10^{-2}$	$8.58 \cdot 10^{-3}$	0.	0.
6	$5.9 \cdot 10^{-3}$	$4.3 \cdot 10^{-5}$	0.	0.
7	$3.2 \cdot 10^{-4}$	0.	0.	0.
average	2.61	2.26	1.20	1.08

For primary proton flux 10^{11} per spill and trigger resolution time 20 ns the probability to have a real or accidental coincidence per proton-target interaction is:

$$P_{\rm tot} = 4.1 \cdot 10^{-4} \, .$$

In these conditions, the number of e^+e^- pairs per proton-target interaction is $1.4 \cdot 10^{-4}$ in the momentum range of the setup.

In Table 9.2 the distributions on the number of particles in the fibre detector ($SciFi$) and in the hodoscopes (HH_1 and HH_2) are shown for an initial proton flux of 10^{11} per spill and a trigger resolution time of 20 ns. These distributions have been obtained for events passing the first level trigger. The fact that the mean value of particles in HH_1 is larger than in HH_2 is due to the contribution of protons.

Note that in this chapter all the data are obtained for secondary particles produced in the target. The particle production in elements of the experimental setup will be discussed in Chapter 11.

9.3 Yields of $\pi^+\pi^-$ atoms

For calculation of $\pi^+\pi^-$ atom yields we have used the relationship (3.1) and $\pi^\pm$ meson yields obtained with FRITIOF 6.0.

The spectrum of the $A_{2\pi}$ atoms into the channel aperture and the spectrum of atomic pairs versus total momentum of pair (at the atom breakup probability equal to 100%) in the momentum range of the setup are shown in Figure 9.4. Only short-lived sources were considered.

For the atom yield calculation we used the strong interaction correlation coefficient for $\pi^+\pi^-$-pairs in the final state at small relative momenta which is equal to $R = 1.65$ [GRIS82, URIB94].

The calculations gave the mean number of $A_{2\pi}$ into the aperture of the setup per p Ti-interaction for the whole $A_{2\pi}$ momentum interval $0 \div 20$ GeV/c:

$$\bar{n}_1^a = 1.33 \cdot 10^{-8} \, ;$$

for the setup momentum acceptance:

$$\bar{n}_2^a = 0.71 \cdot 10^{-8} \, .$$

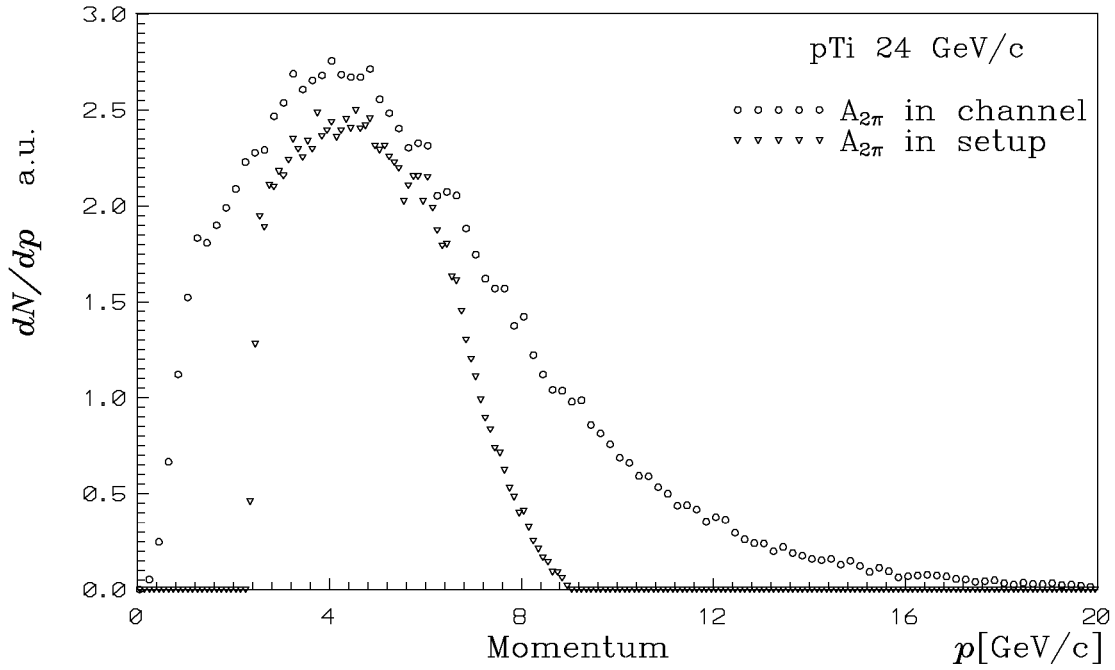

Figure 9.4: Spectra of $A_{2\pi}$ in the channel angular aperture (circles) and "through the detectors" (triangles). Particle decays along the channel have been allowed.

The ratio of $\bar{n}_2^a$ to $\bar{n}_1^a$ is equal 0.53 and gives the fraction of atoms which could be detected by the setup from the total number of atoms produced in the target.

Chapter 10

Simulation of the setup performance

10.1 Simulation procedure

Simulations have been done to estimate the momentum and coordinate resolution of the experimental setup. Both the atomic and free $\pi^+\pi^-$ pairs were simulated. The absolute value of the relative momentum and emitting angles for π^+ and π^- have been simulated assuming that the $A_{2\pi}$ breakup occurs from the ground state.

The full simulation procedure includes: the event generation ($A_{2\pi}$ or free pairs), the particle passage through the experimental setup and the reconstruction of tracks. For the first step, the spectra of free pairs and $A_{2\pi}$ were simulated using the empiric formula [BADH77]. The momentum varied from 1.8 to 8.8 GeV/c for $A_{2\pi}$ and from 0.8 to 6.8 GeV/c for π^+ and π^- from free pairs. $\pi^\pm$ from free pairs and $A_{2\pi}$ were simulated uniformly into the angular aperture of the setup ($\pm 1.5^\circ$ in the horizontal and vertical planes). The proton beam distribution on the target was taken into account.

In another version of event generation the $A_{2\pi}$ momentum was fixed to some values and the angle between $A_{2\pi}$ and the channel axis was fixed to be zero.

The passage of particles through the experimental setup was simulated with taking into account multiple scattering in the target, in the detectors upstream of the magnet ($SciFi$ and FSH), in the output membrane, in air and in the drift chambers. In all media the multiple scattering was calculated according to the Scott-Snyder-Moliere theory except for the drift chambers where a Gaussian distribution was applied.

$SciFi$ consists of scintillating fibre detectors with 0.25 mm pitch for X and Y coordinates. The pitch was varied in the simulation. The real dependence of the double-hit resolution (see Figure 7.6) was taken into account.

Having calculated the angles and coordinates of a particle at the output membrane, the passage of a particle through the drift chambers was simulated and, as a result, the hit wire numbers and coordinates were obtained. The efficiency of DC was assumed to be 100%.

The last step of the simulation was the event reconstruction. Using the simulated data in the drift chambers the tracks were reconstructed with 6 coordinate planes (W planes were not considered) by the least square method and the angles and coordinates of a particle in the first drift chamber plane were calculated. The accuracy of the drift chambers was taken into account in this process using a Gaussian distribution in each plane with variable standard deviation. Track parameters obtained in such a way were used for particle tracking through the magnetic field to obtain the angles and coordinates upstream of the magnet.

The magnetic field was considered in the box approximation. For track reconstruction, the particles were assumed to be emitted from the center of the target in one case and from the center of hit fibre of $SciFi$ in another. The angles and coordinates of the particles were calculated using formulas that connect angles and coordinates at the input and output of the magnetic field.

Basic data for simulation.

1. Proton beam characteristics: $\sigma_X = 1.5$ mm, $\sigma_Y = 1.0$ mm, where σ_X and σ_Y are the standard deviations of a Gaussian distribution in the horizontal and vertical planes.
2. The value of target thickness is $L_{\rm targ} = 0.175$ mm of titanium ($L_{\rm rad} = 35.94$ mm).
3. The pitch of $SciFi$ is 0.25 mm (except in Table 10.4). Total thickness of the detectors in the channel is 9 mm ($L_{\rm rad} = 42.4$ cm).
4. Magnetic field: $B = 1.65$ T, $L_{\rm eff} = 2$ T·m.
5. Output membrane: thickness is 0.4 mm of aluminium ($L_{\rm rad} = 89$ mm).
6. Drift chambers: accuracy is $\sigma_{DC} = 0.2$ mm (except for Table 10.2).

Adopted notations in tables and figures.

1. p_π—pion momentum in lab system.
2. $q^{\rm in}, q^{\rm out}$—initial (in) and reconstructed (out) relative momenta of the $\pi^+\pi^-$ pairs coming from a breakup of $A_{2\pi}$ (atomic pairs); q is the relative momentum in the c.m.s. of the pair.
3. $q_L^{\rm in}$, $q_L^{\rm out}$—initial (in) and reconstructed (out) $q^{\rm in}$ and $q^{\rm out}$ projections to the $\vec{p} = \vec{p}_{\pi^+} + \vec{p}_{\pi^-}$ direction.
4. $q_T^{\rm in}$, $q_T^{\rm out}$—initial (in) and reconstructed (out) $q^{\rm in}$ and $q^{\rm out}$ projections to the plane perpendicular to the $\vec{p} = \vec{p}_{\pi^+} + \vec{p}_{\pi^-}$ direction.
5. $q_X^{\rm in}$, $q_X^{\rm out}$, $q_Y^{\rm in}$ and $q_Y^{\rm out}$—initial (in) and reconstructed (out) X and Y components of $q_T^{\rm in}$ and $q_T^{\rm out}$.
6. R—ratio of number of atomic pairs with $q^{\rm out} < 2$ MeV/c to the whole number of atomic pairs.
7. K—ratio of number of atomic pairs passed through a single fibre simultaneously in X and Y planes of $SciFi$ to the whole number of atomic pairs (in percent).
8. $\sigma(q_X)$, $\sigma(q_Y)$, $\sigma(q_L)$—standard deviations for differences between initial and reconstructed values of q projections.
9. $\sigma(p)$—standard deviation of the pion momentum calculated with pion trajectory traced to the point in the center of the beam on the target.
10. $\sigma(X)$, $\sigma(Y)$—standard deviations of the pion coordinate in the $SciFi$ plane calculated with pion trajectory traced to the point in the center of the beam on the target.

10.2 Results of the simulation

Results of simulations are given in the following tables and pictures. The accuracy characteristics of the experimental setup are presented in Tables 10.1 – 10.4. Data presented illustrate the properties of the detected processes and were used to choose the detector parameters and rejection procedures discussed above.

The accuracy of the detectors leads to a linearly increasing error $\sigma(p)/p$ with increasing of momentum values, while the multiple scattering in the setup elements contributes a constant part in the total $\sigma(p)/p$ uncertainty.

The values of $\sigma(X)$ and $\sigma(Y)$ include constant parts which correspond to the detector accuracy, while a momentum dependence is explained by multiple scattering in the setup elements. It is seen from Tables 10.1 and 10.2 that uncertainties in $\sigma(p)/p$, $\sigma(X)$ and $\sigma(Y)$ are determined only by multiple scattering if the resolution of DC chamber is better than 0.2 mm .

Table 10.1: Dependence of momentum and coordinate reconstruction accuracy on the pion momentum.

p_π (GeV/c)	$\sigma(p)/p$ %	$\sigma(X)$ (mm)	$\sigma(Y)$ (mm)
1.1	0.37	2.51	2.45
2.5	0.40	1.25	1.19
4.0	0.47	1.11	0.86

Table 10.2: Dependence of momentum and coordinate reconstruction accuracy on the DC resolution at $p_\pi = 2.5$ GeV/c.

σ_{DC} (mm)	$\sigma(p)/p$ %	$\sigma(X)$ (mm)	$\sigma(Y)$ (mm)
0.1	0.40	1.25	1.19
0.2	0.40	1.26	1.19
0.3	0.42	1.27	1.20
0.4	0.44	1.29	1.22

The dependence of R, K, $\sigma(q_X)$, $\sigma(q_Y)$ and $\sigma(q_L)$ on the target thickness is given in Table 10.3 for the atomic pairs coming from the breakup of $A_{2\pi}$ ground state. For comparison the data for dimeson atom in 2S state are shown.

For the optimum target (0.175 mm of titanium) the errors $\sigma(q_X)$ and $\sigma(q_Y)$ are mainly determined by multiple scattering in the target. $\sigma(q_L)$ does not depend on the target thickness. 14% of pions coming from $A_{2\pi}$ break up will be detected in the same pitch of $SciFi$ in both planes. In order not to loose these events, a second kind of $SciFi$ logic decision should be used (see chapter 8.4).

The mean squared values of the distances $\sigma(X)$ and $\sigma(Y)$ between track coordinates obtained with $SciFi$ and with downstream detectors, assuming that the particle is emitted

Table 10.3: Dependence of R, K, $\sigma(q_X)$, $\sigma(q_Y)$ and $\sigma(q_L)$ on the target thickness $L_{\rm targ}$. The spectrum of $A_{2\pi}$ was taking into account in the calculations.

	$L_{\rm targ}$ Ti(mm)	R	K %	$\sigma(q_X)$ (MeV/c)	$\sigma(q_Y)$ (MeV/c)	$\sigma(q_L)$ (MeV/c)
$A_{2\pi}$ (1S)	0.0	0.96	99	0.12	0.12	0.83
	0.035	0.94	51	0.37	0.40	0.83
	0.070	0.91	29	0.55	0.55	0.83
	0.120	0.87	18	0.71	0.72	0.83
	0.175	0.82	14	0.83	0.83	0.83
	0.215	0.78	11	0.93	0.92	0.83
	0.263	0.75	9.2	1.03	1.03	0.83
$A_{2\pi}$ (2S)	0.175	0.86	14.	0.81	0.83	0.83

from the target centre, are shown in Table 10.4 for different values of fibre diameter. The small values of $\sigma(X)$ and $\sigma(Y)$ allow to select the hit fibre corresponding to the track reconstructed in the drift chambers. Probabilities of the hitting the single fibre by "atomic" pairs in both planes are also shown.

Table 10.4: Dependence of coordinate reconstruction accuracy and K on the $SciFi$ pitch $L_{\rm pitch}$. The pion momentum was fixed at $p_\pi = 2.5$ GeV/c in the calculations.

$L_{\rm pitch}$ (mm)	$\sigma(X)$ (mm)	$\sigma(Y)$ (mm)	K %
0.10	1.25	1.17	2.4
0.20	1.26	1.18	9.1
0.25	1.26	1.19	14.
0.30	1.26	1.20	19.
0.50	1.26	1.20	45.

The q-distributions of atomic pairs and their projections q_L and q_T are shown in Figures 10.1, 10.3 and 10.5. These distributions are given for the $A_{2\pi}$ breakup in 1S state as well as distributions for detected atomic pairs. Multiple scattering in the target and the setup precision were taken into account. Similar distributions for free pairs in the channel aperture and for detected pairs are shown in Figures 10.2, 10.4 and 10.6.

The differences of π^+ and π^- coordinates are shown in Figures 10.7 – 10.10 for atomic and free pairs in $SciFi$ and in the scintillation hodoscopes downstream of the magnet. The distributions for atomic pairs are much narrower than these for free pairs. From figures one can see a scale the setup resolution required.

The efficiency of atomic pair detection is given in Figure 10.11. Single particle and free pair efficiencies are shown in Figure 10.12.

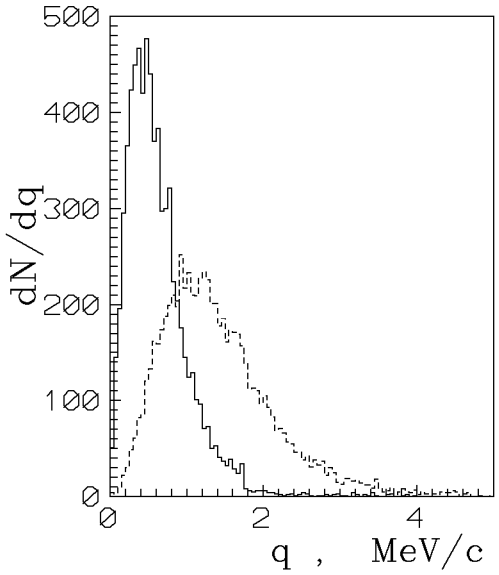

Figure 10.1: Relative momentum distribution of the pairs from breakup of $A_{2\pi}$ in 1S state. Solid line — $q^{\rm in}$ distribution, dashed line—$q^{\rm out}$ distribution.

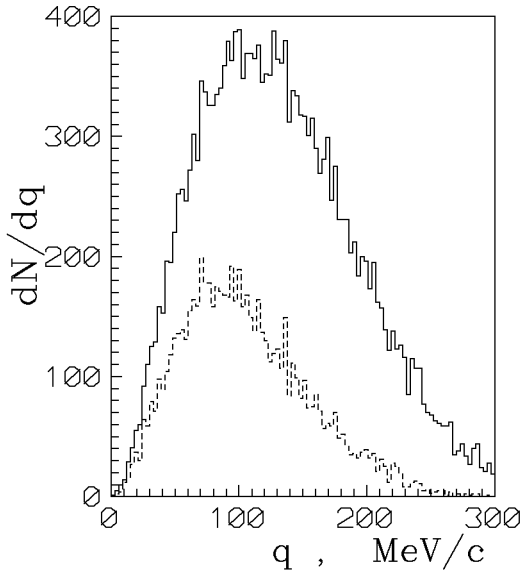

Figure 10.2: Relative momentum distribution of the free $\pi^+\pi^-$ pairs. Solid line—$q^{\rm in}$ distribution, dashed line—$q^{\rm out}$ distribution.

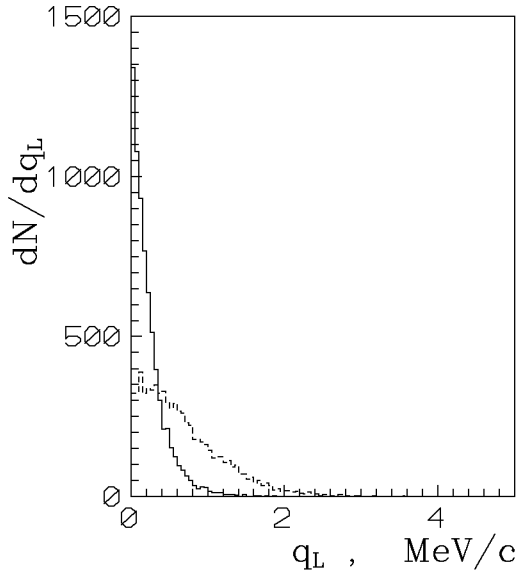

Figure 10.3: q_L distribution of the pairs from breakup of $A_{2\pi}$ in 1S state. Solid line—$q_L^{\rm in}$ distribution, dashed line $-q_L^{\rm out}$ distribution.

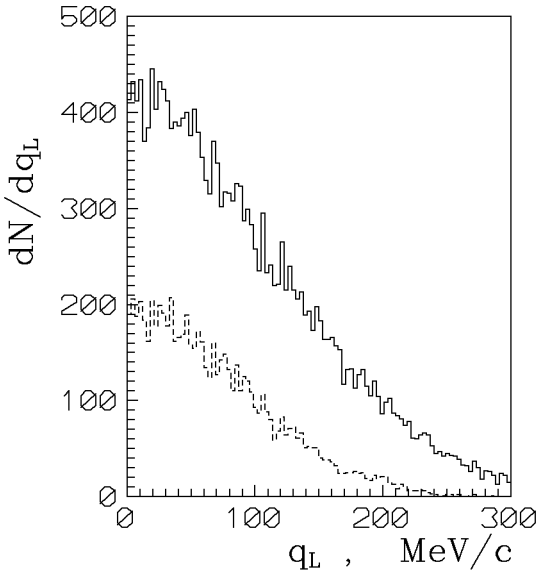

Figure 10.4: q_L distribution of the free $\pi^+\pi^-$ pairs. Solid line—$q_L^{\rm in}$ distribution, dashed line—$q_L^{\rm out}$ distribution.

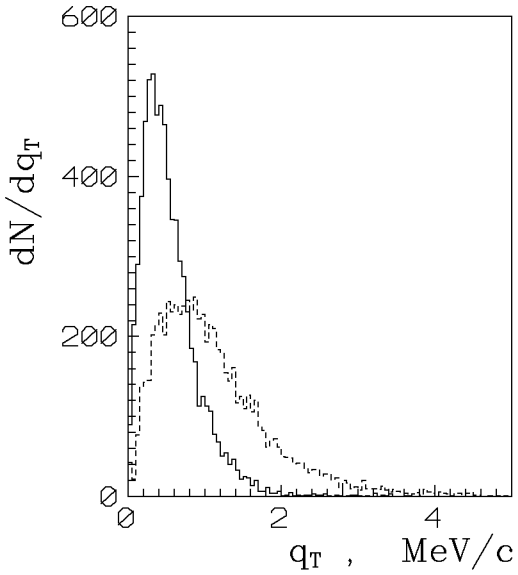

Figure 10.5: q_T distribution of the pairs from breakup of $A_{2\pi}$ in 1S state. Solid line—$q_T^{\rm in}$ distribution, dashed line $-q_T^{\rm out}$ distribution.

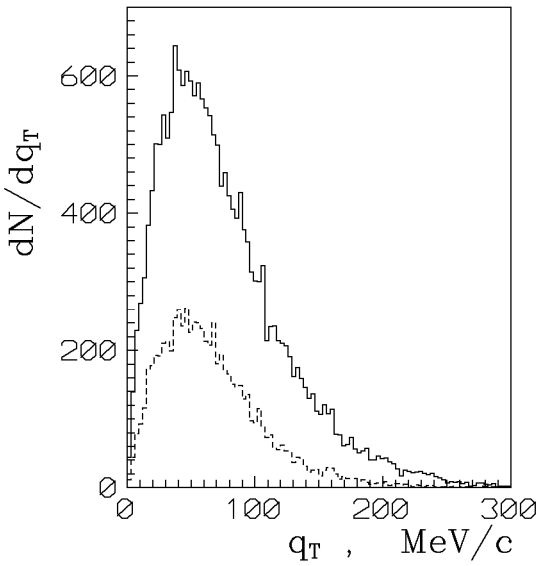

Figure 10.6: q_T distribution of the free $\pi^+\pi^-$ pairs. Solid line—$q_T^{\rm in}$ distribution, dashed line — $q_T^{\rm out}$ distribution.

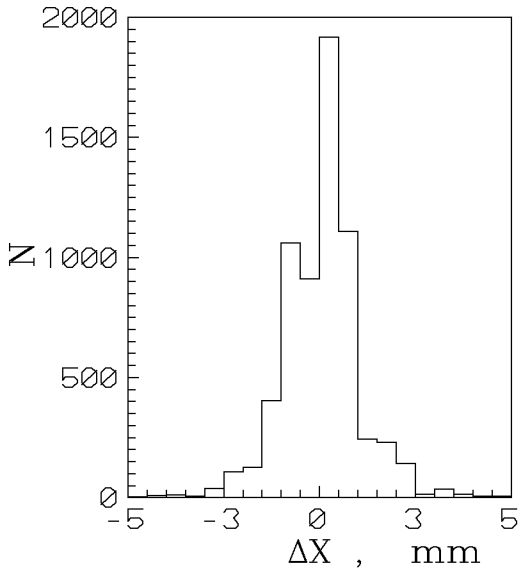

Figure 10.7: Difference in X coordinates in the plane of $SciFi$ for pairs from a breakup of $A_{2\pi}$ in 1S state.

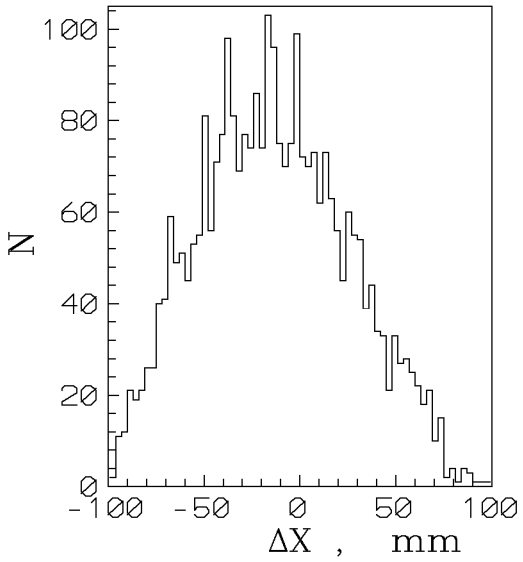

Figure 10.8: Difference in X coordinates in the plane of $SciFi$ for free $\pi^+\pi^-$ pairs.

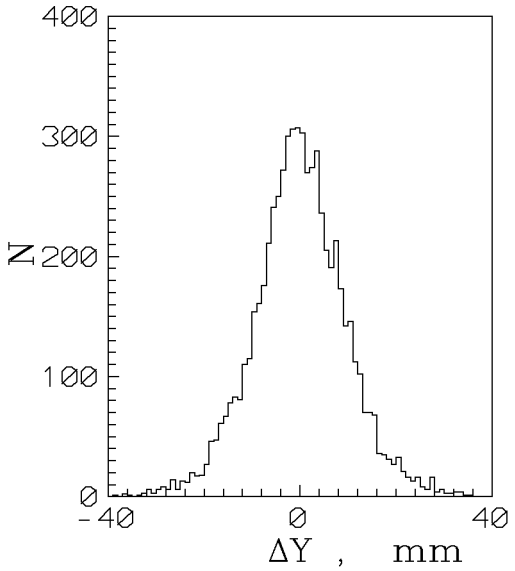

Figure 10.9: Difference in Y coordinates in the scintillation hodoscopes downstream of the magnet (see Fig. 6.3) for pairs from a breakup of $A_{2\pi}$ in 1S state.

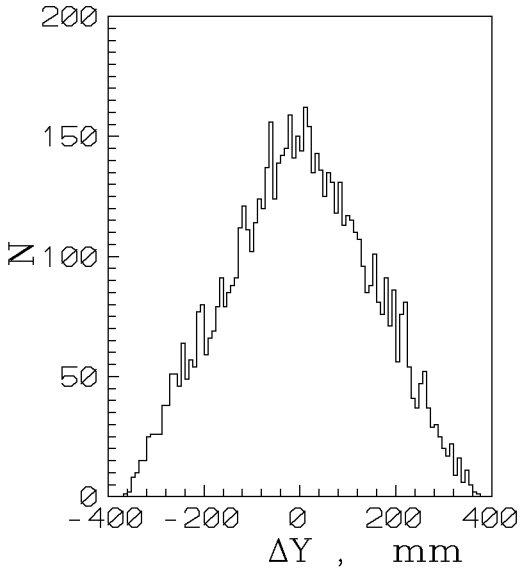

Figure 10.10: Difference in Y coordinates in the scintillation hodoscopes downstream of the magnet (see Fig. 6.3) for free $\pi^+\pi^-$ pairs.

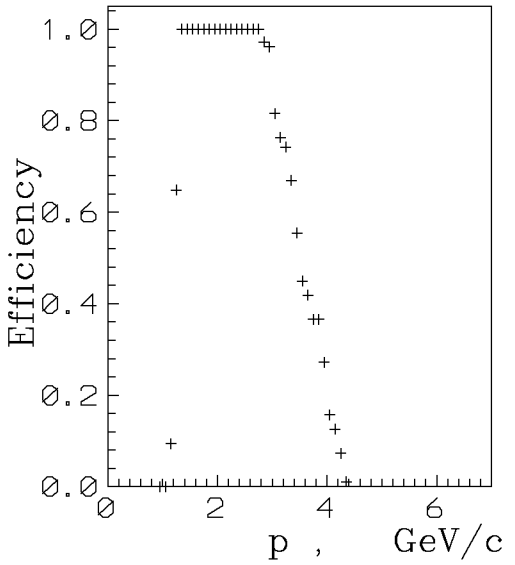

Figure 10.11: Efficiency to detect atomic pairs versus the momentum of pions.

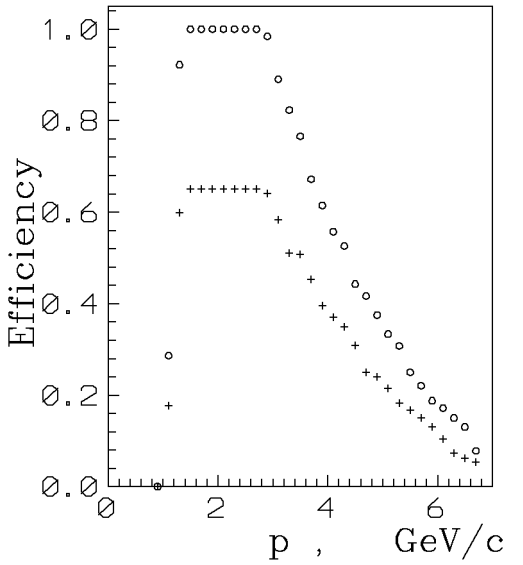

Figure 10.12: Efficiency to detect a single π^+ (π^-)—circles and pion from a free pair—crosses.

Chapter 11

Estimation of trigger rate and runtime

We have calculated the trigger rate for various intensities of the incident proton beam. In this estimation the target made of 175 μm Ti foil was assumed. The probability of proton interaction in this target is $6.3 \cdot 10^{-4}$.

The results for particle flux and trigger rates are presented in Table 11.1. The detector efficiency was supposed to be 100 %. The losses of $A_{2\pi}$ due to the dead time of the electronics and DAQ system were taken into account. The Table includes:

N_p — number of protons in the primary beam per 0.35 s spill,

N_{ch} — number of charged particles in the secondary particle channel per second,

N_+/N_- — number of positive/negative charged hadrons (pions + kaons + protons) in the spectrometer momentum range per second,

Tr.1$\div$Tr.4 — trigger rates at different levels (see Chapter 8) per second,

$\frac{\text{Acc}}{\text{Real}}$ — ratio of accidental to real coincidence rates (not under the real coincidence peak but for all accidentals within 20 ns resolution time),

Losses — losses of events due to dead time of the trigger logic and DAQ,

$N_{A_{2\pi}}$ — number of produced $A_{2\pi}$ in the setup momentum acceptance per week.

Table 11.1:

N_p 10^{11}/spill	N_{ch} 10^6/s	N_+/N_- 10^6/s	Tr.1 10^3/s	Tr.2 10^3/s	Tr.3 10^3/s	Tr.4 10^3/s	$\frac{\text{Acc}}{\text{Real}}$	Losses %	$N_{A_{2\pi}}$ 10^3/week
0.5	11	2.4/1.5	27	6.3	2.8	0.8	1.4	11	8
1.0	21	4.9/2.9	82	21	10	3.0	2.1	20	15
1.5	32	7.4/4.4	164	50	26	7.5	2.8	35	18

The rejection factors at every stage were estimated with event simulation. The Coulomb and strong correlation of pions as well as accidentals were taken into account.

To obtain the number of "atomic" pairs one has to multiply $N_{A_{2\pi}}$ by the breakup probability in the target of $P_{\rm br} = 0.34$ (see Table 5.2). The experimentally observable number of dimesoatoms may be obtained by taking into account the detector and data handling efficiency ε. We suppose here that $\varepsilon = 0.5$ and believe that all underestimated effects are included in this value.

In the calculations we neglected the particles produced in interactions of initial or secondary beams with setup elements (in walls of collimator and vacuum chamber, in exit membrane and so on). The contribution of particles coming from these interactions was estimated with GEANT. Due to these background interactions the counting rates of drift chambers and scintillation hodoscopes increase by a factor 2. The majority of such background particles are electrons and positrons, which are vetoed by the trigger. Accidental coincidences of these electrons with the trigger will cause losses of dimesoatoms of $\sim$10%. The flux of positive and negative charged hadrons increase by 1.1 and 1.3, correspondingly. These hadrons form only accidental first level triggers and the number of second and higher level triggers will not change significantly as the most of background particles are produced downstream of the ionization and fibre detectors.

Taking into account particles produced in the setup elements, one should correct Table 11.1: N_+ and N_- must be doubled, the counting rate of the first level trigger should be increased by 1.2 for $0.5 \cdot 10^{11}$ initial protons flux and by about 1.3 for other proton fluxes; hence, $A_{2\pi}$ losses could increase up to 20%, 30% and 45% corresponding to the beam intensities shown in Table 11.1. The last numbers may be overestimated so in further calculations we use the values from Table 11.1.

At present we assume an intensity of $1.0 \cdot 10^{11}$/spill. The ratio of accidental events within 20 ns resolution time to real events R=$\frac{\rm Acc}{\rm Real}$ is 2.1. As mentioned above, this rather large amount of accidentals is necessary to get a good description of the free pion pair distribution.

To measure the $A_{2\pi}$ lifetime with 10% accuracy one must produce $N_0 = 5.6 \cdot 10^4$ dimesoatoms (see Table 5.2). Hence from Table 11.1 with $N_p = 1.0 \cdot 10^{11}$/spill of 0.35 s the runtime T to accumulate the requested statistics is:

$$T = N_0/(N_{A_{2\pi}} \cdot \varepsilon) = 5.6 \cdot 10^4/(15 \cdot 10^3 \cdot 0.5) = 7 \text{ weeks}.$$

We estimate that one event corresponds to a data volume of 0.5 Kbyte. This leads to the total volume of information equal to 150 Gbytes.

As mentioned in Section 6.2 the beam extraction system could allow a spill duration of 0.45 s. That would decrease the runtime to 5.5 weeks (at the same beam intensity per second). Moreover, it may be possible to run with two spills per supercycle instead of only one as used in the calculations. Then the runtime T would be reduced to 3 weeks.

If both factors are realized then the subtraction method of lifetime measurement, described in Appendix C, becomes feasible; the runtime for this method would be 20 weeks for the Ni target. In this case, the $A_{2\pi}$ lifetime could be measured by the two methods independently and simultaneously.

The runing time of the proposed experiment should be divided into three phases:

1. Detector tests and setup tuning, including test runs for calibrations and a short data acquisition period to prove the correctness of the method.

2. Detection of dimesoatoms and the measurement of $A_{2\pi}$ lifetime with a precision of 20%, using the extrapolation method.

3. Measurement of $A_{2\pi}$ lifetime with a precision of 10% using the extrapolation method or the subtraction one depending on the results obtained after completion of phase 2.

For the first phase three runs, each of one month duration, should be foreseen. We suppose that all detectors will be tested before the installation. The beam time is needed for testing of overall setup, for the measurements of its performances and for calibration purposes.

In the second phase, we plan to measure the $A_{2\pi}$ lifetime with Ti and Mo targets with an accuracy, for each target measurement, of 20%. These targets allow to measure the lifetime when the $A_{2\pi}$ interaction cross sections with matter and the target thicknesses are significantly different (the difference is about 4 times, see Table 5.2). To check the precision of the extrapolation procedure and the accuracy of $A_{2\pi}$ breakup probability calculations, two runs will be needed with Be and Pt targets. The total beam time of the second phase is 8 weeks.

The measurement of the $A_{2\pi}$ lifetime with 10% precision and corresponding calibrations will be performed with Ti, Mo, Be and Pt targets. The beam time needed for these measurements is 32 weeks.

If beam conditions will be favorable (two spills of 0.45 sec duration per supercycle), then the $A_{2\pi}$ lifetime could be measured with both extrapolation and subtraction methods. In this case the beam time for the third phase will be 35 weeks.

Chapter 12

Data processing and analysis

12.1 Data processing

We plan to write different program codes for processing and analysing the data. The first step in processing raw data, as given by the setup detectors read-out, is to perform the following tasks:

1. read raw data from detector electronics and write them to "raw data tapes" RDT;
2. find track candidates in DCs from hit wire numbers;
3. select "in time" and "in space" tracks by linear extrapolation of candidates at the level of hodoscope counters, and connecting hits in the $X - W$ and $Y - W$ planes respectively;
4. compute the first approximation parameters of tracks from drift times;
5. follow selected tracks (assuming they come from the target) through the magnetic field (a map will be needed) till the $SciFi$ detector (see section 7.1);
6. check the presence of the corresponding hits in the $SciFi$ detector.

At the level of points 5 and 6 the momentum is not yet precisely determined, so iterative process may be wanted to

7. improve the determination of track parameters using an "optimum" i.e. "best" linear approximation method fit and taking into account multiple scattering for errors propagation;
8. calculate precisely the track momenta.

If possible, tasks 2 to 8 will be performed on-line (partially at least). Then, the resulting values of on-line computed parameters will be written to tape (DST) together with raw data. If or when it is not possible to handle on-line processing, only pure raw data tapes will be produced at that stage and real DSTs writing will be postponed to later off-line processing.

From the experience acquired at Protvino during the previous experiment, we estimate at 54 ms (on any 1.2 Mips workstation) the time per event needed for performing tasks 2 to 8. The code size is estimated to 1.2 Mbytes.

12.2 Data analysis

The later stage of the analysis is intended to be performed off-line. It will consist of

9. splitting recorded pairs into real $\pi^+\pi^-$ pairs sample on one hand, and accidental pair sample on the other hand.

Then:

10. identify the particle corresponding to each track within a given pair;
11. compute the momentum of each track in the pair, relative momentum and other related quantities;
12. determine the lifetime of the $A_{2\pi}$ atoms.

We estimate to at least 5 ms the processing time per event.

12.3 Programming requirements

The programmers and/or physicists of the participating institutions will be requested to provide and to use program codes written in Standard Fortran-77, using CERN libraries or, if needed, any "freeware" easily available sources. The use of non freeware libraries will be restricted to the use of NAGLIB [NAGLIB], if necessary. Moreover, emphasis will be made on portability and efficiency. We intend to use dynamical compilation when available. We intend to use CMZ format as the standard interface for the experiment.

12.4 Estimated amount of data

We expect to have 3000 events of 0.5 Kbytes per second; the duration of the spill is 0.35 s and the time elapsed between two consecutive spills is 14.4 s. These figures lead to a mean of about 36 Kbytes per sec. It is not yet clear if we use standard 38 Kbytes "3480" magnetic cartridges to record event data. If so, the total amount of data per cartridge being estimated to 200 Mbytes, we ought to write about 16 cartridges per full day i.e. 110 per week of running time. This amount of data is quite comparable to the mean current amount of data taken by any medium size experiment at CERN or elsewhere.

Chapter 13

Systematical errors and calibration measurements

13.1 Systematic errors

To estimate systematic errors S_τ in the measurement of the $A_{2\pi}$ ground state lifetime τ five sources of systematic errors were considered:

1. Particle misidentification;
2. Difference between real and measured positions of the detectors;
3. Uncertainty in determination of the detector resolution;
4. Influence of hadron correlation;
5. Difference of the form of "non-Coulomb" and accidental pair distributions.

The distributions of "real" and "accidental" pairs on relative momentum and its projections were simulated. The spectra and yields of the particles were simulated using FRITIOF (see Chapter 9). The number of simulated events corresponds to $7.2 \cdot 10^4$ dimesoatoms produced in the target at the 100% setup efficiency. These data were analysed using the extrapolation method (see Chapter 4) both with and without taking into account the errors in the setup parameters. The difference of the results was taken as an estimation of the systematic errors S_τ.

13.1.1 Particle misidentification

Using the extrapolation method we have to obtain the relation between "Coulomb" and "non-Coulomb" pairs. The experimental distribution on relative momentum q is fitted by a sum of simulated distributions of "Coulomb" and "non-Coulomb" pairs with one free parameter. The fitting function is used for the determination of the atomic pair number and the number of "Coulomb" pairs in the range $q < 2$ MeV/c. The later is proportional to the number of produced $A_{2\pi}$.

If there is an admixture of pairs consisting of misidentified particles (i.e. at least one particle in a pair is not a pion), then errors of the number of atomic pairs and produced dimesoatoms would arise as the distribution on relative momentum for these pairs differs from that of "non-Coulomb" pairs. This leads to an error of the $A_{2\pi}$ lifetime value.

The scale of the error depends on the number of misidentified pairs and on the magnitude of the distribution dissimilarity. In addition, the admixed pairs distort the lab

momentum spectrum of the "Coulomb" pairs and therefore the reconstructed spectrum of dimesoatoms which is used for calculating the $A_{2\pi}$ lifetime.

We take into consideration pairs containing misidentified electrons (positrons), $K^{\pm}$ mesons and protons.

The pairs consisting of e^+e^- are generated in the Dalitz decay of π^0 meson and γ-quantum conversion in the target and $SciFi$ detector. Other e^+e^- pairs could be rejected by geometric cuts. We assume that the efficiency of identification of an electron (positron) in the spectrometer arm is 99.5%. Then the simulation shows that the error induced on the dimesoatom lifetime is $S_\tau = 1\%$.

The admixture of K^+K^- and πK pairs is considered in the assumption that all K mesons are analysed as being π mesons. That induces an error $S_\tau = 0.25\%$.

The pion-proton events can not be observed in the true coincidence peak due to a different time of flight. Therefore πp pairs may present in "accidental" pairs only. They induce an error $S_\tau < 0.1\%$.

So the estimation of systematic error caused by an admixture of misidentified particles is not larger then 1.4%.

13.1.2 Difference between real and measured positions of the detectors

This difference gives rise to errors in the particle momenta and in the opening angle of the pairs. Therefore the relative momentum q would be calculated erroneously, too. This leads to a different location of the "Coulomb" peak (together with the peak of atomic pairs) and (or) to different width of the "Coulomb" peak. This problem concerns mainly the $SciFi$ detector and the drift chambers (DC).

We assume that the accuracy of the detector locations will be 0.2 mm . Such an error in distance between the target and $SciFi$ detector induces an error in the transverse component of the relative momentum Q_t equal to 0.01%. This leads to a systematic error $S_\tau < 0.04\%$.

An error in the X coordinate of $SciFi$ induces an error in the momentum because the X coordinate of a track in the $SciFi$ plane is used as a base point for procedure of the momentum calculation. The parameters of a track measured in the drift chambers are the main data for momentum reconstruction. Hence a difference between the real and measured positions of DC leads to an error of the particle momentum. If this difference equals 0.2 mm then the relative error of momentum is $\delta p = 0.2 \div 1.0\%$.

In Section 13.2 the influence of shifts of the drift chambers and fibre detector by 0.2 mm in the X and Z coordinates is considered. One has shown that this systematic error of $A_{2\pi}$ lifetime could be reduced to 2% using "Coulomb" peak for calibration.

When momenta of both sign particles are symmetrically increased or decreased the calibration with a resonance mass will be used (see Section 13.3.4).

A difference between the real and measured positions of the detectors in the Y coordinate does not distort the result directly but this causes a decrease of the rejection factor for background particles.

These systematic errors will not be larger than 2%.

13.1.3 Uncertainty in determination of the detector resolution

Here we consider the case in which average values of the momenta and the coordinates are measured accurately but there are errors in resolution for these parameters. These errors lead to a change in the form of the fitting function like in the case discussed above (Section 13.1.1). An error in the momentum resolution of 1% leads to an error $S_\tau = 1.4\%$. The same errors in the resolution on the X or Y coordinates, measured by $SciFi$, induce the error $S_\tau = 1.3\%$. Here the resolution on X and Y contains also errors due to multiple scattering in the target. If calibration with a resonance mass (see Section 13.3) allows us to measure the resolution for momentum and coordinates with an accuracy of 0.5% then the systematic error will not exceed 2%.

13.1.4 Influence of hadron correlations

The influence of hadron correlation on the form of $\pi^+\pi^-$ pair relative momentum distribution has been considered in Chapter 3.2. It may be described with the factor $F_c(q)$:

$$F_c(q) = 1 - \xi q\,.$$

For the description of such a distribution an additional coefficient $C(q)$ was included into the fitting function:

$$C(q) = 1 - aq\,,$$

here a is a free parameter. Distributions, both with and without the factor $F_c(q)$, were fit by a function with coefficient $C(q)$. For simulation ξ was taken as $1.5 \cdot 10^{-3}$ (MeV/c)$^{-1}$. The difference of the results corresponds to an error $S_\tau = 0.1\%$.

13.1.5 Difference of the form of "non-Coulomb" and accidental pair distributions

"Non-Coulomb" pairs have a momentum distribution different from "Coulomb" pairs. This fact causes indirectly differences in the distribution of the "non-Coulomb" and accidental pairs as these last pairs contain pions from both short-lived and long-lived sources. To estimate the related systematic errors, "Coulomb" and "non-Coulomb" pairs distributions were simulated using accidental pairs, the relation between two types of pairs being found with Lund. Then two kinds of fit were applied to these distributions. The first fit function takes into account the dependence of "Coulomb"/"non-Coulomb" ratio on the lab momentum. The second fit uses the accidental pair distribution only. The difference of the results corresponds to an error of $S_\tau = 0.3\%$.

13.1.6 Summary

If we take for the global systematic error of the dimesoatom lifetime measurement with the extrapolation method the arithmetical sum of errors due to different sources, we find it is less than 5.8%.

For the subtraction method the sources of systematic errors are only a distortion of the momentum spectrum by misidentified particles and an erroneous measurement of the target thicknesses. The sum of these errors does not exceed 1%.

13.2 Calibration with the "Coulomb" peak.

The setup performance should be tested experimentally by the detection of well-known processes. In these tests the setup ability to identify the process has to be confirmed and some characteristics to be measured (the effective mass resolution, for example). With this aim we considered some processes that could be applied for the setup calibration procedure.

This method of calibration is used for correction of errors arising from inaccuracy in measuring of the angles of the spectrometer arms. The Coulomb interaction in the final state of the $\pi^+\pi^-$ pairs leads to an enhancement of the production cross section of pairs with small relative momentum. Therefore the distribution of $\pi^+\pi^-$ pairs on the difference of particle momenta contains a peak at $p_1 = p_2$ where p_1 (p_2) is the momentum of π^+ (π^-).

Consider a distribution of $\pi^+\pi^-$ over $\Delta\Theta_x = \Theta_{x1} + \Theta_{x2}$, here Θ_{x1} (Θ_{x2}) is the angle of the positive (negative) charged particle in DC with the setup axis. As $p \sim 1/\Theta_x$, this distribution contains the "Coulomb" peak, too. The peak position points to the value of $\Delta\Theta_x$ which corresponds to equal momenta $p_1 = p_2$. If the position of the detectors is measured exactly then the peak is located at $\Delta\Theta_x = 0$ as the magnet deflects the particles of opposite signs in opposite directions. But if Θ_{x1} and Θ_{x2} affected by systematical errors α_1 and α_2 due to mis-alignment, the peak will be located at $\Delta\Theta_x = \alpha_1 + \alpha_2$. This error can be corrected with the subtraction of a correction angle $\Theta_{\rm cor} = \Delta\Theta_x/2$ from Θ_{x1} and Θ_{x2}. This method is effective only for asymmetric errors in Θ_{x1} and Θ_{x2}.

To test this method, a large statistics sample of proton-target interactions corresponding to $72 \cdot 10^3$ generated $A_{2\pi}$ was simulated. These data have been handled and analyzed with the extrapolation method.

Three different situation have been examined:

(a) The position of the detectors is known exactly.

(b) There are errors in DC positions equal to 0.2 mm in projections X and Z. The real positions of the first three planes of one arm are shifted from the setup axis in X and towards the target in Z and the real positions of the last three planes are shifted oppositely. In the other arm the displacements of all planes are opposite to those of the first arm. Shifts of the $SciFi$ detector are the same as for the last plane of the 1st arm. In this case the errors of track parameters are maximal. Practically it leads to a rotation of the arms. Correction is not applied.

(c) The errors are the same as in (b) but the correction is applied.

The ratio of the "real" pair distribution over $\Delta\Theta_x$ to that of "accidental" pairs (needed to exclude the influence of a detection efficiency on the distribution shape) is shown in Figure 13.1 for these three cases. The distributions contain the events selected by applying a cut $Q_t < 2.25$ MeV/c to increase of the "Coulomb" peak magnitude. The effective

Table 13.1:

error	$\Theta_{\rm cor}$ mrad	$\langle\Delta\Theta_x\rangle$ mrad	$N_{\rm pair}$
no	0.	$0.6510 \cdot 10^{-2}$	$15540. \pm 490.$
yes	0.	-0.7578	5990 ± 490
yes	0.90	-0.1096	15050 ± 490
yes	0.95	$-0.8633 \cdot 10^{-1}$	15350 ± 490
yes	1.00	$-0.4241 \cdot 10^{-1}$	15980 ± 490
yes	1.05	$-0.7082 \cdot 10^{-2}$	15670 ± 490
yes	1.10	$0.3165 \cdot 10^{-1}$	14460 ± 490
yes	1.15	$0.7500 \cdot 10^{-1}$	15320 ± 480
yes	1.20	0.1027	14800 ± 490

number ($N_{\rm eff}$) of events in the distributions allows one to measure a mean value of the $\langle\Delta\Theta_x\rangle$ with an accuracy 0.05 mrad. Dependence of the number of atomic pairs $N_{\rm pair}$ on the value of correction angle $\Theta_{\rm cor}$ is given in the Table 13.1. Real correction angle corresponds to $\langle\Delta\Theta_x\rangle$ close to zero. Here $\Theta_{\rm cor} = 1.05$ mrad.

It is seen that after correction, the difference of $N_{\rm pair}$ from the number of atomic pairs calculated without errors is not more than 20% of the statistical error and corresponds to 2% accuracy in the $A_{2\pi}$ lifetime.

13.3 Calibration with particle decays

13.3.1 The simulation program

In order to reproduce the experimental setup, the simulation program, DIRAC, based on GEANT [BRUN87] has been developed. Results on the setup calibration with the help of K^0_S and K^+ mesons and Λ^0 hyperon decay are now presented.

The program simulates the transport of secondary particles through the setup, mimics the detector "responses", carries out the event reconstruction and fills up the histograms of different statistical distributions.

The detector sizes and characteristics, their location as well as information on materials needed for the program performance are taken from Chapter 7. Only the coordinate measurements were considered in the calculation. Precision of the drift chambers as well as that of the coordinate detector in the channel are supposed to be 150 μm and their efficiency 100%. The magnetic field was chosen to be homogeneous with B=1.65 T.

The following physical processes were considered in the simulation:

— multiple scattering in the channel coordinate detector, in the aluminium foil of the vacuum chamber window, in mylar and wires of the drift chambers and in air space of the setup;

— decays of nonstable particles according to with their lifetimes and branching ratios;

— ionization losses of particles;

— hadron and electromagnetic interaction of particles.

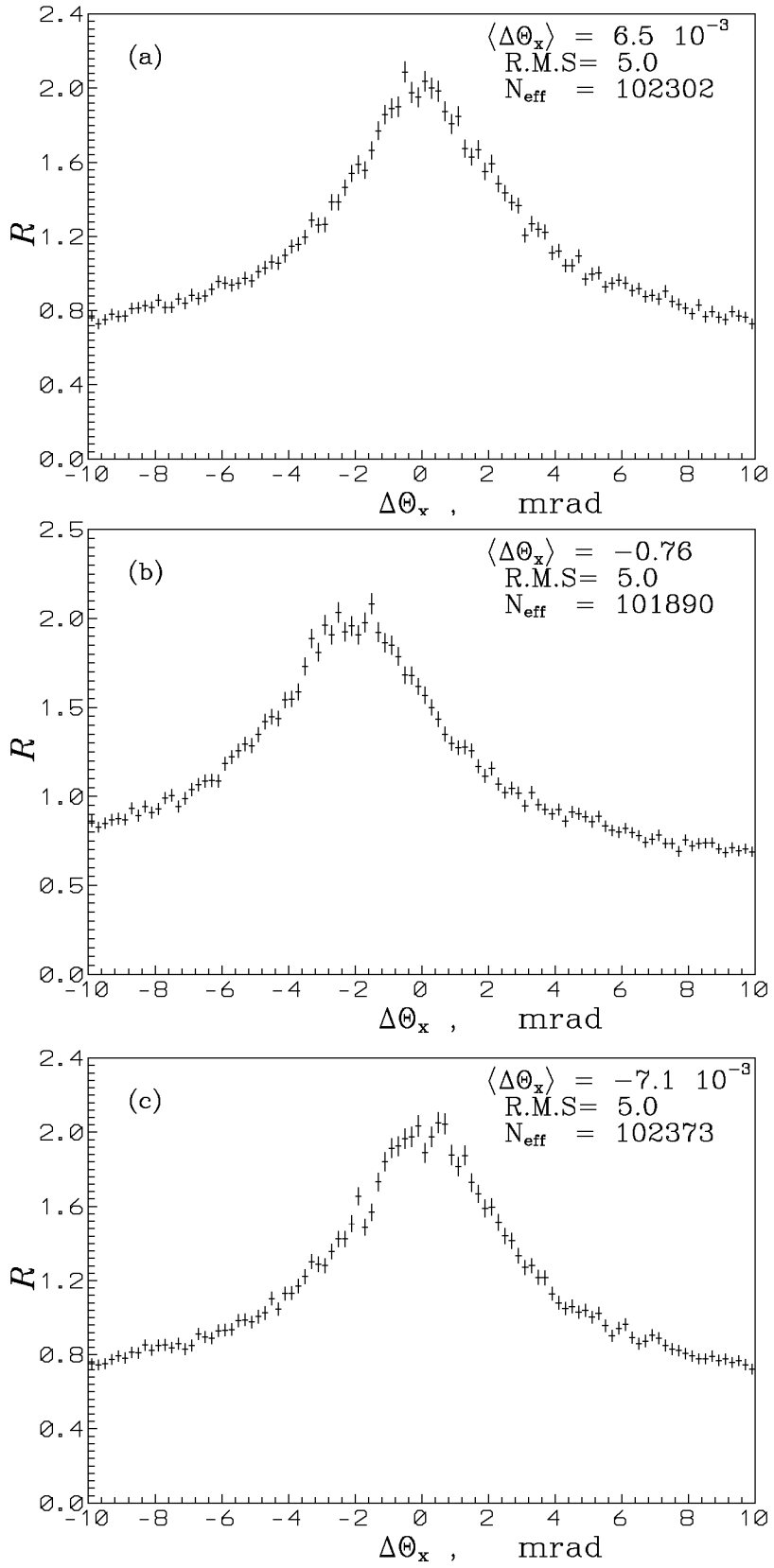

Figure 13.1: The ratio of the distribution of "real" pairs over $\Delta\Theta_x$ to that of "accidental" pairs: (a) for exact positions of detectors; (b) for positions of detectors measured with errors; (c) after correction, $\Theta_{\rm cor} = 1.05$ mrad.

The simulation has been performed within the momentum range of initial particles 4 GeV/$c \leq P \leq$ 7 GeV/c for Λ^0 and 6 GeV/$c \leq P \leq$ 10 GeV/c for K_S^0.

The procedure of event detection in the program, i.e. $K_S^0 \to \pi^+\pi^-$ or $\Lambda^0 \to p\pi^-$ decays, included track and momentum reconstruction of secondary particles. An event was detected only in the case of tracks found simultaneously in both arms of the spectrometer and of two particle passing through the detector in the channel.

Reconstruction of straight Y projections of tracks was performed by taking into consideration the measurements by 6 planes of drift chambers of the corresponding arm and by the coordinate detector in the channel. Reconstruction of the X projection of tracks took place in two stages. In the first stage, a straight track downstream of the magnet was considered if it passed through one of planes of the first drift chamber and through at least two other planes. On the second stage the complete track and momentum of the corresponding particle in horizontal plane were reconstructed on the base of point and angle of straight track coming out of the magnet and of the X coordinate in the channel coordinate detector.

13.3.2 Calibration with K_S^0 and Λ^0 decays

To imitate a pion pairs from dimesoatom breakup the particles with small lifetimes and decaying into $\pi^+\pi^-$ pair with high probability are suitable candidates. The particles decaying, e.g., into $p\pi^-$ (Λ^0) could also be considered as well as $K^- \to \pi^+\pi^-\pi^-$.

The calibration based on the two-particle decays $K_S^0 \to \pi^+\pi^-$ and $\Lambda^0 \to p\pi^-$ is considered below.

The typical results on momentum reconstruction of decaying particle (Λ^0) and effective mass distribution of detected $p\pi^-$ are presented in Figure 13.2. It shows no systematic error in Λ^0 mass reconstruction. As example, for an initial particle momentum of 5 GeV/c, we get $M_{\Lambda^0} = 1.1160 \pm 0.0009$ GeV/c^2.

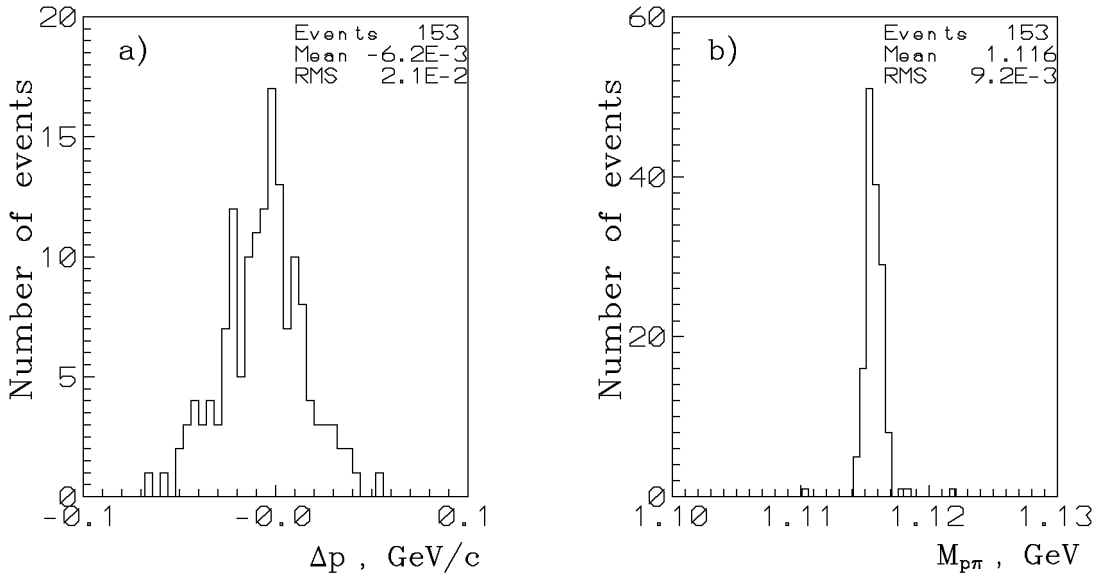

Figure 13.2: Simulation of the decay $\Lambda^0 \to p\pi^-$ in the channel at $p_\Lambda = 5$ GeV/c: a) deviation of the reconstructed momentum from the input simulation value; b) effective mass spectrum for the $p\pi^-$ pair.

The probability to detect $\pi^+\pi^-$ pairs from the K^0_S decay and $p\pi^-$ pairs from the Λ^0 decay versus initial particle momenta are shown in Figure 13.3a and 13.3b. The number of initial particles uniformly simulated in the solid angle restricted by sensitive area of the channel coordinate detector was, in both cases, equal to 10000. The probability to detect $\pi^+\pi^-$ and $p\pi^-$ is calculated taking into account the branching ratios. It is of the order of 0.02% to 0.8% for K^0_S and of 1% to 1.4% for Λ^0.

The results of the simulation show also, that the precision of the Λ^0 momentum reconstruction is limited to $0.0042 < \Delta P/P < 0.0046$ and that the average accuracy of effective mass reconstruction is $\sim$1 MeV. Analogous value for K^0_S are found to be 3.5 MeV.

13.3.3 Calibration with $K^+ \to \pi^+\pi^+\pi^-$ decays

Calibration with K^+ decay is attractive. In this case, it is possible to reconstruct the vertex, being the intersection point of K^+ meson track with the plane formed by any two tracks downstream of the magnet.

The probability to detect $\pi^+\pi^+\pi^-$ versus the K^+ initial momentum, taking into account branching ratio, is shown in Figure 13.3c. The direction of initial particles was uniformly simulated in the same solid angle as in case of Λ^0 and K^0_S.

13.3.4 Use of $\Lambda^0 \to p\pi^-$ decay for the telescope position tuning

The Λ^0 mass reconstruction shown in Figure 13.2 was obtained supposing that the positions of the detectors are strictly known. In fact, the value of the reconstructed mass may be shifted due to uncertainties in the values of the telescope angles with respect to the setup symmetry axis. The asymmetric errors on angles may be corrected with the "Coulomb" peak calibration described in Section 13.2. To exclude symmetric errors on angles, the Λ^0 decay process may be used.

To test the influence of symmetric errors in the telescope angles on the Λ^0 mass value the simulation has been done. Each telescope was turned by 1 mrad additionally, but the coordinates of DC wires were considered as if they had "normal" positions. Figure 13.4 shows the Gauss approximation of effective mass spectra for $\Lambda^0 \to p\pi^-$ decay at 4 GeV/c for "normal" case and the case with angular errors. The distance between the centers of these distributions depends, in general, on the initial momentum, but in the interval $4 \leq P \leq 7$ GeV/c a good resolution of the peaks is observed. This gives the possibility to correct for symmetrical angle distortions of the telescope positions.

13.3.5 Resume

Taking into account the fact that the yield of the detected $p\pi^-$ from Λ^0 decay significantly overcomes the corresponding yield of $\pi^+\pi^-$ from K^0_S and that the relative precision of Λ^0 momentum reconstruction is higher, the use of Λ^0 for the setup calibration seems preferable, especially from the point of view of accelerator runtime costs. The fact, that the $p\pi^-$ detection takes place in a wider momentum range than for $\pi^+\pi^-$ pairs from K^0_S, is in favour of the Λ^0 choice, as it is closer to the pion pair range from dimesoatom breakup. Finally, the yield of Λ^0 itself from the target is sufficiently high.

The setup calibration based on three-particle decays such as $K^+ \to \pi^+\pi^+\pi^-$ is also possible. In this case the yield of detected events is comparable to the yield of $\pi^+\pi^-$ pairs

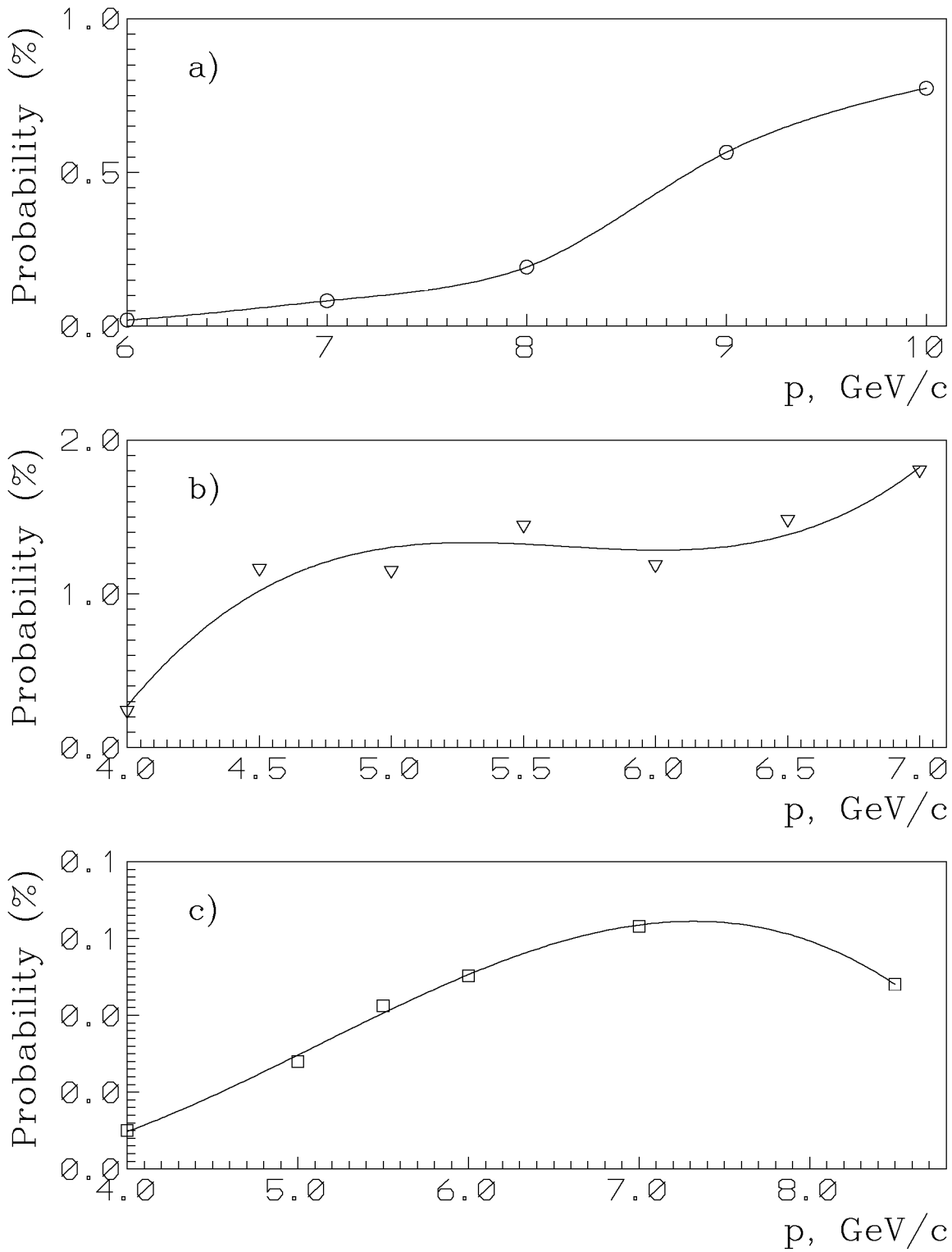

Figure 13.3: Probability to detect products of particle decays in the channel versus initial particle momenta: a) $\pi^+\pi^-$ pairs from K^0_S decay; b) $p\pi^-$ pairs from Λ^0 decay; c) $\pi^+\pi^+\pi^-$ from K^+ decay.

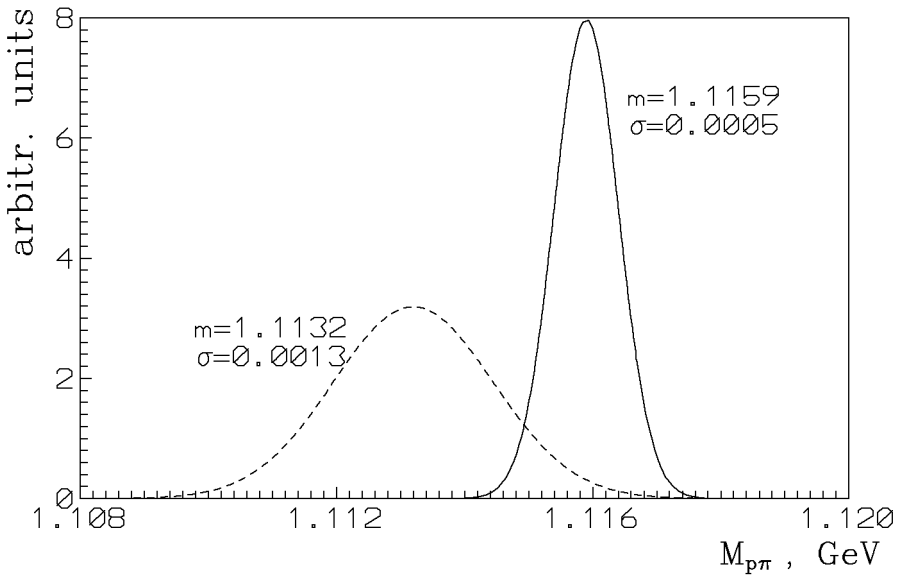

Figure 13.4: Effective mass distributions for $p\pi^-$ pairs from Λ^0 decay at 4 GeV/c: when the positions of the detectors are strictly known (full line curve) and when displacements of 1 mrad with respect to the symmetry axis of the experimental setup (dashed line curve).

from K^0_S.

To tune the telescope positions one has to use the $\Lambda^0 \to p\pi^-$ decay as well as the "Coulomb" peak calibration method.

13.4 Calibration with e^+e^- pairs

The pairs consisting of e^+e^- will be used for calibration of the scintillation hodoscopes and Cherenkov counters.

The time of flight of e^+ (e^-) does not depend on the momentum in the region of the setup acceptance. In addition e^+ and e^- can be strictly selected with the Cherenkov counters. Therefore the electron-positron pair distribution as a function of the time difference between hits on hodoscopes with positive and negative particles contains one peak of real coincidence in contrast to the analogous hadron distribution which has several peaks corresponding to $\pi^+\pi^-$, πK and πp pairs. For these reasons the electron-positron pairs are most suitable for the time calibration of the scintillation hodoscopes VH and HH .

The efficiency of Cherenkov counters to e^+ and e^- will be tested with shower detectors (see Chapter 7.5) or additional movable counters which are sensitive to electrons.

The e^+e^- pairs will be stored simultaneously with $\pi^+\pi^-$ data. It will allow to test the stability of detectors during the run.

Chapter 14

Other physics subjects

The proposed setup may be used to study other physical topics. Some of them could be investigated simultaneously with the $A_{2\pi}$ lifetime measurement, others need some modifications of the apparatus.

14.1 Observation of $A_{2\pi}$ long-lived states

As mentioned in Section 2.4 the measurement of the $A_{2\pi}$ lifetime and Lamb shift allows to obtain a_0 and a_2 separately in a model independent way. In order to measure ΔE_{ns-np}, the dependence of the lifetime for long-lived $A_{2\pi}$ states ($l \neq 0$) on the applied electric field can be studied [NEME85]. Calculations presented in Appendix B show that up to 10% of atoms generated in the thin target come out to the vacuum region as long-lived states. Such $A_{2\pi}$ atoms may be observed in the proposed setup without any change and the results of this experiment will help to prove the feasibility of ΔE_{ns-np} measurements.

14.2 Observation of $A_{\pi K}$ and measurement of its lifetime

CHPT, including the strange quark [SU(3)$_L$×SU(3)$_R$], can be tested by comparing the predicted values for πK-scattering lengths with model independent experimental values.

Pion-kaon scattering together with pion-pion scattering belong to the purest processes of pseudoscalar Goldstone bosons. In particular, the reaction $\pi K \to \pi K$ is important as it involves strangeness and unequal masses (mesons or quarks) in the simplest way.

Data about the πK-scattering lengths $b_{1/2}$ and $b_{3/2}$ (S-states, isotopic spin 1/2 and 3/2) may be obtained, in a model dependent way, from an analysis of single meson exchange in the reactions

$$KN \to \pi KN, \qquad KN \to \pi K\Delta^{++}\,. \tag{14.1}$$

Mean values for $b_{1/2}$ and $b_{3/2}$ from several experiments spread over wide intervals:

$$0.13 \leq b_{1/2} \leq 0.24, \qquad -0.05 \leq b_{3/2} \leq -0.013\,. \tag{14.2}$$

The observation of atoms consisting of π^+ and K^- mesons ($A_{\pi K}$) and the measurement of their lifetime allow to extract in a model independent way the difference $b_{1/2} - b_{3/2}$. (In the study of the corresponding antiatoms $A_{\pi^- K^+}$, the signal to background ratio is less favourable.) CHPT predicts the following values for these parameters [BERN91]:

$$b_{1/2} = 0.17 \qquad b_{3/2} = -0.05\,. \tag{14.3}$$

The relative errors are larger for b_i than for a_i because of the different parameter scale used in the expansion for the πK-scattering amplitudes. For $\pi\pi$-scattering this parameter is

$$\left(\frac{m_\pi}{4\pi F_\pi}\right)^2 = 0.014\,. \tag{14.4}$$

In the case of πK-scattering the analogous parameter is one order of magnitude larger:

$$\left(\frac{m_K}{4\pi F_\pi}\right)^2 = 0.18 \tag{14.5}$$

and, therefore, the precision of the theoretical calculations is smaller.

The probability for the $A_{\pi K}$ annihilation is mostly given by the process

$$\pi^+ + K^- \to \pi^0 + K^0 \tag{14.6}$$

and equals [BILE69] to

$$W_{n,0}(\pi^0 K^0) = \frac{1}{\tau_{n,0}} = \frac{8\pi}{9}\left(\frac{2\Delta m}{\mu}\right)^{1/2}(b_{1/2} - b_{3/2})^2 |\psi_{n,0}(0)|^2\,, \tag{14.7}$$

where $\Delta m = M_A - m_{\pi^0} - M_{K^0}$, M_A is the atom mass, μ is the reduced atom mass, and $\psi_{n,0}(0)$ is the corresponding wave function value at zero distance between the π and K mesons. As strong interaction does not change the value of $\psi_{n,0}(0)$ substantially [EFIM87]:

$$\psi_{1,0}(0) = \psi^c_{1,0}(0)(1 + 4 \cdot 10^{-4}), \tag{14.8}$$

the relations (2.18) and (2.19) obtained for $A_{2\pi}$ are valid for $A_{\pi K}$, too. So the measurement of the $A_{\pi K}$ annihilation probability from S-states allows to obtain in a model independent way a value for $\tau_{1,0}$ and, hence, for $b_{1/2} - b_{3/2}$.

Substituting the πK-scattering length values (14.3) and Coulomb value $|\psi^c_{1,0}(0)|^2$ into formula (14.7), one finds for the πK lifetime:

$$\tau_{1,0} = 5.8 \cdot 10^{-15}\text{s}. \tag{14.9}$$

The momenta of π and K arising from $A_{\pi K}$ ionization are bound by the relation:

$$\frac{p_\pi}{p_K} = \frac{m_\pi}{m_K}. \tag{14.10}$$

From this it follows that the setup geometry must be changed for $A_{\pi K}$ observation: the kaon spectrometer arm is tuned to higher momentum detection compared with the pion arm, and pion suppression in the kaon arm is necessary.

The yield of $A_{\pi K}$ is about 12 times less than that one for $A_{2\pi}$ [NEME85].

14.3 Study of charged particle production dynamics using the Coulomb correlation

As mentioned in [AFAN91A] a study of the Coulomb correlation in the $\pi^+\pi^-$ system enables to measure the relative parts of pion pairs, generated by short-lived or long-lived sources, at the percent level.

Excluding pions originating from K meson and hyperon decays with the coordinate detector in front of the magnet, one can determine a summed probability for η and η' mesons produced.

14.4 Bose-Einstein correlations

A study of Bose-Einstein correlations in the $\pi^-\pi^-$ system requires consideration of Coulomb corrections for those pion pairs, originating from short-lived soures. In previous experiments these corrections were not experimentally determined, but estimated by model (Lund) calculations. Exploiting the high relative momentum resolution of our spectrometer, it is possible to extract these corrections from the measurements ($\pi^-\pi^-$ and $\pi^+\pi^-$) themselves. Correlation functions for $\pi^-\pi^-$ pairs, calculated using the model [LEDN82] (see Section 3.2), are shown in Figure 14.1. The data for like sign particles are taken as a by-product during data acquisition runs.

14.5 Search for narrow resonances in $\pi^+\pi^-$ system

The high resolution in relative $\pi^+\pi^-$ c.m.s. momentum ($\sim$ 1 MeV/c) and the large amount of pion pairs recorded allow to undertake a search for narrow pion resonances in the mass interval $2m_\pi \leq M_{\pi\pi} \leq 2m_\pi + 60$ MeV.

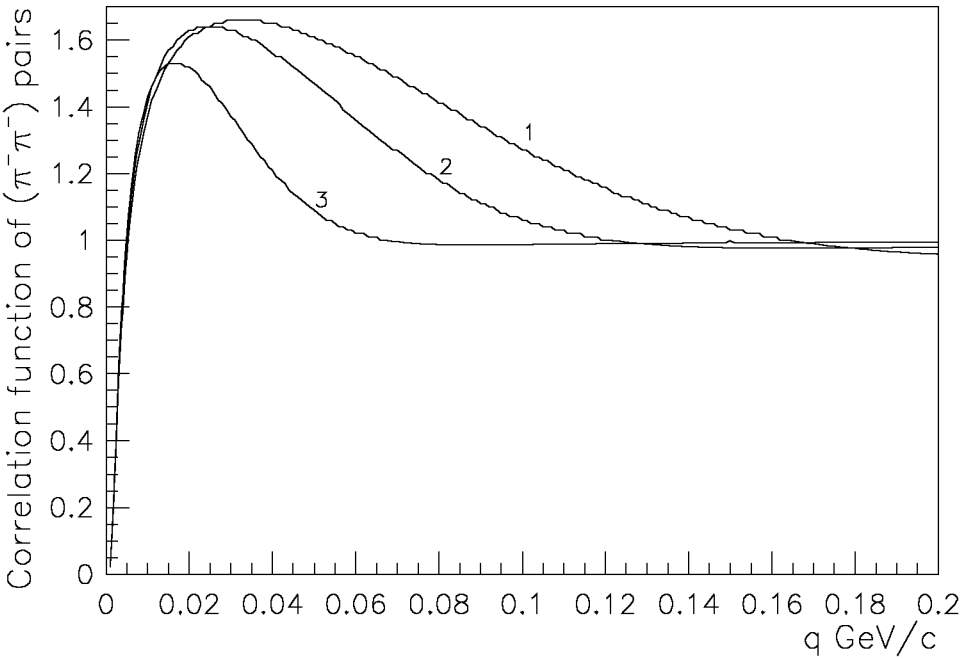

Figure 14.1: Correlation function of $\pi^-\pi^-$ versus relative momentum q in the pair c.m.s. Calculations have been performed using the model [LEDN82] for the following kinematic variables and the model parameters: $q_T = 0$, velocity of pair in the rest frame of pion sources $v = 0.7c$ and particle emission time $\tau_0 = 1.0$ fm/c. Curves 1, 2 and 3 are obtained for the space parameter of pion source region r_0 of 1.2 fm, 2.0 fm and 4.0 fm, respectively. The decrease of correlation function to zero at the origin occurs due to the Coulomb repulsion of likely charged particles.

Chapter 15

Cost estimation and time scale of the experiment

15.1 Cost estimation

The total cost of the setup is estimated to be about 2.6 MCHF. Request to CERN amounts to about 900 kCHF including about 500 kCHF for shielding and iron absorber.

We estimate the cost of the equipment as follows:

I	Detectors with readout electronics.	
	1. Scintillation fibre detector	300 kCHF
	2. Forward scintillation hodoscope	55 kCHF
	3. Microstrip gas chamber	60 kCHF
	4. Drift chamber system	720 kCHF
	5. Horizontal hodoscopes	135 kCHF
	6. Vertical hodoscopes	235 kCHF
	7. Cherenkov counters	120 kCHF
	8. Preshowers	110 kCHF
	9. Muon detectors	115 kCHF
	Subtotal	1850 kCHF
II	Data acquisition system and computers	375 kCHF
III	Trigger system	270 kCHF
IV	Auxiliary electronics	50 kCHF
V	Secondary particle channel	80 kCHF
	Subtotal	775 kCHF

1. Proton beam line ZT7:	
(a) experimental area and beam line[1]	375 kCHF
(b) iron for the beam catcher[1]	300 kCHF
(c) proton beam diagnostics	40 kCHF
2. Secondary channel shielding (40 tons of lead) and muon absorber (40 tons of iron)	210 kCHF
Subtotal	925 kCHF

15.2 Time scale of the experiment

After approval of the proposal, we estimate that the construction of the detectors will take 2 years. Installation on the floor can be done within 6 months.

The setup test and calibration (phase 1) will require 3 months of beam time spread over 10 months.

The measurement of τ at 20% level should be achieved within 8 weeks of beam time and about 3 months for data processing (phase 2).

The final measurement of τ at 10% level will last about two years, including 16 to 35 weeks of beam time, depending on the available beam conditions and on the method to be applied.

[1]This estimation have been done by R.Coccoli and L.Danloy, see PS/PA Note Installation 93-10. Rev.1.3.12.93)

Acknowledgements

We thank J.Gasser and H.Leutwyler for their invaluable support in writing the theoretical part of our proposal. For the calculation of electromagnetic corrections to the relation between the atom lifetime and pion scattering lengths we are grateful to U.Moor and G.Rashe. We also thank R.Lednicki for his help in the analysis of correlations and B.Erazmus for useful discussions of this problem. Furthermore, we would like to thank L.Okun, K.Pretzl and L.Tauscher for many helpful discussions and their support in preparing the proposal. For numerous interesting discussions about status and possible trends of the underlaying theory we are grateful to M.Knecht and J.Stern. The great help in planning the beam layout and the profound technical expertise of the CERN staff, especially of V.Agoritsas, R.Coccoli, L.Danloy, M.Doser, L.Durieu, Y.Perrin, D.Simon and J.Tuyn, are warmly acknowledged. Discussions and consultations with F.Aeschiman, A.Braem, C.Flament, W.Flegel, J.Y.Hemery, W.Klempt, G.Martini, J.P.Merlo, P.Simon and M.Zahnd were very helpful.

Appendix A

Description of $A_{2\pi}$ passing through a target

Let us consider details of the probability calculation of the $A_{2\pi}$ breakup inside a target. Using the calculated total and excitation cross sections we can describe an evolution of atomic state populations during the $A_{2\pi}$ passage through a target. To calculate the transition cross sections (5.1) we have used form factors $F_i^f(q)$ of $A_{2\pi}$ obtained in the frame with the quantization axis along the atom momentum. This axis stays preserved in all subsequent collisions as the atom momentum is much greater then the transfered one. Therefore the evolution of the atomic state populations is described in a simple way.

Let us write a set of differential equations for the probability of different $A_{2\pi}$ state populations. Such a set of equations is usually named microscopic description of atomic state populations or classical set of kinetic equations.

$$\frac{dp_i(s)}{ds} = \sum_{j=1}^{\infty} a_{ij} p_j(s) \tag{A.1}$$

Here $p_i(s)$ is the probability of $A_{2\pi}$ state populations after passing the distance s in the matter. With the chosen quantization axis only atomic transitions that conserve Z-parity $P^Z = (-1)^{l-m}$ are permitted [TARA91], where l and m are the orbital and magnetic quantum numbers. The $A_{2\pi}$ atoms are produced in nS states, so they have positive Z-parity. Thus only states with positive Z-parity have nonzero populations and just these states are considered further. We simply renumber all "permitted" atom states and i and j are numbers of states. The a_{ij} denotes the matrix of inverse lengths of the transition from the state j to the state i. For $i \neq j$, a_{ij} is given by

$$a_{ij} = \frac{\sigma_j^i \rho N_0}{A}. \tag{A.2}$$

Here ρ and A are density and atom weight of the target, respectively, and N_0 is the Avogadro number. For $i = j$, the a_{ii} describes the total decrease of the state i:

$$a_{ii} = -\frac{\sigma_i^{tot} \rho N_0}{A} - \begin{cases} 2m_\pi / p_A c \tau_{n,0} & \text{for } n\text{S states} \\ 0 & \text{otherwise} \end{cases} \tag{A.3}$$

where m_π is the pion mass, p_A is the $A_{2\pi}$ momentum and $\tau_{n,0}$ is the lifetime of the nS states (2.19). The first term concerns with the population decrease due to interaction

with the target and the second one describes the annihilation probability from the nS states. Here and further we neglect any decrease of population of other states due to annihilation and of all states due to radiation because the lifetimes for these processes are much greater than the time of flight through the target [NEME85].

The initial condition for the set of equations (A.1) is given by the probability of $A_{2\pi}$ production with different quantum numbers (Section 3.1, p. 17).

The lifetime and momentum of $A_{2\pi}$ are parameters of the equation set (A.1). Its solution is reduced to calculation of eigenvalues and eigenvectors of matrix a_{ij} and then to decomposition of initial conditions on the set of eigenvectors.

Since $A_{2\pi}$ can get excited or deexcited at the interaction, the matrix a_{ij} does not show a triangular form like in the case of a chain of radiation decays which is described by the analogous set of equations. For this reason an exact solution for any state may only be obtained as a solution of the infinite set of equations. Hence we have to limit the set of equations in order to get a solution. The precision of the limited equation set solution is illustrated by Tables A.1 and A.2.

In Table A.1 the summed population probabilities P_n of states with principal quantum number n (summed over l and m) are shown. These results are the solutions of the limited equation set, including the states with principal quantum number up to $n_{\max}$. These calculations have been performed for conditions of the previous experiment at Protvino [AFAN93A, AFAN94]: the $A_{2\pi}$ mean momentum of 2.86 GeV/c and the tantalum target of 8 μm thickness. The $A_{2\pi}$ lifetime was assumed to be $3.7 \cdot 10^{-15}$ s which predicted by CHPT.

Table A.1:

	$P_n(n_{\max})$					
$n_{\max}$	1	2	3	4	5	6
1	$3.301 \cdot 10^{-1}$					
2	$3.337 \cdot 10^{-1}$	$4.848 \cdot 10^{-2}$				
3	$3.341 \cdot 10^{-1}$	$5.249 \cdot 10^{-2}$	$1.475 \cdot 10^{-2}$			
4	$3.342 \cdot 10^{-1}$	$5.333 \cdot 10^{-2}$	$1.703 \cdot 10^{-2}$	$6.334 \cdot 10^{-3}$		
5	$3.342 \cdot 10^{-1}$	$5.358 \cdot 10^{-2}$	$1.768 \cdot 10^{-2}$	$7.641 \cdot 10^{-3}$	$3.273 \cdot 10^{-3}$	
6	$3.343 \cdot 10^{-1}$	$5.367 \cdot 10^{-2}$	$1.791 \cdot 10^{-2}$	$8.094 \cdot 10^{-3}$	$4.068 \cdot 10^{-3}$	$1.906 \cdot 10^{-3}$
7	$3.343 \cdot 10^{-1}$	$5.370 \cdot 10^{-2}$	$1.801 \cdot 10^{-2}$	$8.280 \cdot 10^{-3}$	$4.381 \cdot 10^{-3}$	$2.414 \cdot 10^{-3}$

In Table A.2 the same data are presented in the form $\delta P_n(n_{\max}) = (P_n(n_{\max}) - P_n(n_{\max}-1))/P_n(n_{\max})$ to show the rapid convergence of P_n .

The transition cross sections obey the equality $\sigma_i^f = \sigma_f^i$ and so the matrix a_{ij} is symmetric. The same cross sections depend on the magnetic quantum numbers of initial and final states m_i and m_f as $|m_f - m_i|$. Moreover, the initial condition for the set of equations (A.1) includes the fact that only nS states (with $m = 0$) are not empty. It can be concluded that states with opposite sign magnetic quantum numbers have equal populations. This allows to exclude the states with negative magnetic quantum numbers from the equation set and thus to reduce dimension of the set. For example, the dimension of the matrix a_{ij} is reduced from 84 to 50 for $n_{\max} = 7$. However the resulting matrix a_{ij} becomes asymmetric.

We have solved the equation set for $n_{\max} = 7$, a limit which results from the precision of the routine used to solve the eigenvalue problem. Thus the populations of all states

Table A.2:

	$\delta P_n(n_{\max})$					
$n_{\max}$	1	2	3	4	5	6
2	$1.087\cdot10^{-2}$					
3	$1.195\cdot10^{-3}$	$7.636\cdot10^{-2}$				
4	$2.524\cdot10^{-4}$	$1.570\cdot10^{-2}$	$1.336\cdot10^{-1}$			
5	$7.449\cdot10^{-5}$	$4.613\cdot10^{-3}$	$3.683\cdot10^{-2}$	$1.711\cdot10^{-1}$		
6	$2.699\cdot10^{-5}$	$1.672\cdot10^{-3}$	$1.308\cdot10^{-2}$	$5.602\cdot10^{-2}$	$1.954\cdot10^{-1}$	
7	$1.123\cdot10^{-5}$	$6.959\cdot10^{-4}$	$5.402\cdot10^{-3}$	$2.246\cdot10^{-2}$	$7.127\cdot10^{-2}$	$2.104\cdot10^{-1}$

with $n \leq n_{\max}$ as a function of the path s in the target are known. This function takes into account the interaction of $A_{2\pi}$ with target atoms and the $A_{2\pi}$ annihilation. Points of $A_{2\pi}$ production are distributed uniformly over the target thickness. So we have to use the average values over this distribution for all discussed probabilities.

From Tables A.1 and A.2 one can conclude that the summed population of all discrete atomic states with $n \leq n_{\max}$ ($P_{\rm dsc}$) is known with precision much better than 1%. From Table A.1 one realizes that P_n has the asymptotical behaviour $an^{-3} + bn^{-5} + \ldots$. Using rows 5 and 6 we calculate the constants a and b and are able to estimate the total population of all other atomic states ("tail"), $P_{\rm tail}$, that are not included in the equation set. An uncertainty in this estimation has little influence on the final results because of the smallness of the "tail" (see Table 5.1).

The $A_{2\pi}$ atoms annihilate mainly from 1S state (2.17). The population of the first few states is known with high accuracy (Table A.2) and so the probability of $A_{2\pi}$ annihilation ($P_{\rm anh}$).

After having calculated the probabilities for $A_{2\pi}$ to remain in one of discrete states or to annihilate, while passing through the target, the remainder, that is probability of $A_{2\pi}$ breakup, $P_{\rm br}$, is given by

$$P_{\rm br} = 1 - P_{\rm dsc} - P_{\rm tail} - P_{\rm anh}\,. \tag{A.4}$$

In such a way we can calculate the probability of $A_{2\pi}$ breakup in any target for arbitrary values of the atom momentum and lifetime.

Appendix B

Populations of long-lived states 2P, 3P, ...

In Figure B.1 a summed population of all long-lived atomic states (with $l \neq 0$) after $A_{2\pi}$ passage though the target is shown as a function of the $A_{2\pi}$ ground state lifetime for different Ta target thicknesses. One can see that about 10% of produced atoms leave the target in long-lived states. This figure illustrates the feasibility of observation of such states discussed in Sections 2.4.3 and 14.1.

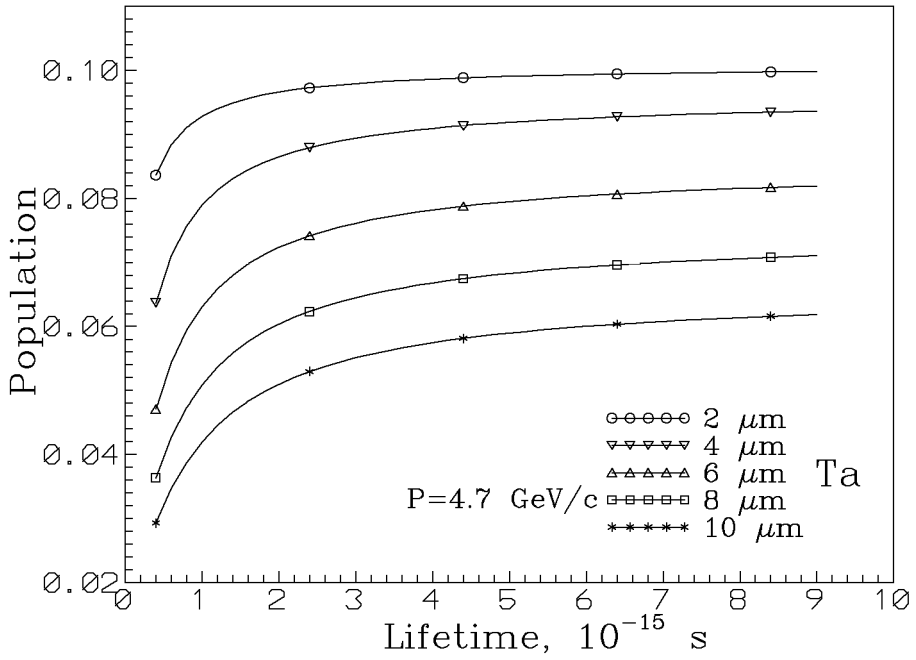

Figure B.1: Summed population of all long-lived atomic states (with $l \neq 0$) after $A_{2\pi}$ passage through the target as a function of the $A_{2\pi}$ ground state lifetime for different Ta targets.

Appendix C

Subtraction method for the lifetime measurement

C.1 Method description

For dimesoatom lifetime determination one can use the experimental information obtained by means of three targets T_1, T_2 and T_3 made of the same material. The target T_1 is one layer of a foil, e.g. of titanium of 175 μm thick. The target T_3 consists of k_3 layers of the same total thickness as T_1. The space between the layers is about 1 mm. In this case most $A_{2\pi}$ produced in any layer annihilate between this layer and the next one. The number k_3 of layers is found according to the following conditions:

1. Technological feasibility of manufacture of thin foils.
2. A large size of the multilayer target along the proton beam leads to erroneous determination of q_T and to different solid angles of the experimental setup for different target layers.

Possible values of k_3 are

$$20 \leq k_3 \leq 40\,. \tag{C.1}$$

The target T_2 consists of k_2 layers of the total thickness equal to that of the targets T_1 and T_3. The number of layers satisfies the condition

$$1 < k_2 < k_3\,. \tag{C.2}$$

Assume the experimental data are collected for the same number of interactions in each of the three targets. The distributions on the relative pair momentum q in the region $q < 2$ MeV/c will contain N_1, N_2 and N_3 pairs for the targets T_1, T_2 and T_3, respectively. These pair numbers can be represented as

$$\begin{aligned} N_1 &= n_{A\,1} + N_{f\,1} \\ N_2 &= n_{A\,2} + N_{f\,2} \\ N_3 &= n_{A\,3} + N_{f\,3}. \end{aligned} \tag{C.3}$$

Here $n_{a\,1}$, $n_{a\,2}$ and $n_{a\,3}$ are the numbers of the atomic pairs and $N_{f\,1}$, $N_{f\,2}$ and $N_{f\,3}$ are the numbers of free pairs. The number of the atomic pairs is determined by the probability of $A_{2\pi}$ ionization that is different for the three targets. As the total thicknesses of the targets T_1, T_2 and T_3 are the same there will be the same multiple scattering. Therefore

$$N_{f\,1} = N_{f\,2} = N_{f\,3}\,. \tag{C.4}$$

Let us consider the value

$$x \;=\; \frac{N_2 - N_3}{N_1 - N_3}. \tag{C.5}$$

Taking into account (C.4) we obtain

$$x \;=\; \frac{n_{A\,2} - n_{A\,3}}{n_{A\,1} - n_{A\,3}}\,. \tag{C.6}$$

The x value only depends on atomic pair numbers.

The calculations have shown that x is a simple function of the $A_{2\pi}$ lifetime ($x = f(\tau)$) for fixed pair momentum. Therefore the measurement of x value allows to determine the lifetime of the dimesoatom.

The number of layers of the target T_2 is determined by minimizing the errors

$$\sigma_\tau \;=\; \sigma_x/(dx/d\tau) \tag{C.7}$$

for the fixed number of interactions. The expression for the standard deviation is

$$\sigma_x \;=\; \frac{1}{N_1 - N_3}\,\sqrt{\sigma^2_{N_2} + x^2\sigma^2_{N_1} + (1-x)^2\sigma^2_{N_3}}\,. \tag{C.8}$$

C.2 Production and breakup of $A_{2\pi}$ in multilayer targets. Target choice for the subtraction method

The method to calculate the $A_{2\pi}$ breakup probability described above (Section 5.2) can easily be applied to multilayer targets suggested to measure the $A_{2\pi}$ lifetime by the subtraction method. To do so one should also take into account the probability of atom annihilation in gaps between the layers and the fact that atoms are produced in any layer.

In Figure C.1 the probability of $A_{2\pi}$ breakup is shown as a function of the gap width for different numbers of layers N_l of titanium targets with a total thickness of 175 μm. From this figure we have chosen the gap width of 500 μm for all further calculations.

In Figure C.2 the probability of $A_{2\pi}$ breakup is shown as a function of the $A_{2\pi}$ lifetime for different numbers of layers N_l of nickel targets with total thickness of 70 μm. Using these data one can evaluate the variable x. Taking into account (C.6) x can be written as

$$x \;=\; \frac{P_{\mathrm{br}\,2} - P_{\mathrm{br}\,3}}{P_{\mathrm{br}\,1} - P_{\mathrm{br}\,3}}\,. \tag{C.9}$$

The value x as a function of the $A_{2\pi}$ lifetime is shown in Figure C.3 for different numbers of layers k_2 in the second target and the fixed number of layers $k_3 = 100$ in the

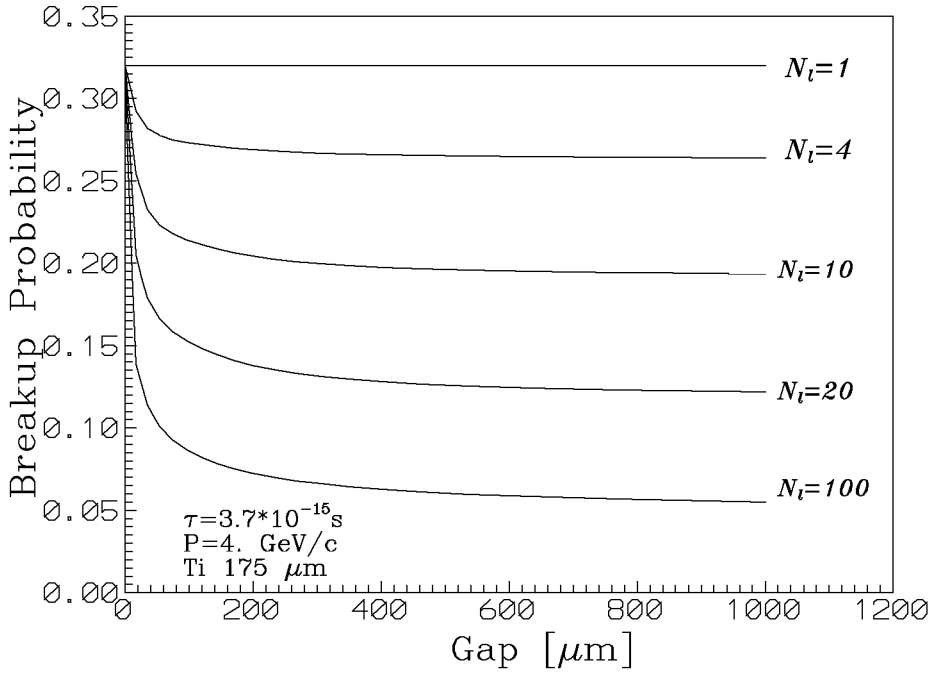

Figure C.1: The probability of $A_{2\pi}$ breakup in multilayer targets as a function of the gap width for different numbers of layers N_l of Ti targets with a total thickness of 175 μm.

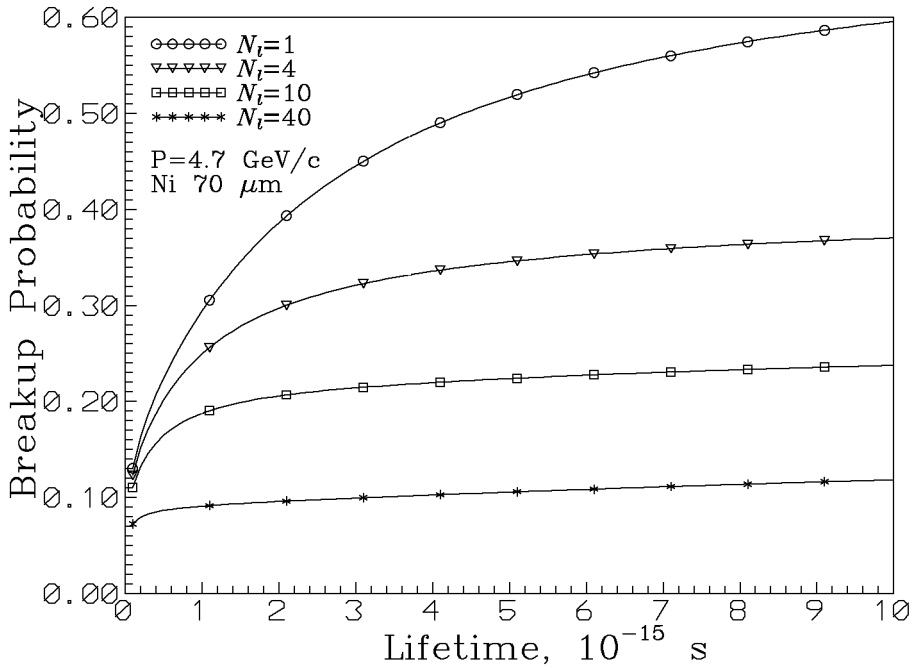

Figure C.2: The probability of $A_{2\pi}$ breakup in multilayer targets as a function of the $A_{2\pi}$ lifetime for different number of layers N_l of Ni targets with a total thickness of 70 μm.

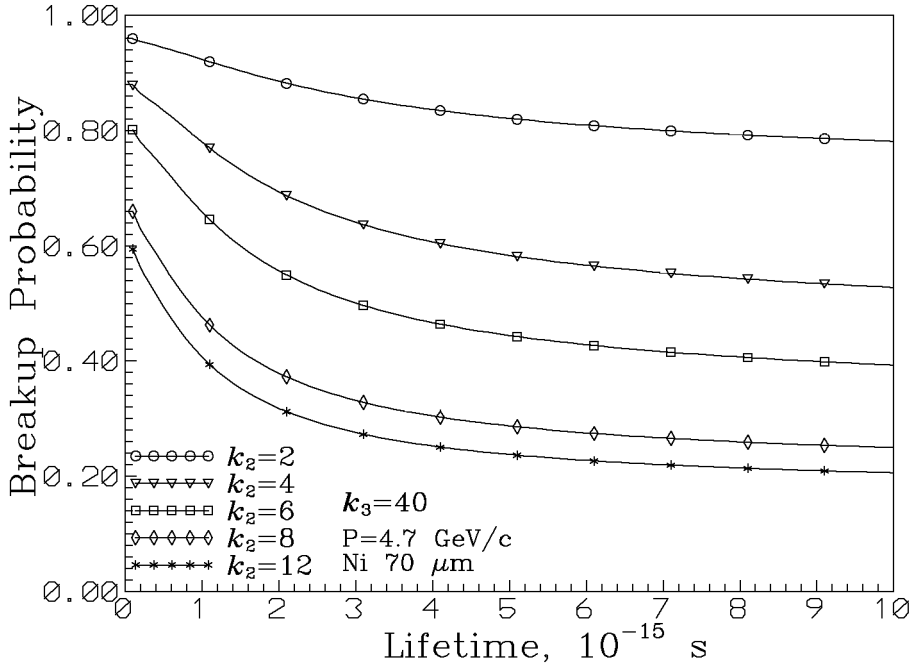

Figure C.3: The value x as a function of the $A_{2\pi}$ lifetime for different numbers of layers k_2 in the second target and the fixed number of layers $k_3 = 100$ in the third target for Ni targets with a total thickness of 70 μm.

third target. In Figure C.4 the same dependence is shown for $k_2 = 5$ and various numbers k_3.

Using equation (C.6) and the results of a simulation of the $A_{2\pi}$ detection, we can evaluate a number of $A_{2\pi}$, that has to be produced in targets to achieve the required precision in the lifetime measurement with the subtraction method. In Figure C.5 the number of $A_{2\pi}$, N_A, that has to be produced in all three targets to obtain the $A_{2\pi}$ lifetime within 10%, is shown as a function of target nucleus charge Z for different numbers of layers k_2 in the second target and the fixed number of layers $k_3 = 40$ in the third target. All targets have the total thicknesses equivalent in radiation length to 20 μm tantalum. Data are shown for the lifetime value predicted by CHPT: $3.7 \cdot 10^{-15}$ s and the $A_{2\pi}$ momentum of 4.7 GeV/c. In the calculation the ratio of accidental to real coincidences in the setup was 1.3. One can see that the smallest number of $A_{2\pi}$ is required for the nickel targets consisting of 5 layers in the second target and with a total thickness of 70 μm.

In Figure C.6 the dependence of N_A on the atom lifetime is shown for targets equivalent to 20 μm tantalum and fixed values of layer numbers $k_2 = 5$ and $k_3 = 40$. Like in the case of the extrapolation method, for a wide range of the $A_{2\pi}$ lifetime, there are target materials which require approximately the same minimal number of produced $A_{2\pi}$ to measure the lifetime within 10%.

Some numbers concerning the subtraction method are given in Table C.1. For various targets made of materials with nucleus charge Z, with the total thickness equivalent to 20 μm tantalum (Table 5.2) and consisting of numbers of layers in the second target $k_2 = 5$ and in the third one $k_3 = 40$, the following numbers are given: the probabilities of $A_{2\pi}$ breakup in all three targets $P_{\mathrm{br}1}$, $P_{\mathrm{br}2}$, $P_{\mathrm{br}3}$, the value of x, the relative precision δx in

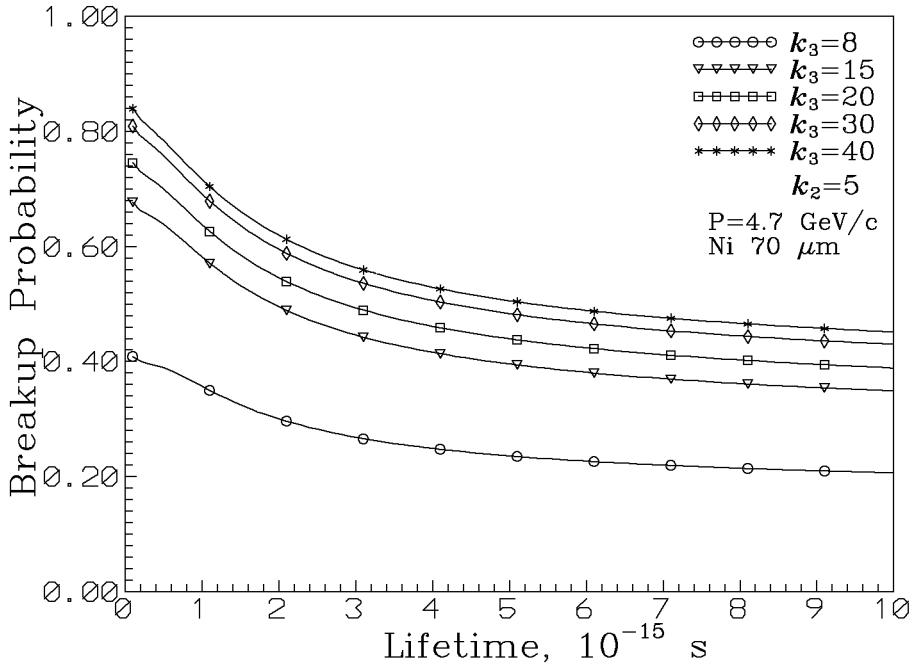

Figure C.4: The value x as a function of the $A_{2\pi}$ lifetime for the number of layers $k_2 = 5$ in the second target and various number of layers k_3 in the third target for the nickel targets with a total thickness of 70 μm.

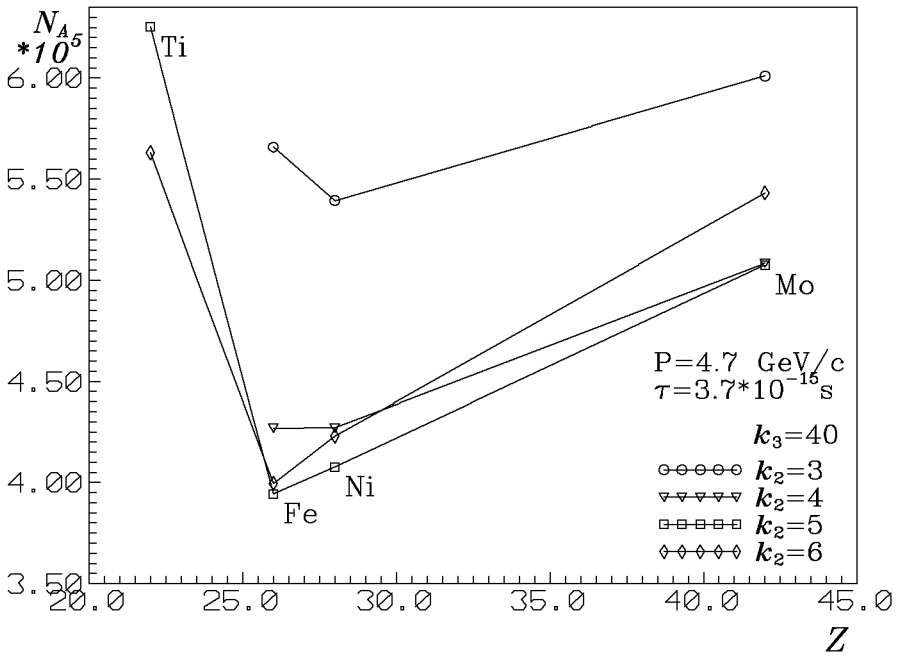

Figure C.5: The number of $A_{2\pi}$ that has to be produced in three targets to obtain the $A_{2\pi}$ lifetime within 10% as a function of target nucleus charge Z for targets equivalent to 20 μm Ta. Solid lines are drawn between points with equal numbers of layers k_2 in the second target. The number of layers in the third target is fixed to $k_3 = 40$.

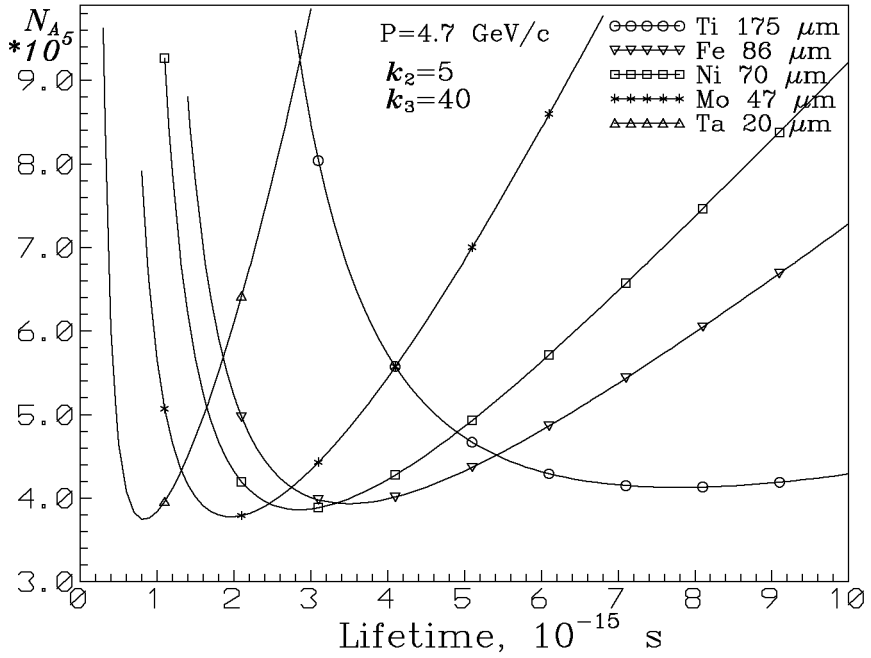

Figure C.6: The number of $A_{2\pi}$ that has to be produced in three targets to obtain the $A_{2\pi}$ lifetime within 10% as a function of lifetime for targets equivalent to 20 μm of tantalum. The numbers of layers in the second and third targets are fixed to $k_2 = 5$ and $k_3 = 40$.

the measurement of x and the number N_A of $A_{2\pi}$ produced in all three targets, required (both δx and N_A) to obtain the lifetime within 10%, and ratio $w_1 : w_2 : w_3$ between the numbers of produced $A_{2\pi}$ in each target, providing the smallest value of N_A. One can see that targets in the range from Fe to Cu require about the same number N_A and so they would be used for the lifetime mesurement by this method. Using targets with another total thickness requires the greater number N_A.

Comparing Tables 5.2 and C.1 one can conclude that the number of atoms produced in the first (one layer) targets is sufficient to obtain the lifetime by the extrapolation method within 10%. From an additional calculation one can see that the data recorded for the second target alone will allow to obtain the lifetime by the extrapolation method within 18%.

Table C.1:

	Z	$P_{\mathrm{br}\,1}$	$P_{\mathrm{br}\,2}$	$P_{\mathrm{br}\,3}$	x	δx	$w_1 : w_2 : w_3$	N_A
Al	13	0.234	0.202	0.096	0.771	$1.00 \cdot 10^{-2}$	0.390 : 0.500 : 0.110	$6.2 \cdot 10^6$
Ti	22	0.341	0.260	0.100	0.663	$2.17 \cdot 10^{-2}$	0.342 : 0.500 : 0.158	$6.3 \cdot 10^5$
Fe	26	0.444	0.294	0.101	0.563	$2.28 \cdot 10^{-2}$	0.297 : 0.501 : 0.202	$3.9 \cdot 10^5$
Ni	28	0.476	0.303	0.102	0.538	$2.16 \cdot 10^{-2}$	0.286 : 0.501 : 0.213	$4.1 \cdot 10^5$
Cu	29	0.475	0.303	0.102	0.539	$2.17 \cdot 10^{-2}$	0.286 : 0.501 : 0.213	$4.1 \cdot 10^5$
Mo	42	0.534	0.318	0.103	0.500	$1.82 \cdot 10^{-2}$	0.269 : 0.501 : 0.230	$5.1 \cdot 10^5$
Ta	73	0.635	0.344	0.106	0.450	$1.03 \cdot 10^{-2}$	0.248 : 0.501 : 0.251	$1.3 \cdot 10^6$
Re	75	0.655	0.348	0.106	0.441	$8.49 \cdot 10^{-3}$	0.244 : 0.501 : 0.255	$1.9 \cdot 10^6$

Appendix D

The proton beam line ZT7

The ZT7 area uses the PS slow extraction channel SE61. Twenty bunches of 5 ns FWHM duration and 100 ns repetition are accelerated in PS. Period of the beam revolution in the accelerator is equal to 2 μs. So every 2 μs the slow extraction system acts upon the same part of the internal proton beam. In addition the intensity is modulated to the main 50 Hz as well as to higher harmonics.

Reasonable requirements to the beam intensity oscillations are:

Period of oscillations	100 ns	2 μ	20, 10,...ms
Relative intensity of oscillations	$\pm$5%	$\pm$10%	$\pm$15%

The energy of the extracted proton beam equals 24 GeV and its intensity is $2 \cdot 10^{11}$ protons per cycle. The spill length is actually equal to 350 ms and it can be increased up to 450 ms as the flat top is limited to 500 ms. This mode of operation can be realized even for a single cycle within supercycle. During the slow extraction the beam momentum increases by 0.3%.

The primary proton beam is split into two beams in the vertical plane by a special septum magnet (splitter) which controls the beam intensity ratio. The undeflected part of the beam is going to the north area of the East Hall. The bent beam (ZT7 beam) is going to the south area.

Relative intensities of the two beams are controlled by adjusting the splitter magnet and the beam parameters at its location. For proposed experiment an intensity of the proton beam needed is about 10^{11} protons per spill.

For safety considerations, two independent elements are needed for the beam switch off. The following switch off procedure is made with:
— no current in the bending magnet BHZ03;
— closure of a beam stopper STP01.
In this case the proton beam will hit the iron wall separating the PS machine from the primary area. This procedure allows to isolate the ZT7 beam control from other users in the East Hall.

D.1 Magnetic elements of the proton channel

The magnetic channel (Figures 6.1 and 6.2) consists of two quadrupole doublets (QFS2, Q126 and QFS1, Q124) separated by a string of dipoles (C208, M213, M219, M203).

A dipole string bends the beam in order to bring it to the target location and make some slight beam position adjustment on the target. The deviation angle of the beam is equal to 148 mrad. The magnets have to be located as more upstream as possible to minimize the bending power required.

The first quadrupole doublet mostly contains the beam in the beam pipe but it is also used in conjunction with the second one in order to fulfill the optical constraint at the target.

The last doublet with help of the first one brings the beam with required properties on the target. Location, spacing and optics of the doublet have been chosen such as to minimize the dispersion of the focus (Figure 6.2). The beam size on the target can be adjusted in both planes by trimming the four available optical elements.

The small horizontally adjusting magnet (HADJ), placed downstream of the dipoles, in conjunction with one of the main magnets will be used to control both the angle and position of the beam. The HADJ is also needed to compensate for the increase ($\sim 0.3\%$) of the proton momentum during the slow extraction.

The standard way to control the beam position on the target is by open-loop compensation of HADJ magnet with a routine residual sweep to the value less than 0.5 mm. It is also possible to use the same magnet and power supply in a closed-loop system using phototubes on both sides of the beam. An RMS of the beam position about 100 μm should be achievable in this case. An additional advantage of the feedback system is its ability to compensate for slow, moderate drifts in the beam position.

The small magnet (VADJ) will be used to adjust the vertical position of the beam.

Most magnets and quadrupoles are recovered from the present ZT7 line.

Behind the magnetic elements of the channel the proton beam passes through the hole in the iron shield.

The magnetic elements of the channel allow to obtain minimum dimensions of the beam on the target: $H = 3$ mm, $V = 2$ mm, where H and V are horizontal and vertical dimensions at the 2σ level, respectively [DURI94]. The beam divergence is equal to ± 1 mrad.

Stability of the beam centre of gravity at the target of about 0.5 mm or better will be needed inside the spill and from spill to spill. The focus position can be shifted 2 m upstream by simply changing the currents in the quadrupoles.

The experiment will be sensitive to the beam distribution far from the core. Level of the beam halo must be low to diminish a count rate of the coordinate detectors located off the axis of the proton beam.

D.2 Vacuum elements of the channel

The proton beam passes in the standard vacuum tube made of aluminium (Figure 6.4). Outer and inner cross dimensions of the main tube are equal to 197 mm and 185 mm, respectively.

For mounting of the targets the CERN target device of "Marguerite" type will be used. It is rather big vacuum box in which there is a quite complicated mechanism for change up to twelve different targets fastened with help of holders on the wheel.

The target device is connected with the vacuum tube through the vacuum valve with 150 mm body–size hole. The vacuum valve is destined to separate initial part of the vacuum channel in the event of a vacuum disturbance in the vicinity of the setup but not

in the case of emergency. The proton channel at the outlet of PS has an air gap and so any emergency vacuum spoiling is not dangerous for the machine.

A demountable connection is envisaged in the main vacuum tube 2 m upstream of the vacuum valve in order to reserve a possibility for travel the target position within 2 m along the proton beam to change the experimental conditions.

Standard bellows of 200 mm in diameter and standard flanges for quick junction (with aluminium seals) are used for mounting of the channel units.

The vacuum volume upstream of the vacuum valve is evacuated down to 10^{-2} Torr with the backing pump of the Balzers type (30 m^3/sec) through the standard branch tube with manual valve. The vacuum is measured with Pirani gauge.

The proton beam downstream of the target passes in the vacuum also (Figure 6.4). After the target there is a section about 2 m long with the diameter of 400 mm. This section is ended by the blank flange with two openings.

The upper opening is closed by a thin foil window and serves as an outlet for secondary particles arisen in the target and detected by the experimental setup. The window of square cross section has dimensions $105 \times 105\,mm^2$.

To the lower opening the vacuum tube of 100 mm in diameter for the proton beam is connected. Distance between the openings is equal to 122 mm.

The section has a big cross dimensions in order to diminish amount of rescattered on its walls particles that can get into the collimator for the secondary particles.

This section and the proton vacuum tube downstream of the section are evacuated with another vacuum pump of the same type as the main vacuum tube and the vacuum is measured with Pirani gauge also.

Then the vacuum tube of 100 mm in diameter goes through a hole in the radiation shield and between the poles of the spectrometer magnet close to the lower pole (Figure 6.5). The proton beam is deflected in horizontal plane by the magnetic field on the maximum angle $\pm 1.3°$ in accordance with the value and polarity of the magnetic field.

So the flexible vacuum tight connection of the tube in the magnet centre is envisaged in order to keep the proton beam in the tube at any value of the magnetic field. For this purpose the tube after the flexible connection will be turned in horizontal plane. The flexible connection is accomplished with help of a backed rubber ring of high quality placed between the stationary and travelling parts of the tube.

The vacuum tube for the proton beam downstream of the magnet is enlarged to a diameter of 197 mm (standard tube) with help of bellows. The tube of approximately 14 m long passes lower the detectors of the setup and is ended with a thin outlet window near the catcher where the proton beam is absorbed. The tube consists of several sections for convenience of manufacture and transportation. The tube will be moved in horizontal plane in accordance with the value and polarity of the spectrometer magnetic field as mentioned above.

Appendix E

MSGC detector

The detector makes use of the technique known as "Microstrip Gas Chambers" [OED88] ($MSGC$), which can cope with 2 main objectives in the detection of single points pertaining to $\pi^+\pi^-$ track pairs: high space resolution and capability to operate in a high rate environment of 2×10^7 s^{-1}.

It is assembled in a module of 4 consecutive planes, each covering a sensitive area of 10×10 cm^2 (see Figures E.1, E.2 and E.3). Position resolution is achieved by a 200 μm cathode-cathode pitch distance between cromium 90 μm wide parallel strips implanted on a semi-conductor glass support, with bulk resistivity in the range 10^9 to 10^{12} Ω·cm. Interleaved with the cathode strips are anode strips 10 μm wide, which provide electric fields of the order of 100 kV/cm in the amplification region. The basic cell structure is illustrated in Figure E.4, where also a back-plane electrode is shown. A support thickness of 200 μm can be achieved [GEIJ92], which accounts for 0.16% of a radiation length. As a medium for primary ionization we use an Ar+DME gas mixture at 60-40%, which provides sufficient ionization over a gas gap of 3 mm and fast drift speed [BOUC94]. The drift field is supplied by an additional (drift) electrode at the opposite side of the gas gap. Minimum radiation length can be achieved if this electrode is made of evaporated Cr on a 0.2 mm glass. Typical operating voltages are: $V_a = 620$ V, $V_c = 0$ V, $V_b = 100$ V, and $V_d = -1000$ V. With the above-mentioned parameters the detector can be operated at gains larger than 10^3. The planes are mounted in gas-tight boxes closed by the drift electrode. The detector plates are glued on the inner frame of the chip board which contains the front-end electronics and at the same time provides the reference for internal alignment.

In view of the high irradiation of the chambers at $2 \cdot 10^7$ particles per second, particular attention must be paid to the construction materials in order to avoid a long-term ageing behaviour of the chambers. A very promising technique is to use glass frames (which is illustrated in Figure E.5), where only small gain losses (10%) have been observed after 12 $mC \cdot cm^{-1}$ [HORI93]. Another possibility would be the use of high grade polymers, such as VECTRA plates.

In order to be able to resolve multi-particle ambiguities, the detector planes are rotated at angles $0°(X)$, $90°(Y)$,$60°(U)$ and $120°(V)$. Single-hit resolution of 50 μm can be obtained for each plane, only from the digital information of detector elements. From further measurement of individual pulse-height information in clustering signals, the resolution can still be improved.

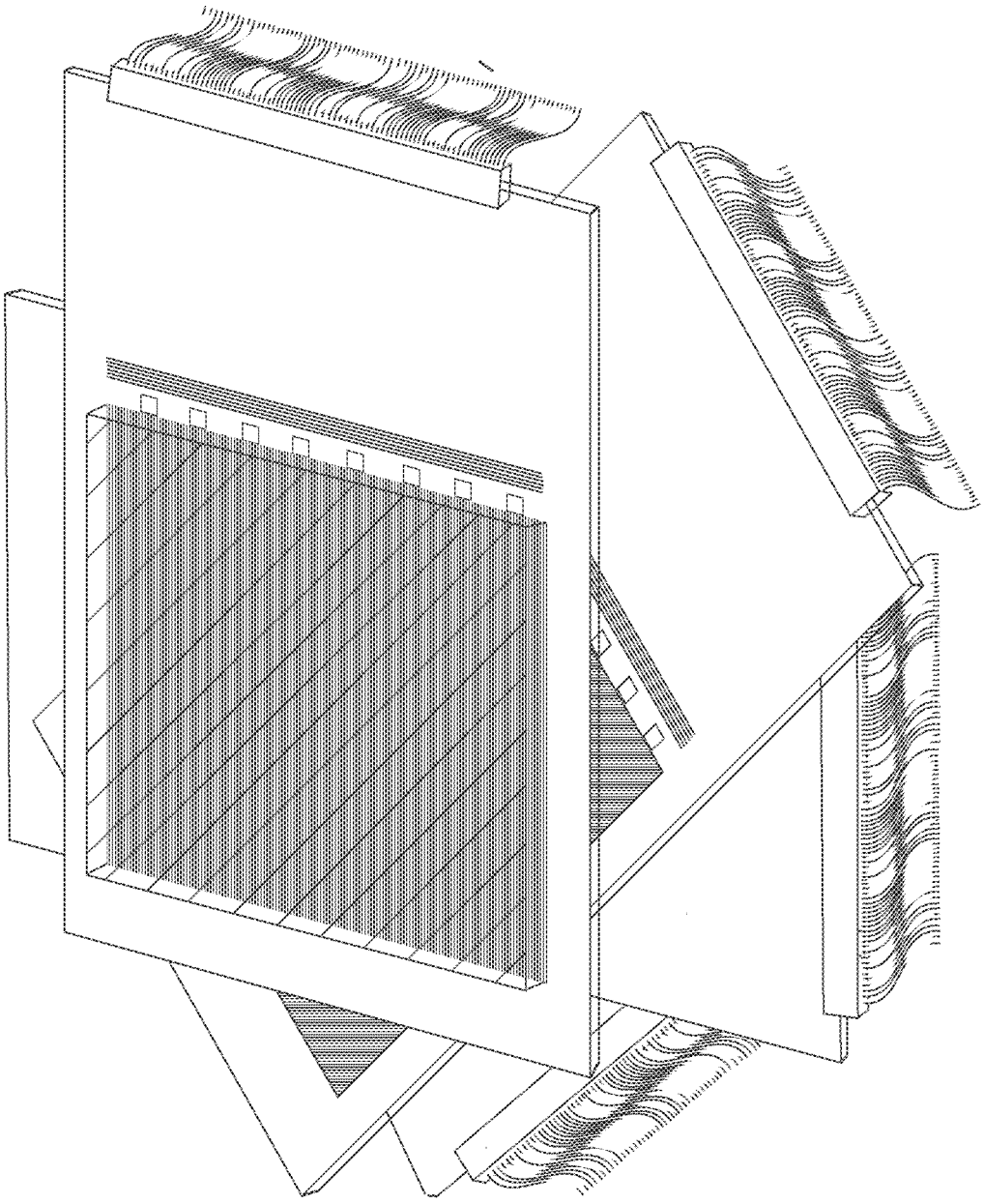

Figure E.1: Layout of $MSGC$ detector

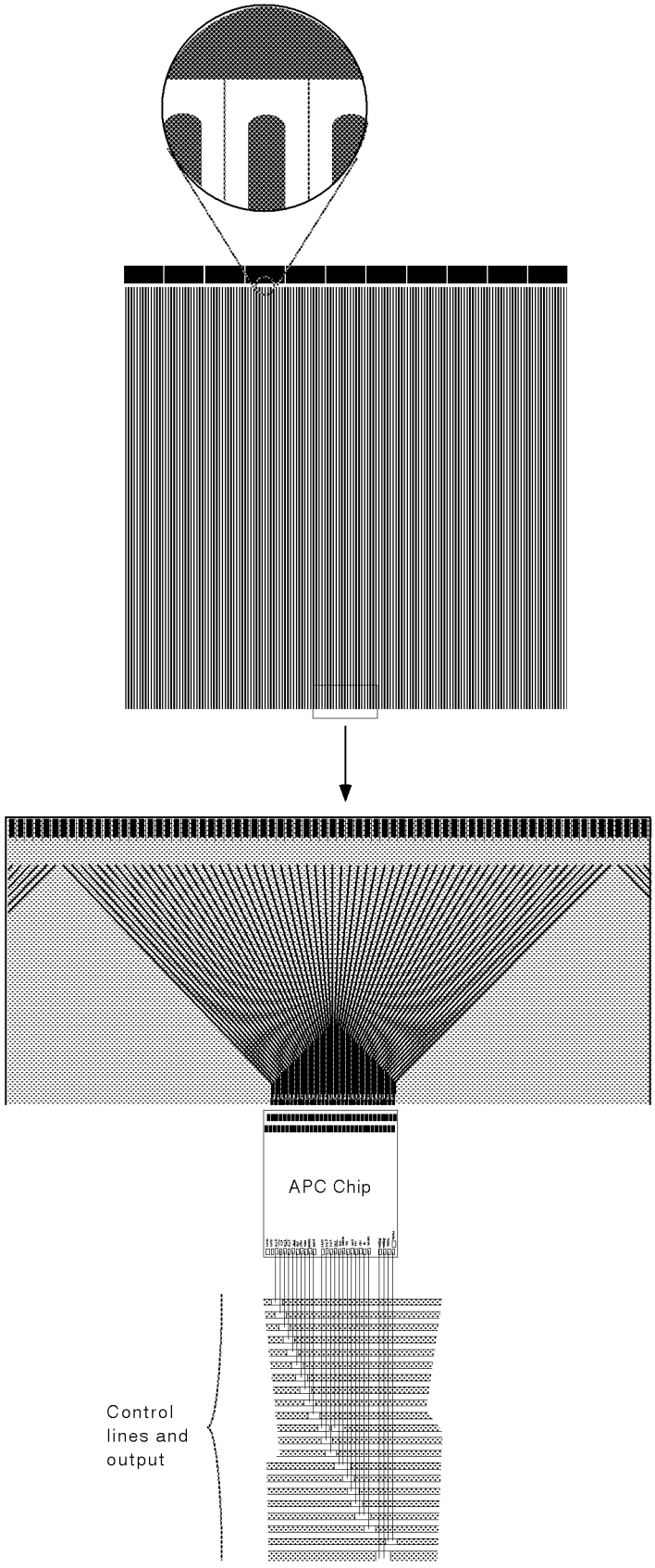

Figure E.2: *MSGC* detector plates

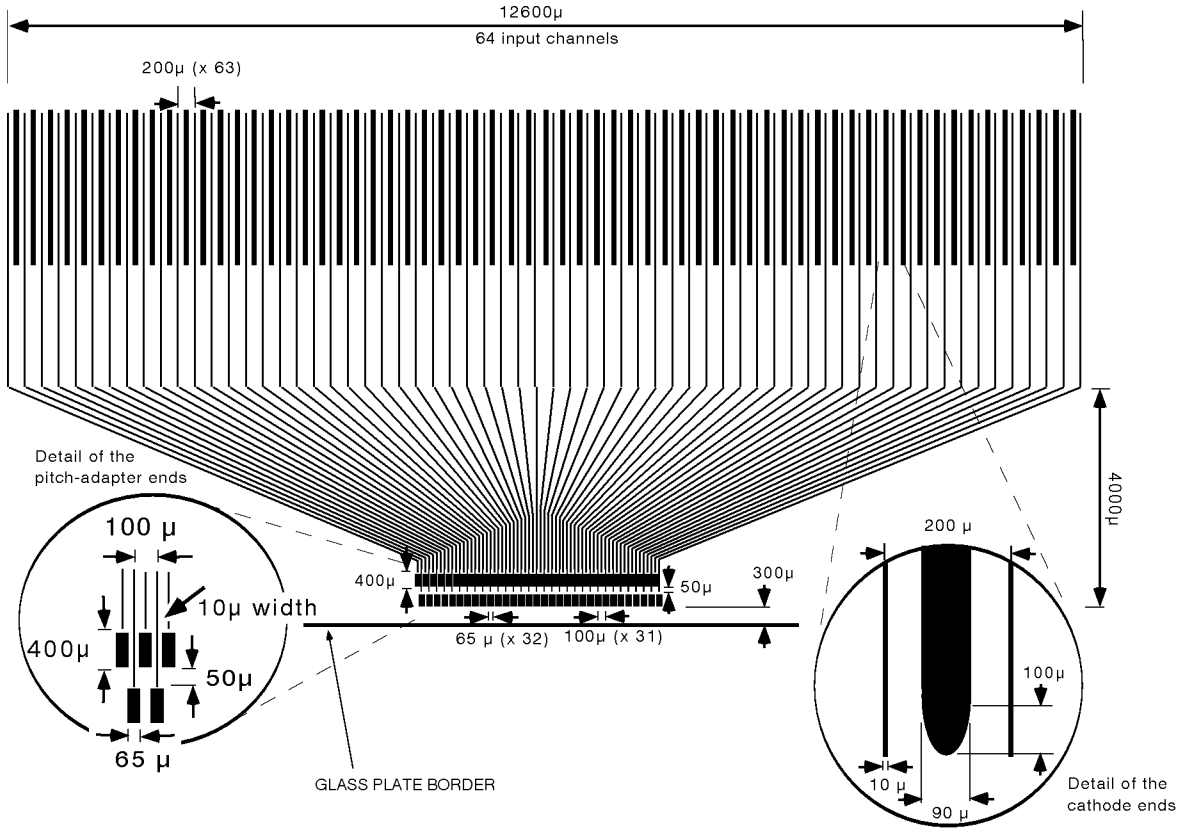

Figure E.3: Details of the pitch-adapter ends.

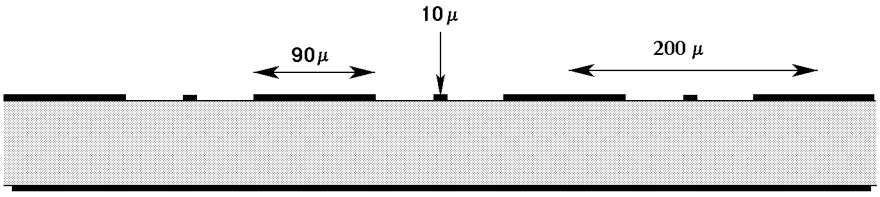

Figure E.4: *MSGC* cell structure

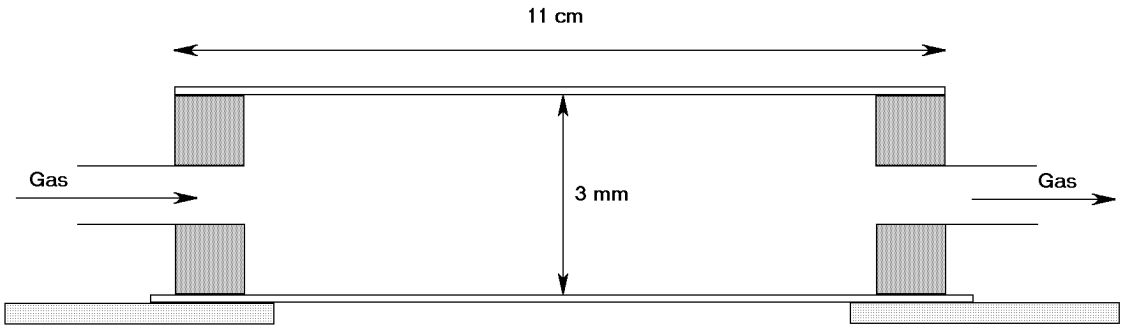

Figure E.5: *MSGC* box assembly

E.1 Electronics readout

The 10×10 cm^2 *MSGC* will be instrumented with VLSI readout. To cope with the different pitch from the microstrip substrate and the chip inputs, the substrate will include at one end of each group of 64 cathodes a built-in pitch adapter (from 200 μm to 93.2 μm). We plan to use a new version of the APC (Analog Pipeline Chip) [ATLA92], which has a pipeline of 32 buffers of depth, and a total of 64 channels per APC. This allows to wait for a trigger and search for the signal in a time interval of less than 3 μs. The preamplifiers (with risetime less than 85 ns) integrate the counter signals and store them in one buffer at a time (with a sampling frequency greater than 10 MHz). Upon trigger arrival it is possible to reread one or several of these buffers, allowing a different effective gain and signal/noise ratio. The effective gain in the chip will be around 10 V/pC. On the other hand it is possible to perform elementary operations with the chip, such as addition or subtraction of buffer charges, so that the signal baseline can be subtracted in the front-end electronics. The 8 chips for each instrumented chamber will then be read serially into a fast digitizer such as SIROCCO module.

E.2 Summary of the detector parameters

- single-hit resolution: $\leq$50μm (at 90°)
- total radiation length : 1.28% X_0
- detector gain: $\geq 10^3$
- ageing resistance (lifetime) : >12 mC cm^{-1}
- electronics gain: $\approx$ 10 V/pC
- time gate for background rejection: 100–200 ns
- power dissipation: 18 mW/chip

Bibliography

[AFAN91A] Afanasyev L.G et al., Phys. Lett. **255B** (1991) 146.

[AFAN91B] Afanasyev L.G. JINR E2-91-578, Dubna, 1991;
JINR B1-2-91-572, Dubna, 1991.

[AFAN93A] Afanasyev L.G. et al., Phys. Lett. **308B** (1993) 200.

[AFAN93B] Afanasyev L.G. et al., Preprint JINR E13-93-234, Dubna, 1993.

[AFAN93C] Afanasyev L.G., Tarasov A.V., JINR E4-93-293, Dubna, 1993.

[AFAN94] Afanasyev L.G. et al., Phys. Lett. **338B** (1994) 478.

[AGOR91] Agoritsas V. et al., DRDC Proposal, DRDC/P-25, 7 March 1991.

[AGOR93] Agoritsas V. et al., RD-17 Status Report, CERN/DRDC/93-47.

[AGOR94] Agoritsas V. et al., Preprint CERN–PPE 94–126 Geneva 1994,
to be published in NIM.

[AKER71] Akerlof G.W. et al., Phys. Rev. **D3** (1971) 645.

[AKIM60] Akimov Yu.K., Komarov V.I. et al., NIM **7** (1960) 37.

[ALEX82] Alekseev G.D. et al., Particles & Nuclei, v.13, No.3, p.703, Moscow 1982.

[ALLA70] Allaby J.V. et al., CERN Rep. No CERN 70–12, 1970.

[ANIS65] Anisovitch V.V., Anselm A.A., Gribov V.N.,
Zh.Eksp.Teor.Fiz. **42** (1962) 224.

[ATHE85] Atherton H.W et al., Phys. Lett., **158B** (1985) 81.

[ATLA92] ATLAS Letter of Intent, CERN/LHCC 92-4
CMS Collaboration CERN/LHCC 93-48

[BADH77] Badhwar G.D., Phys. Rev. **D15** (1977) 820.

[BATU65] Batusov Yu.A. et al., Yad.Fiz. **1** (1965) 687.

[BAYE69] Bayer V.N. and Fadin V.S., Zh.Eksp.Teor.Fiz. **57** (1969) 225.

[BELK79] Bel'kov A.A., Bunyatov S.A., Yad.Fiz. **29** (1979) 1295.

[BELK86] Bel'kov A.A., Pervushin V.N., Tkebuchuva F.G., Yad.Fiz. **44** (1986) 466.

[BERN91] Bernard V., Kaiser N. and Meissner U., Phys.Rev. **D43** (1991) 2757, Nucl.Phys. **B357** (1991) 129.

[BIJN94A] Bijnens J., Colangelo C., Ecker G. and Gasser J., preprint BUTP-94/4, ROM2F 94/05, to appear in Nucl. Phys. B.

[BIJN94B] Bijnens J. et al., work in progress.

[BILE69] Bilenky S.M. et al., Yad.Fiz. **10** (1969) 812.

[BLAI70] Blair I.M. et al., Phys.Lett. **32B** (1970) 528.

[BORE87] Boreiko V.F. et al., JINR P10-87-827, Dubna, 1987.

[BOUC94] Bouclier R. et al. CERN-PPE/94-63

[BOWL91] Bowler M.G., Phys.Lett. **B270** (1991) 69.

[BRUN87] Brun R. et al. *GEANT3 Reference Manual.* CERN Program Library Long Writeup W5013, DD/EE/84–1, 1987.

[CHPT] For recent reviews on CHPT see e.g.
Leutwyler H., [LEUT93];
Meißner U.G., Rep. Prog. Phys. 56 (1993) 903;
Pich A., Lectures given at the V Mexican School of Particles and Fields, Guanajuato, México, December 1992,
preprint CERN-Th.6978/93 (hep-ph/9308351);
Ecker G., Chiral perturbation theory, in: Quantitative Particle Physics: Cargèse 1992, Eds. M. Lévy et al., Plenum Publ. Co. (New York, 1993);
Donoghue J.F., Golowich E. and Holstein B.R., "Dynam ics of the Standard Model" (1992), Cambridge University Press, Cambridge.

[COLA94] Colangelo G., thesis, Università di Roma II, 1994.

[DAFNE] The DAFNE Physics Handbook, eds. L. Maiani, G. Pancheri and N. Paver, INFN-Frascati, 2nd edition, to appear.

[DAVY86] Davydov Yu.I. et al., JINR Communication, Dunba 1986.

[DEKK65] Dekkers D. et al., Phys. Rev. **137** (1965) 962.

[DENI87] Denisenko K.G. and Mrowczynsky S., Phys.Rev. **D36** (1987) 1529.

[DIDD64] Diddens A.N. et al., Nuovo Cim. **31** (1964) 961.

[DITT94] Ditta J. Proceeding of "Journes VLSI (Full-Custom)" at Collège de France, 2 Feb. 1994, and private communications.

[DONO90] Donoghue J., Gasser J. and Leutwyler H., Nucl. Phys. **B343** (1990) 341.

[DURI94] Durieu L., PS/PA/Note 94-13, CERN 1994.

[EFIM86] Efimov G.V., Ivanov M.A., Lyubovitskij V.E., Yad.Fiz. **44** (1986) 460.

[EFIM87] Efimov G.V., Ivanov M.A., Lyubovitskij V.E., Pis'ma v Zh.Eksp.Teor.Fiz., **45** (1987) 526.

[EICH72] Eichten T. et al., Nucl. Phys. **B44** (1972) 333.

[ERAZ94] Erazmus B. et al., Phys. Rev. **C49** (1994) 349.

[FROG77] Froggatt C.D. and Petersen J.L., Nucl. Phys. **B129** (1977) 89.

[GASS83] Gasser J. and Leutwyler H., Phys. Lett. **125B** (1983) 327.

[GASS84] Gasser J. and Leutwyler H., Ann. Phys. **158** (1984) 142.

[GASS85] Gasser J. and Leutwyler H., Nucl. Phys. **B250** (1985) 465, 517, 539.

[GASS94] Gasser J., private communication, work in progress.

[GILL78] Gillespie G.H., Phys.Rev. **A18** (1978) 1967.

[GEIJ92] Geijsberts M. et al. NIM **A313** (1992) 377 and NIM **A315** (1992) 529.

[GRAY74] Grayer G. et al., Nucl. Phys. **B75** (1974) 189.

[GRIS82] Grishin V.G. Inclusive processes in hadron interactions at high energy. Energoizdat, Moscow, 1982, p.131. (in Russian).

[GUET76] Guettler K. et al., Phys. Lett. **64B** (1976) 111.

[HORI93] Horisberger R. and Pitzl D. NIM **A326** (1993) 92.

[HUBB75] Hubbel J.H. et al., J.Phys.Chem.Ref.Data **4** (1975) 71.

[HUBB79] Hubbel J.H., Overbo I., J.Phys.Chem.Ref.Data **8** (1979) 9.

[KALI94] Kalinina N. and Lednitski R., private communication, work in progress.

[KOPY72] Kopylov G.E. and Podgoretsky M.I., Yad. Fiz., **15** (1972) 392.

[KURO81] Kuroda K. et al. Rev. of Sci. Instr. **52** (1981) 337.

[LATT93] For a recent review, see "Lattice 93", Proceedings of the International Symposium on Lattice Field Theory, Dallas, 1992, edited by T. Draper et al., published in: Nucl. Phys. B (Proc. Suppl.) **34** (1994) April 1994.

[LEDN82] Lednitski R. and Ljuboschitz V.L. Yad.Fiz. **35** (1982) 1316.

[LEDN90] Lednitski R. and Ljuboschitz V.L., Proc. Int. Workshop on Particle Correlations and Interferometry in Nuclear Collisions, CORINE90, Nantes, June 28-30, 1990, p.42.

[LEUT93] For a recent review, see Leutwyler H.,in: Proc. XXVI Int. Conf. on High Energy Physics, Dallas, 1992, edited by J.R. Sanford, AIP Conf. Proc. No.272 (AIP, New York, 1993) p.185.

[LEUT93A] Leutwyler H., Bern University preprint BUTP-93/24 (hep-ph/9311274), Ann. Phys. in printing.

[MOLI47] Moliere G., Z.Naturforsch **2A** (1947) 3.

[MOOR94] Moor U., Rasche G. and Woolcock W.S. to appear in Nucl. Phys.

[MORG68] Morgan D. and Shaw G., Nucl. Phys. **B10** (1968) 261.

[MROW87] Mrowczynski S., Phys.Rev. **D36** (1987) 1520.

[NAGE79] Nagels M.M. et al., Nucl. Phys. **147** (1979) 189.

[NAGLIB] NAG Fortran Library Manual, Mark 15, 1st Edition, NAG, Oxford, 1991

[NEME85] Nemenov L.L., Yad.Fiz. **41** (1985) 980.

[OCHS91] Ochs W., Max–Planck–Institue preprint MPI–Ph/Ph 91–35, June 1991.

[OED88] Oed A., NIM **A263** (1988) 351.

[OLLS67] Ollson M.G., Turner L., Phys.Rev.Lett., **20** (1967) 1127.

[RASC94] Rasche G., private communication, work in progress.

[REVI94] Review of Particle Properties, Phys. Rev. **D50** (1994) 1173.

[ROSS75] Rossi A.M. et al., Nucl. Phys. **84B** (1975) 269.

[ROSS77] Rosselet L. et al., Phys. Rev. **D15** (1977) 574.

[SAKH48] Sakharov A.D., Zh.Eksp.Teor.Fiz. **18** (1948) 631.

[SEVI90] Sevior M.E. et al., TRI–PP–90–90, Dec.1990.

[STER93] Stern J., Sazdjian H. and Fuchs N.H., Phys. Rev. D47 (1993) 3814;
Knecht M. and Stern J., preprint IPNO–TH 94–53,
and in Ref. [DAFNE].

[TARA91] Tarasov A.V., Christova I.U., JINR P2-91-10, Dubna, 1991.

[TUYN72] Tuyn J.W.N. et al., Health Physics Internal Report HP–72–118, CERN, 1972.

[URET61] Uretsky J. and Palfrey J., Phys. Rev. **121** (1961) 1798.

[URIB94] Uribe J. et al., Phys.Rev., **D49** (1994) 4373.

[VIGD92] Vigdor S.E. et. al. Letter of Intent, Indiana University Cyclotron Facility 92-115, 1992.

[VOLK87] Volkov M.K., Teor.Mat.Fiz., **71** (1987) 381.

[WEIN66] Weinberg S., Phys.Rev.Lett. **17** (1966) 616.

[WEIN68] Weinberg S., Phys.Rev. **166** (1968) 1568.

[WEIN77] Weinberg S., The Problem of Mass, in: A Festschrift for I.I. Rabi, Transactions of The New York Academy of Sciences, Serie II Volume 38 (The New York Academy of Sciences, New York, 1977).

[WEIN79] Weinberg S., Physica **96A** (1979) 327.